COAL COMBUSTION SIMULATION USING ONE-DIMENSIONAL TURBULENCE MODEL

by

Babak Goshayeshi

A dissertation submitted to the faculty of
The University of Utah
in partial fulfillment of the requirements for the degree of

Doctor of Philosophy

Department of Chemical Engineering

The University of Utah

December 2014

The University of Utah Graduate School

STATEMENT OF DISSERTATION APPROVAL

The dissertation of **Babak Goshayeshi**

has been approved by the following supervisory committee members:

James Sutherland	, Chair	**02/28/2014** Date Approved
Philip Smith	, Member	**02/28/2014** Date Approved
Jost Wendt	, Member	**02/28/2014** Date Approved
Jeremy Thornock	, Member	**02/28/2014** Date Approved
Rob Stoll	, Member	**02/28/2014** Date Approved

and by **Milind Deo**, Chair/Dean of

the Department/College/School of **Chemical Engineering**

and by David B. Kieda, Dean of The Graduate School.

ABSTRACT

The coal combustion process simulated employing high-fidelity models in both gas and particle phase using an Euleraian formulation of One-Dimensional Model (ODT). The coal submodels including vaporization, devolatilization and char oxidation and gasification are described and implemented within the ODT framework. Two coal devolatilization models: a two-rate model based on the Kobayashi-Sarofim and the Chemical Percolation Devolatilization (CPD) are described and implemented. In the gas phase, new formulation of an infinitely fast chemistry (flame-sheet) is developed and implemented.

The main aim of this dissertation is to apply ODT model to simulate a large/pilot scale coal combustor. To achieve this aim, the models are first challenged in much simpler cases. An experiment conducted on single particle combustion in laminar flow is simulated to challenge the gas phase and coal submodels. The effects of the thermochemical models from the turbulence models are isolated. Ignition delay reported by experiment is applied as a metric to measure the accuracy of simulation predictions. The predicted ignition delays indicate that simpler Kobayashi-Sarofim and flame-sheet models roughly capture general trends present in the experimental data, but fail to provide quantitative agreement. On the other hand, the CPD model paired with detailed gas-phase chemistry provides reasonable agreement with the experimental observations over all reported conditions.

Oxy-coal combustion is among the promising technologies to reduce greenhouse gas emissions for stationary power generation. An oxy-coal combustor located at the University of Utah is simulated using the ODT model. Predictions of flame stand-off distance are compared with experimental results. The impacts of models complexity and parameters as well as system parameters on the flame stand-off prediction and flame stability are studied. The influence of gas models, detailed kinetic vs flame-sheet, and devolatilization models, CPD vs Kobayashi-Sarofim models on the prediction of flame stand-off distance are investigated. Furthermore, the impacts of mixing rate and radiative temperature on the flame stability and flame stand-off are studied. Increase in the mixing rate shrinks the flame stand-off Probability Distribution Function (PDF) and moves the mode of PDF to shorter distances, however, the minimum flame stand-off distance is relatively insensitive

to mixing rate. Impact of radiative temperature on flame stand-off distance is significant where an increase in radiative temperature shifts the whole flame stand-off PDF to shorter distances and also decreases the width of PDF. Using flame-sheet calculation in the gas phase, decreases the flame stand-off PDF width and moves the mode of PDF to shorter distances. Nevertheless, the minimum flame stand-off distance is insensitive to use flame-sheet model. It is shown that the devolatilization model dictates the minimum flame stand-off distance.

For years my envoy wandered about the world in quest of the "tree of life" which of none that eats the fruit shall die. But, it is the tree of knowledge within the sage that has its branches and leafs spread all around the world.

– Rumi

To my parents,
who taught me the value of knowledge

CONTENTS

LIST OF FIGURES

LIST OF TABLES

ACKNOWLEDGMENTS

First and foremost, I acknowledge my parents for their unconditional love and support throughout my life. Additionally, thank you to my siblings for encouraging me with their best wishes: you are an integral part of my every success.

I would also like to express my most sincere gratitude to my advisor and mentor, Dr. James C. Sutherland, for his motivational guidance, support and patience throughout my dissertation. Under his supervision, I have learned how to handle the torch of science and wisdom, and to find my path. No matter how many times I interrupted him with questions during his lunch break, he always answered patiently and with a smile. Thank you, Dr. Sutherland, for providing me with this truly enlightening and life-changing experience.

I am very grateful to Dr. Philip Smith and Dr. Jeremy Thornock for their excellent guidance and their willingness to share their knowledge. Thanks also to my excellent committee members, Dr. Rob Stoll and Dr. Jost Wendt.

Thanks to Naveen Punati. Because of his exceptional and reliable work on ODT, I could complete this dissertation. Thanks to Dadmehr Rezaie for providing the experimental results and helping me to set up the simulation. Particular thanks to Amir Biglari, a great friend and also, Michal Hradisky and Tony Saad for the inspirational discussions.

In addition, I would like to thank my friend and flatmate, Roozbeh Gholizadeh, with whom I could share my thoughts, and his unique solutions for problems always delighted me. Thanks to dear Janey and Don Kuffman, whose neighborly company I enjoyed, and who also kindly helped me to review this dissertation.

Catrina Wilson, Jeri Schryver, Christina Bushman, Tracey Farnsworth and Jenny Jones thank you for easing the burdens of office machinery and the tasks of organization.

Once again, I would like to thank my supervisory committee for their time and mentorship.

CHAPTER 1

INTRODUCTION

Coal as an energy carrier plays an important role in the energy market and promises to keep its essential contribution to that market in the future [1]. The modeling of coal behavior in the coal combustion process is a further challenge when accounting for the fact that coal properties and structure change significantly in this process. Throughout this work, coal particle thermochemistry is divided into three subprocesses: vaporization, devolatilization and char oxidation/gasification.

The modeling challenge for coal combustion is further complicated by the varying properties and chemical structure of different coal types [17], and by the fact that the coal properties change significantly throughout a coal particle's lifetime in a combustor [57, 101, 84].

Models for devolatilization vary widely in complexity, with the most sophisticated models accounting for the chemical structure of the coal and its effect on the devolatilization process [89]. In 1971, a constant value was proposed for the combustion rate of each coal type [5]. Arrhenius-form models such as the single-rate [4] and Kobayashi [45] models describe devolatilization with a kinetic rate. In 1976, the Distributed Activation Energy (DAE) model [3] proposed using a gaussian distribution for the activation energy. Determining the parameters for the gaussian distribution were the challenges of this model [70]. Representing coal as a collection of functional group including aromatic rings, aliphatic chains and bridges and oxygen-carrying groups was a significant step in devolatilization modeling [21, 91]. The Chemical Percolation Devolatilization (CPD) model accounts for the thermal decomposition of the macromolecular network and accounts for structural variation among various coal types [25, 6, 89], and can accurately describe light-gas evolution from coal devolatilization [37]. In this work, the Kobayashi and CPD devolatilization models (representing a relatively simple and fairly sophisticated model, respectively) are utilized and their ability to predict ignition delay is examined.

Char oxidation and gasification are heterogenous reactions, and are significantly slower

than the vaporization and devolatilization processes [89, 88]. There are many factors that influence the char oxidation, such as coal structure, coal type, the gas-phase environment (*e.g.*, oxygen partial pressure) and temperature [61, 52]. The products of char oxidation are mainly carbon dioxide and monoxide [56, 95]. A common assumption in coal combustion modeling is that char oxidation occurs after the coal particle is fully devolatilized [98, 97]. The present study and formulation allow for simultaneous vaporization, devolatilization and char oxidation and do not impose any temporal ordering/sequencing of these processes.

The influence of systems parameters such as oxidizer composition and coal rank on ignition delay and flame stability have been explored experimentally by several researchers [48, 54, 51, 36, 43, 44, 72]. A review on experiments measuring the coal particle ignition delay is reported in [11]. In [51], the influence of gas phase temperature and particle size on the single particle ignition delay are also considered as parameters. In Chapter 3, the ignition delay is employed as a metric to evaluate simulation results where the effect of gas phase temperature, coal rank and particle size on ignition delay are studied and compared to the experiments conducted by [51].

Among the promising technologies to reduce the greenhouse gasses and CO_2 sequestration in new and existing coal-fired power plants is oxy-coal combustion. In the process of oxy-coal combustion, pure oxygen is mixed with recycled flue gas rather than with air that combusts with the coal (fuel) providing a low cost option to capture CO_2. The model required to predict the physics of such a system must address particle dynamics in turbulent flow, gas-phase thermochemistry, heterogeneous reactions between the coal and gas, devolatilization/pyrolysis, vaporization, radiative heat transfer, *etc.* The turbulent nature of the practical oxy-coal combustor enforces nonlinear coupling across a multitude of length and time scales, further complicating the modeling.

Numerous studies on oxy-coal combustion and gasification physics, in particular the ignition delay, flame stability and temperature, flame shape, impacts of oxygen and diluent have been undertaken[68, 29, 51, 14]. Various experiments were conducted to measure flame stand-off and stability where impacts of coal type and operating conditions such as composition of coal transport medium were studied [105, 76]. To understand the ignition mechanism in oxy-coal flames, simulation of phenomena employing Computational Fluid Dynamics (CFD) can be quite useful. Researchers use this tool to address the influence of different parameters such radiative temperature and oxygen concentration, on flame stability and ignition point in oxy-coal flames [34].

Applying Direct Numerical Simulation (DNS) with detailed kinetic calculation in the gas

phase and employing advance coal devolatilization models can help improve understanding of ignition and can provide a basis for evaluating simpler models. However, such simulations are prohibitively expensive to compute. In this work, an Eulerian formulation of the One-Dimensional Turbulence (ODT) model is used. ODT resolves the full range of length and time scales of the continuum (as in DNS) but in a single spatial dimension. First proposed by [41], ODT has been successfully applied to a variety of turbulent flows, including particle-laden flows [80] and turbulence-chemistry interaction [73] including extinction and reignition [49]. Several assumptions in ODT are made *a priori*, with a particularly noteworthy assumption that the flow field is statistically one-dimensional (implications of this assumption are discussed in [74, 93]). The one-dimensional nature of ODT provides a suitable platform to undertake numerical simulation with much lower computational cost than DNS. In this work, ODT is used to simulate oxy-coal flames and is evaluated against experimental data [105, 77].

The dissertation is arranged as follows: Chapter 2 provides the applied governing equations and a general description of models components. In this chapter, conservation equations as well as source terms for gas and particle phase will be discussed. In addition, a method to exchange source terms between gas and particle phases is suggested. Furthermore, coal submodels including vaporization, devolatilization and char oxidation and gasification are elaborated upon. The combustion of single coal particle in laminar flow is studied in Chapter 3 where ignition delay is applied as a metric to measure the accuracy of simulation predictions. In Chapter 4 the simulation predictions of the oxy-coal combustor located at the University of Utah will be analyzed. The flame stand-off distances predicted by simulation will be compared with the experiment. The conclusion of this dissertation is provided in Chapter 5.

CHAPTER 2

MODELS FORMULATION

"... It is typical of these cases that an indeterminacy originally restricted to the atomic domain becomes transformed into macroscopic indeterminacy, which can then be resolved by direct observation. That prevents us from so naively accepting as valid a blurred model for representing reality. In itself, it would not embody anything unclear or contradictory. There is a difference between a shaky or out-of-focus photograph and a snapshot of clouds and fog banks."

-Erwin Schrowdinger

The ODT formulation utilized in this dissertation can be divided into two main sections:

1. Gas or carrier phase: a Eulerian formulation of ODT applied to determine the physics of the gas phase.

2. Particle or disperse phase: a Lagrangian frame of reference used for individual particles's trajectories.

The ODT equations formulated through expressions using ExprLib software allows the programmer to apply graph theory on the complex algorithm and by simply specifying the dependency among expression reduces the level of complexity [66][1].

Mathematical expressions are implemented as objects that directly expose data dependencies. Using this approach makes problems with complex dependencies tractable, and removes virtually all logic from the algorithm itself. Additionally, it allows the developers to commit highly localized changes, without a detailed understanding of any algorithms [66].

Detailed description of the phase's formulation are provided in this chapter. Furthermore, the expression graphs produced by test cases of each model are presented. These

[1]https://software.crsim.utah.edu/trac/wiki/ExprLib

expression graphs, presented for submodels, provide other developers with the required information on the tags and dependencies of the utilized models.

2.1 Gas Phase

A Eulerian formulation of ODT [93] adapted to solve multiphase reacting flows is applied in this dissertation. The conservation equations are

$$\frac{\partial \rho}{\partial t} = -\frac{\partial v}{\partial y} + S_{\mathrm{p}m}, \tag{2.1}$$

$$\frac{\partial \rho v}{\partial t} = -\frac{\partial \rho v v}{\partial y} - \frac{\partial \tau_{yy}}{\partial y} - \frac{\partial P}{\partial y} + S_{\mathrm{p}v}, \tag{2.2}$$

$$\frac{\partial \rho u}{\partial t} = -\frac{\partial \rho v u}{\partial y} - \frac{\partial \tau_{yx}}{\partial y} + S_{\mathrm{p}u}, \tag{2.3}$$

$$\frac{\partial \rho e_0}{\partial t} = -\frac{\partial \rho e_0 v}{\partial y} - \frac{\partial p v}{\partial y} - \frac{\partial \tau_{yy} v}{\partial y} - \frac{\partial q}{\partial y} + S_{\mathrm{p}e_0}, \tag{2.4}$$

$$\frac{\partial \rho Y_i}{\partial t} = -\frac{\partial \rho Y_i v}{\partial y} - \frac{\partial J_i}{\partial y} + \omega_i + S_{\mathrm{p}Y_i}, \tag{2.5}$$

where u and v refer to streamwise and spanwise velocities, respectively, mixture-averaged approximations are used for diffusive fluxes, and P is obtained via the ideal gas equation of state. $S_{\mathrm{p}m}$, $S_{\mathrm{p}v}$, $S_{\mathrm{p}u}$, $S_{\mathrm{p}e_0}$ and $S_{\mathrm{p}Y_i}$ are interphase exchange terms for mass, y-momentum, x-momentum, total internal energy and species, respectively, (see §2.3), and the p subscript denotes a particle-phase property. Here, the y-direction is taken as the spanwise direction

2.1.1 Detailed Kinetics Calculation

Cantera software is utilized to calculate gas phase properties as well as reaction rates. In the single particle case (chapter 3), the full GRI3.0 mechanism consisting of 53 species and 325 reaction is utilized. However, for simulation performed in oxy-coal combustion, Chapter 4, a reduced GRI mechanism, consisting of 24 species and 86 reactions is utilized [86].

Transport equations are solved for the species, with appropriate phase-exchange source terms for the devolatilization, vaporization, and char oxidation models.

2.1.2 Flame-sheet Model

The flame-sheet model assumes an infinitely fast reaction

$$r_i \rightarrow \pi_i, \tag{2.6}$$

where r_i and π_i are the moles of i^{th} species (except O_2) in reactants and flame-sheet product, respectively. It is assumed that the products of reaction are CO_2, H_2O and N_2. The oxygen required to consume each species is defined as

$$\xi_i = (\sigma_{iC} + \sigma_{iH}/4 - \sigma_{iO}/2) \quad i \equiv \text{species, except } O_2 \tag{2.7}$$

where ξ_i represents stoichiometric oxygen to burn the one mole of species i and σ_{ij} is the number of element j in the species i. The stoichiometric oxygen requirement can be calculated as

$$\theta = \sum_i r_i \xi_i \quad i \equiv \text{species, except } O_2. \tag{2.8}$$

The equivalence ratio, $\Phi = \frac{r_{O_2}}{\theta}$, is used to determine the products of reaction. In rich conditions ($\Phi \geq 1$),

$$\pi_i = \begin{cases} E^r_C & i = CO_2 \\ E^r_H/2 & i = H_2O \\ E^r_N/2 & i = N_2 \\ r_{O_2} - \theta & i = O_2 \\ 0 & \text{otherwise} \end{cases} \tag{2.9}$$

where E^r_j is the amount of element j provided by the reactants,

$$E^r_j = \sum r_i \sigma_{ij} \quad i \neq O_2. \tag{2.10}$$

Likewise, for rich conditions ($\Phi < 1$),

$$\pi_i = \begin{cases} r_{CO_2} + E^\pi_C & i = CO_2 \\ r_{H_2O} + E^\pi_H/2 & i = H_2O \\ r_{N_2} + E^\pi_N/2 & i = N_2 \\ 0 & i = O_2 \\ r_i(1 - \Phi \frac{\xi_j}{\sum_j \xi_j}) & \text{otherwise} \end{cases} \tag{2.11}$$

where

$$E^\pi_j = \Phi \sum_i r_i \sigma_{ij}. \tag{2.12}$$

represents the number of moles of element j produced by reaction (2.6). In the flame-sheet model, transport equations are solved for each species that is involved in the coal models

(devolatilization, vaporization and char oxidation) as well as any gaseous species fed into the reactor. The product composition is then obtained at each point in space and time using the methodology just discussed in this section.

2.2 Coal Phase

The motion of a single particle in gas-solid flows can be described by using Newton's second law

$$m_{\mathrm{p}}\frac{\mathrm{d}u_{\mathrm{i,p}}}{\mathrm{d}t} = m_{\mathrm{p}}g_{\mathrm{i}} + S_{\mathrm{p}_j,v} + F_{\mathrm{c}} \tag{2.13}$$

where i denotes the i^{th} direction, m_{p}, $u_{i,\mathrm{p}}$, g_{i}, $S_{\mathrm{p}_j,v}$, and F_c are mass of single particle, particle velocity, gravity acceleration in i^{th} direction, force generated by fluid-particle interaction, and force generated by particle-particle interaction. For this study, particle-particle interaction is ($F_{\mathrm{c}} = 0$) and the drag force is described by Stokes' law so that the particle momentum equations become

$$\frac{\mathrm{d}u_{\mathrm{p_j}}}{\mathrm{d}t} = \frac{g_i\left(\rho_{\mathrm{p}} - \rho_{\mathrm{g}}\right)}{\rho_{\mathrm{p}}} + S_{\mathrm{p}_j,u}, \tag{2.14}$$

$$\frac{\mathrm{d}v_{\mathrm{p_j}}}{\mathrm{d}t} = \frac{g_i\left(\rho_{\mathrm{p}} - \rho_{\mathrm{g}}\right)}{\rho_{\mathrm{p}}} + S_{\mathrm{p}_j,v}. \tag{2.15}$$

Particle source terms for v ($S_{\mathrm{p_j},v}$) and u ($S_{\mathrm{p_j},u}$) are given by (2.76) and (2.77), respectively.

Given the evolution of the particle velocity according to (2.14) and (2.15), the particle position evolves as

$$\frac{\mathrm{d}x_{i,\mathrm{p}}}{\mathrm{d}t} = u_{i,\mathrm{p}}, \tag{2.16}$$

where $x_{i,\mathrm{p}}$ is particle location in i^{th} direction.

The particle energy evolution is given by

$$\frac{\mathrm{d}T_{\mathrm{p}}}{\mathrm{d}t} = \frac{-A_{\mathrm{p}}}{m_{\mathrm{p}}C_{\mathrm{p}}}\left[h_c\left(T_{\mathrm{p}} - T\right) + \varepsilon\sigma\left(T_{\mathrm{p}}^4 - \mathrm{T}_{\mathrm{w}}^4\right)\right] + S_r, \tag{2.17}$$

where T_{p}, $\mathrm{T_w}$ and T are the particle, radiative (wall), and gas temperatures, respectively. C_{p}, m_{p}, A_{p} and ϵ are the particle heat capacity, mass, surface area (sphere surface) and emissivity, respectively, σ is the Stefan-Boltzmann constant, $h_c = {}^{Nu\kappa}/_{\mathrm{d_p}}$ is the convective heat transfer coefficient with $Nu = 2.0 + 0.6Re_{\mathrm{p}}^{1/2}Pr^{1/3}$ [32] where $\mathrm{d_p}$ is the particle diameter, and S_r is the temperature source term due to vaporization and heterogeneous reactions defined by (2.81). In this work, radiation is considered only between particles and an "effective" furnace environment.

The overall mass balance on coal particle (m_{p}) is divided into three phenomenological categories describing the evolution of moisture ($m_{\mathrm{H_2O}}$), volatiles (m_{v}), and char (m_{c}),

$$\frac{\mathrm{d}m_{\mathrm{p}}}{\mathrm{d}t} = \frac{\mathrm{d}m_{\mathrm{w}}}{\mathrm{d}t} + \frac{\mathrm{d}m_{\mathrm{v}}}{\mathrm{d}t} + \frac{\mathrm{d}m_{\mathrm{c}}}{\mathrm{d}t}. \tag{2.18}$$

In the proposed model, a coal particle consists of moisture, volatile, char and ash. Figure 2.1 depicts the coal's constituents and the models that describe mass exchange. For example, evaporation only adds moisture into the gas phase; however, char oxidation produces CO_2 and CO and consumes O_2. The models that describe the consumption of coal constituents are outlined in §2.2.1-§2.2.3

2.2.1 Evaporation

The moisture content evolution is given by

$$\frac{\mathrm{d}m_{\mathrm{w}}}{\mathrm{d}t} = -\left(S_{\mathrm{p,H_2O}}\right)^{\mathrm{Evap}} = k_v \left(\frac{P^{\mathrm{sat}}_{\mathrm{H_2O}}}{\mathrm{R}T} - \frac{P_{\mathrm{H_2O}}}{\mathrm{R}T_{\mathrm{g}}}\right) A_{\mathrm{p}} M_{\mathrm{w,H_2O}}, \tag{2.19}$$

where k_v is the mass transfer coefficient of steam (m^2/s) into air [63], $P^{\mathrm{sat}}_{\mathrm{H_2O}}$ is the saturation pressure of water at particle temperature, $P_{\mathrm{H_2O}}$ is partial pressure of water in gas. Determination of k_v is given by:

$$Sh = \frac{k_v d_{\mathrm{p}}}{D_{\mathrm{H_2O},gas}} = 2.0 + 0.6 Re_{\mathrm{p}}^{1/2} Sc_{\mathrm{g}}^{1/3},$$

where Sh is the Sherwood number, Re_{p} is the Reynolds number of particle, Sc_{g} is the Schmidt number of gas phase, $D_{\mathrm{H_2O,gas}}$ is the diffusivity of water into gas phase and d_{p} is the diameter of particle.

The saturation pressure of water is considered as a function of particle temperature and calculated using the Buck equation [7]:

$$P^{\mathrm{sat}}_{\mathrm{H_2O}} = 611.21 exp\left[\left(18.678 - \frac{T_{\mathrm{p}}}{234.5}\right)\left(\frac{T_{\mathrm{p}}}{257.14 + T_{\mathrm{p}}}\right)\right]. \tag{2.20}$$

For purposes of energy coupling in (2.81) the latent heat of vaporization for water is calculated from the Watson relation [71, 103], which provides the latent heat of vaporization as a function of temperature. The Watson relation is:

$$\frac{\lambda_{\mathrm{Evap}}}{\lambda_{\mathrm{ref}}} = \left(\frac{1 - T_r}{1 - \mathrm{T_{ref}}}\right) \tag{2.21}$$

where T_r and $\mathrm{T_{ref}}$ are the reduced temperature (base on water critical temperature) of particle and reference temperature. λ_{Evap} and λ_{ref} are the water latent heat of vaporization at particle and a reference temperature, respectively. Since the pressure is essentially constant

over the domain for the conditions considered here, this model provides an inexpressive calculation for the required latent heat of vaporization. Figure 2.2 shows a comparison between the Watson model and a model proposed by [69].

The expression graph of the evaporation model is illustrated in Figure 2.3. The evaporation rate expressed in (2.19) is the expression in the middle with the tag name of evaporation_rhs. This expression employed all the other expressions connected with arrow to calculate the arguments used in its equation.

2.2.2 Devolatilization

Three devolatilization models with different complexities and computational costs are implemented.

2.2.2.1 Kobayashi-Sarofim Model

In this model, the devolatilization process is described as following:

$$m_v \rightarrow \alpha_1 g_i + (1 - \alpha_1 c), \tag{2.22}$$

$$m_v \rightarrow \alpha_2 g_i + (1 - \alpha_2 c). \tag{2.23}$$

α_1 and α_2 are weights of release light gases in each rate [45], c is the produced char in the devolatilization process.

The devolatilization rate described in this model has two weighted first order Arrhenius reaction rates [45],

$$\frac{\mathrm{d}m_v}{\mathrm{d}t} = -(r_1 + r_2) = -\left[A_1 e^{(-E_1/\mathrm{R}T_\mathrm{p})} + A_2 e^{(-E_2/\mathrm{R}T_\mathrm{p})}\right] m_v, \tag{2.24}$$

where r_1 and r_2 are reaction rates for 2.22 and 2.23, respectively; and the Arrhenius parameters (A_1, E_1, A_2, E_2) reported in [96] were used, consistent with several other studies [83, 12, 15, 68]. The influence of the Arrhenius parameters for the Kobayashi-Sarofim model for coal simulations has been considered by [26]. By substituing 2.22 and 2.23 into 2.24 and after some simplification,

$$\frac{\mathrm{d}m_v}{\mathrm{d}t} = [\beta\alpha_1 + (1-\beta)\alpha_2]\frac{\mathrm{d}g_i}{\mathrm{d}t} + [\beta(1-\alpha_1) + (1-\beta)(1-\alpha_2)]\frac{\mathrm{d}c}{\mathrm{d}t} = \chi\frac{\mathrm{d}g_i}{\mathrm{d}t} + \Upsilon\frac{\mathrm{d}c}{\mathrm{d}t}, \tag{2.25}$$

where

$$\beta = \frac{r_1}{r_1 + r_2}. \tag{2.26}$$

Different reactions have been proposed for the Kobayashi devolatilization model [85]. Although there is no universally accepted form, in this work, we assume

$$\mathrm{CH}_a\mathrm{O}_b \rightarrow \chi\left[x\mathrm{CO} + y\mathrm{H}_2 + z\mathrm{C}_2\mathrm{H}_2\right] + \Upsilon\mathrm{C}_{(\mathrm{s})}. \tag{2.27}$$

where a and b are calculated from coal's ultimate and proximate analysis. There is general agreement on CO and H_2 as the products for Kobayashi model, but accounting for tar in the gas phase is less well-established. In this work, C_2H_2 represents tar in the gas phase. To satisy the elemental balance over the coal particle,

$$x = \frac{a}{\chi},\ y = \frac{b}{2\chi} - z,\ z = \frac{1 - \Upsilon - b}{2\chi}.$$

In this mode, the species yield are

$$\frac{\mathrm{d}m_{\mathrm{CO}}}{\mathrm{d}t} = -x\frac{\mathrm{M_{w,CO}}}{\mathrm{M}_{\mathrm{w},v}}\frac{\mathrm{d}m_{\mathrm{v}}}{\mathrm{d}t} \tag{2.28}$$

$$\frac{\mathrm{d}m_{\mathrm{H_2}}}{\mathrm{d}t} = -y\frac{\mathrm{M_{w,H_2}}}{\mathrm{M}_{\mathrm{w},v}}\frac{\mathrm{d}m_{\mathrm{v}}}{\mathrm{d}t} \tag{2.29}$$

$$\frac{\mathrm{d}m_{\mathrm{C_2H_2}}}{\mathrm{d}t} = -z\frac{\mathrm{M_{w,C_2H_2}}}{\mathrm{M}_{\mathrm{w},v}}\frac{\mathrm{d}m_{\mathrm{v}}}{\mathrm{d}t} \tag{2.30}$$

$$\frac{\mathrm{d}m_{\mathrm{C_{(s)}}}}{\mathrm{d}t} = -\Upsilon\frac{\mathrm{M_{w,C(s)}}}{\mathrm{M}_{\mathrm{w},v}}\frac{\mathrm{d}m_{\mathrm{v}}}{\mathrm{d}t} \tag{2.31}$$

where $\mathrm{M_{w,CO}}$, $\mathrm{M_{w,H_2}}$, $\mathrm{M_{w,C_2H_2}}$, $\mathrm{M}_{\mathrm{w},v}$ are molecular weight of CO, H_2, C_2H_2 and volatile, rescpectively. The reaction rate of 2.22 and 2.23 are different through the time, therefore, the elemental coeffencts, a and b are chaging through the time,

$$\frac{\mathrm{d}a}{\mathrm{d}t} = -\frac{2}{\mathrm{M_{w,H_2}}}\frac{\mathrm{d}m_{\mathrm{H_2}}}{\mathrm{d}t} - \frac{2}{\mathrm{M_{w,C_2H_2}}}\frac{\mathrm{d}m_{\mathrm{C_2H_2}}}{\mathrm{d}t}, \tag{2.32}$$

$$\frac{\mathrm{d}b}{\mathrm{d}t} = -\frac{1}{\mathrm{M_{w,CO}}}\frac{\mathrm{d}m_{\mathrm{CO}}}{\mathrm{d}t}. \tag{2.33}$$

In 2.27 the elemental coeffecient of carbon must be kept as one, therefore it must be its consumption rate affects the elemental coeffiecient of hydrogen (a) and oxygen (b). The consumption rate of carbon is

$$\frac{\mathrm{d}carbon}{\mathrm{d}t} = -\frac{1}{\mathrm{M_{w,CO}}}\frac{\mathrm{d}m_{\mathrm{CO}}}{\mathrm{d}t} - \frac{1}{\mathrm{M_{w,C_2H_2}}}\frac{\mathrm{d}m_{\mathrm{C_2H_2}}}{\mathrm{d}t} - \frac{1}{\mathrm{M_{w,C_{(s)}}}}\frac{\mathrm{d}m_{\mathrm{C_{(s)}}}}{\mathrm{d}t}. \tag{2.34}$$

Considering 2.34, equations 2.32 and 2.33 must be modified accrodingly,

$$\frac{\mathrm{d}a^{'}}{\mathrm{d}t} = \left(\frac{\mathrm{d}a}{\mathrm{d}t} - a\frac{\mathrm{d}carbon}{\mathrm{d}t}\right) / \left(1 - \frac{\mathrm{d}carbon}{\mathrm{d}t}\right), \tag{2.35}$$

$$\frac{\mathrm{d}b^{'}}{\mathrm{d}t} = \left(\frac{\mathrm{d}b}{\mathrm{d}t} - b\frac{\mathrm{d}carbon}{\mathrm{d}t}\right) / \left(1 - \frac{\mathrm{d}carbon}{\mathrm{d}t}\right). \tag{2.36}$$

The expressions graph produced by a test case is illustrated in Figure 2.4. The main expression only has dependency to particle temperature and volatile mass, which is similar for all the deovlatilization models implemented in this work.

2.2.2.2 Single-Step Model

This is one of the first models to describe devolatilization with an Arrhenius reaction form. The devolatilization process is described with reaction as following:

$$CH_aO_b \rightarrow bCO + \frac{a+b-1}{2}H_2 + \frac{1-b}{2}C_2H_2. \tag{2.37}$$

The volatile yield is determined from:

$$\frac{dm_v}{dt} = -Ae^{(-E/RT_p)}m_v, \tag{2.38}$$

where $A = 4.5 \times 10^5$ (1/s) and $E = 8.1 \times 10^7$ (J/K mol) [35]. This model does not produce any char as a side product of devolatilization, whereas the char production is considered in the Kobayashi-Sarofim and CPD model.

This model is implemented in the ODT framework with the keyword of SingleRate. However, its predictions are not included in this dissertation.

2.2.2.3 Chemical Percolation Devolatilization (CPD) Model

CPD is one of the most accurate (and complex) models available to predict the production rates of the species during the devolatilization. CPD predicts the devolatilization of different coal types based on their chemical structure. In CPD, coal is described as a macromolecular network of aromatic ring clusters of various sizes and types that are connected by a variety of chemical bridges (so-called "labile bridges") of different bond strengths [25].

In the modified CPD model [37], used in this work, reactions start with cleaving labile bridge l to form a highly reactive intermediate (l^*)

$$l \xrightarrow{k_b} l^* \tag{2.39}$$

which then decomposes to form a char bridge (c) and light gases (g) as well as side-chains

$$l^* \xrightarrow{k_c} c + 2g_2 \tag{2.40}$$

$$l^* \xrightarrow{k_\delta} 2\delta_i \tag{2.41}$$

The side chains (δ_i) decompose to form light gases,

$$\delta_i \xrightarrow{k_g} g_i. \tag{2.42}$$

We can write the balance equations for the above quantities as

$$\frac{\mathrm{d}l}{\mathrm{d}t} = -k_b l, \tag{2.43}$$

$$\frac{\mathrm{d}l^*}{\mathrm{d}t} = k_b l - (k_\delta + k_c) l^*, \tag{2.44}$$

$$\frac{\mathrm{d}c}{\mathrm{d}t} = k_c l^* \cong \frac{k_b l}{\rho_{\frac{\delta}{c}} + 1}, \tag{2.45}$$

$$\frac{\mathrm{d}\delta_i}{\mathrm{d}t} = \left[\frac{2\rho_{\frac{\delta}{c}} k_b l}{\rho_{\frac{\delta}{c}} + 1}\right] \frac{f g_i}{\sum_{j=1}^{16} f g_j} - k_{gi}\delta_i, \tag{2.46}$$

also for g_i the reaction rate is

$$\frac{\mathrm{d}g_i}{\mathrm{d}t} = (S_{\mathrm{p},y_i})^{\mathrm{CPD}} = \left[\frac{2k_b l}{\rho_{\frac{\delta}{c}} + 1}\right] \frac{f g_i}{\sum_{j=1}^{16} f g_j} + k_{gi}\delta_i \tag{2.47}$$

where $\rho_{\frac{\delta}{c}} = \frac{k_\delta}{k_c}$ and fg_i are functional groups for each species stated in Table 2.1.

k_b is reaction constant which is described as

$$k_b = A_b e^{\frac{-E_0}{RT}} \tag{2.48}$$

where E_b is the activation energy and can be expressed by

$$F(E) = \frac{1}{\sqrt{2\pi\sigma^2}} \int_{-\infty}^{E} e^{-(1/2)(E-E_0)/\sigma^2} dE \tag{2.49}$$

where $F(E)$ is

$$F(E) = \frac{l}{l_0} \tag{2.50}$$

where l_0 is the initial amount of labile bridge. Also for k_{g_i}, the same procedure is applied but the only difference is the expression for $F(E)$,

$$F(E) = \frac{g_i}{g_{i,max}} = \frac{g_i}{2(1-c_0)\frac{f g_i}{\sum f g_i}} \tag{2.51}$$

The evolution of volatile mass during the devolatilization can be expressed by

$$\frac{\mathrm{d}m_v}{\mathrm{d}t} = -\left(\sum_i^{16} \frac{dg_i}{dt} + \frac{dc}{dt}\right). \tag{2.52}$$

The CPD model employed herein involves solution of 18 ODEs on each particle to evolve the quantities related to devolatilization, and has been shown to provide accurate evolution of

several light gases for devolatilization of various coal types over a range of thermal conditions [37]. The gas-phase species produced by the CPD model are: CO_2, CO, CH_4, C_2H_2, HCN, NH_3, H and H_2O.

In this work, C_2H_2 represents the "tar" in the devolatilization process. The focus of this dissertation is on the ignition process and flame regimes, therefore, soot production process is not considered.

In the scope of this work, C_2H_2 as a soot precursor is used to address the "tar" production by the devolatilization process. Char is a side product of the CPD model as stated in (2.40). Equation (2.45) represents the char production by CPD model that its initial condition is a function of coal type. The initial value of char accounted for the CPD model is given by:

$$if\ \mathrm{C} > 0.859 \quad \rightarrow \quad c_0 = 11.83\mathrm{C} - 10.16$$

$$if\ \mathrm{O} > 0.125 \quad \rightarrow \quad c_0 = 1.25\mathrm{O} - 0.175,$$

where C and O are carbon and oxygen content of coal. Acetylene was chosen since it is a soot precursor [20] and also, it is included in the gas phase mechanisms utilized in this dissertation.

2.2.3 Char Oxidation/Gasification

Char oxidation and gasification are heterogeneous reactions at the particle surface. The mass-exchange terms are accounted for in the mass balance equation, (2.5). Char oxidation is a complex phenomenon that depends on many factors such as temperature and oxygen concentration. Most of the coal combustors are currently operating at atmospheric pressure. However, there are numerous processes, such as coal gasification, which operate at elevated pressure [59, 64, 52]. In this dissertation, all the formulations are provided for atmospheric pressure.

The rate of consumption of char by oxidation is described by [61]

$$\left(\frac{\mathrm{d}m_c}{\mathrm{d}t}\right)^{\mathrm{Oxid}} = \frac{r_{\mathrm{c}}\mathrm{M}_{\mathrm{w,C}}}{\varphi}\pi \mathrm{d}_{\mathrm{p}}^2, \tag{2.53}$$

where $\varphi = 2/(1+\psi)$, $\mathrm{M}_{\mathrm{w,C}}$ is the molecular weight of carbon and r_{c} is the the reaction rate of char. The value of ψ represents the moles of CO_2 formed per moles of carbon that react.

$$\psi = \frac{\frac{\mathrm{CO_2}}{\mathrm{CO}}}{1+\frac{\mathrm{CO_2}}{\mathrm{CO}}}, \tag{2.54}$$

CO_2 and CO are the most common products of char oxidation, there are several equations which express the ratio of CO_2/CO production. This ratio has a significant influence on the

particle temperature that affects the whole coal combustion process [22]. There are several models describing the CO_2/CO ratio. [56] proposed an experimental Arrhenius from the equations that follow:

$$\frac{\mathrm{CO}}{\mathrm{CO_2}} = A \exp\left(-\frac{E}{RT_\mathrm{p}}\right),$$

where $A = 10^{3.3}$ and $E = 14300$ cal/mol. Later, [95] contributed oxygen partial pressure into the equation, and is given by:

$$\frac{\mathrm{CO_2}}{\mathrm{CO}} = A P_{O_2,s}^{n} \exp\left(\frac{B}{T_\mathrm{p}}\right), \tag{2.55}$$

where $A = 0.02$, $B = 3070$ K and $n = 0.2$.

Nevertheless, [22] derived different parameters for (2.55) by compiling the detailed heterogeneous reaction mechanism. They found significant disagreement in the CO2/CO ratio predicted by Tognotti parameters [95]. In this dissertation, (2.55) parameters suggested by [95] are utilized.

There are several models and equations that explain char oxidation reaction rate. The Langmuir-Hinshelwood model is a kinetic expression that is frequently used. This approach describes competing adsorption (O_2) and desorption (CO) on char surface that makes it more attractive. There are multiple forms for Langmuir-Hinshelwood, but it was shown by [61] that

$$r_c = \frac{k_2 k_1 P_{\mathrm{o2},s}^{n_r}}{k_1 P_{O_2,s}^{n_r} + k_2}, \tag{2.56}$$

yields good results, where k_1 and k_2 are Arrhenius rate constants as reported in Table 2.2, $n_r = 0.3$ and $P_{\mathrm{o2}s}$ is the partial pressure of oxygen at particle surface [61]. To determine the oxygen partial pressure at the surface of a particle the following equation is applied:

$$\frac{P_{\mathrm{o2}s}}{P} = \left(\frac{P_{\mathrm{o2}inf}}{P} - \gamma\right) exp\left(-\frac{r_c d_\mathrm{p}}{2 C_\mathrm{g} D_{\mathrm{O_2,g}}}\right) + \gamma, \tag{2.57}$$

where C_g and $D_{\mathrm{O_2,g}}$ are the gas phase concentration and diffusion coefficient of oxygen into the gas phase, respectively. The partial pressure of oxygen at the gas phase is represented by $P_{O_2,inf}$ and $\gamma = (\psi - 1)/2$.

The contributions of char oxidation process in species source terms are given by:

$$(S_{p,\mathrm{CO}})^{\mathrm{Oxid}} = \left(\frac{\mathrm{d}m_c}{\mathrm{d}t}\right)^{\mathrm{Oxid}} \times \frac{M_{w,\mathrm{CO}}}{M_{w,c}} \times \frac{\psi}{\mathrm{CO_2/CO}} \tag{2.58}$$

$$(S_{p,\mathrm{CO_2}})^{\mathrm{Oxid}} = \left(\frac{\mathrm{d}m_c}{\mathrm{d}t}\right)^{\mathrm{Oxid}} \times \frac{M_{w,\mathrm{CO_2}}}{M_{w,c}} \psi \tag{2.59}$$

$$(S_{p,\mathrm{O_2}})^{\mathrm{Oxid}} = -\left(\frac{\mathrm{d}m_c}{\mathrm{d}t}\right)^{\mathrm{Oxid}} \times \frac{M_{w,\mathrm{O_2}}}{M_{w,c}} \times \frac{1+\psi}{2} \tag{2.60}$$

To solve (2.56), (2.57), (2.55) Muller's method [23] and bisection method are applied. Muller method is a root-finding method that is based on determining the answer in the

neighborhood of the root using a quadratic polynomial. This method uses a quadratic equation to find three points near the root. If the Muller's method does not converge to the root after a certain number of iterations, bisection method will be applied to find the root. Applying bisecion method guarantees the convergence, however, it has more computational cost than Muller's method.

Gasification is an environment-friendly technology that provides efficient power from hydrocarbon fuels such as coal, biomass and oil residues. The complex geometry of coal makes the gasification modeling very complicated. The evolution of coal structure during gasification is studied by different researchers [101, 18]. Like char oxidation, the gasification process at elevated pressure was the subject of numerous studies [40, 9, 38, 19]. In this dissertation, gasification models at atmospheric pressure are considered.

Char oxidation and gasification are heterogeneous reactions that consume char. The presence of carbon dioxide and water vapor around the coal particle increases the likelihood of gasification reactions at high temperatures through

$$\mathrm{C_{(s)}} + \mathrm{CO_2} \longrightarrow 2\mathrm{CO} \ , \tag{2.61}$$

$$\mathrm{C_{(s)}} + \mathrm{H_2O} \longrightarrow \mathrm{CO} + \mathrm{H_2}. \tag{2.62}$$

The gasification process described in (2.62) is much slower than (2.61) and it is negligible. Nevertheless, the H_2O gasification (2.62) is also considered in this work. The differential equation describing char gasification is

$$\left(\frac{\mathrm{d}m_c}{\mathrm{d}t}\right)_i^{\mathrm{Gasif}} = -k_i m_{\mathrm{c}}; \quad i \equiv \mathrm{CO_2}, \mathrm{H_2O}, \tag{2.63}$$

where k_i is given by [102]

$$k_i = A_i P_i^{n_g} \exp\left(-\frac{E_i}{RT_{\mathrm{p}}}\right), \tag{2.64}$$

and P_i represents the partial pressure of CO_2 and H_2O around the particle for reactions (2.61) and (2.62), respectively. The Arrhenius rate parameters appearing in (2.64) are stated in Table 2.3. In this work, the evolution of particle surface area is accounted for using a modified random pore model [50, 60].

The species source terms for gasification are given by:

$$(S_{p,\mathrm{CO_2}})^{\mathrm{Gasif}} = -\left(\frac{\mathrm{d}m_c}{\mathrm{d}t}\right)_{\mathrm{CO_2}}^{\mathrm{Gasif}} \times \frac{M_{w,\mathrm{CO_2}}}{M_{w,c}} \tag{2.65}$$

$$(S_{p,\mathrm{CO}})^{\mathrm{Gasif}} = 2\left(\frac{\mathrm{d}m_c}{\mathrm{d}t}\right)_{\mathrm{CO_2}}^{\mathrm{Gasif}} \times \frac{M_{w,\mathrm{CO}}}{M_{w,c}} + \left(\frac{\mathrm{d}m_c}{\mathrm{d}t}\right)_{\mathrm{H_2O}}^{\mathrm{Gasif}} \times \frac{M_{w,\mathrm{CO}}}{M_{w,c}} \tag{2.66}$$

$$(S_{p,\mathrm{H_2O}})^{\mathrm{Gasif}} = -\left(\frac{\mathrm{d}m_c}{\mathrm{d}t}\right)^{\mathrm{Gasif}}_{\mathrm{H_2O}} \times \frac{M_{w,\mathrm{H_2O}}}{M_{w,c}} \tag{2.67}$$

$$(S_{p,\mathrm{H_2}})^{\mathrm{Gasif}} = \left(\frac{\mathrm{d}m_c}{\mathrm{d}t}\right)^{\mathrm{Gasif}}_{\mathrm{H_2O}} \times \frac{M_{w,\mathrm{H_2}}}{M_{w,c}} \tag{2.68}$$

The expression graph of the char oxidation and gasification model is illustrated in Figure 2.5.

2.2.4 Coal Heat Capacity

In this dissertation, coal particles consist of four main constituents (Figure 2.1): moisture, volatile, char and ash. It was assumed that coal heat capacity is the summation of its constituents heat capacity as stated in following:

$$C_{\mathrm{p}} = \frac{m_w C_w + m_v C_v + m_c C_c + m_{ash} C_{ash}}{m_{\mathrm{p}}}$$

where C_w, C_v, C_c and C_{ash} are heat capacity of water, volatile, char and ash, respectively. It was assumed that the heat capacity of all the constituents are only a function of particle temperature where temperature is uniform within the coal particle.

The relative change in particle temperature during the evaporation 2.2.1 process is small. It was assumed $C_w = 4200\ \frac{\mathrm{kJ}}{\mathrm{kg}}$. An equation to determine the volatile heat capacity is suggested by [53]:

$$C_v = 1500.5 + 2.9725 T_{\mathrm{P}}. \tag{2.69}$$

The equation to calculate the char heat capacity [55] is given by:

$$C_c = \frac{R}{M_{w,c}} \left[f_1\left(\frac{380}{T_{\mathrm{p}}}\right) + 2 * f_1\left(\frac{1800}{T_{\mathrm{p}}}\right) \right] \tag{2.70}$$

where $M_{w,c}$ is the molecular weight of char, R is the gas constant and $f_1()$ is

$$f_1(z) = \frac{z^2 e^z}{(e^z - 1)^2}. \tag{2.71}$$

The amount of ash is constant over the simulation and its heat capacity can be determined by [17]:

$$C_{ash} = 594 + 0.586 T_{\mathrm{P}}. \tag{2.72}$$

2.3 Interphase Exchange Terms

The change terms between coal particle and gas phase stated in conservation equations are defined in this section.

2.3.1 Intensive-Extensive Exchange

To facilitate the interphase coupling, a volume must be defined on each discrete segment of the ODT line to convert the extensive particle source terms to intensive terms.

The volume is defined in terms of the ODT grid spacing (Δy), diameter of the jet (D_j), coal feed rate and $\dot{m}_c$, as

$$V_{\text{cell}} = \Delta y A_{\text{cell}} = \Delta y D_j \frac{\dot{m}_c}{n_{\text{p}}} \tag{2.73}$$

where the number of particles in the simulation can be calculated by

$$n_{\text{p}} = \frac{\dot{m}_c \zeta_{\text{p}}}{\rho_{coal} \frac{\pi}{6} d_{\text{p}}^3}. \tag{2.74}$$

In (2.74), ρ_{coal}, d_{p} and ζ_{p} are the initial coal particle density, diameter and characteristic time, respectively.

Equation (2.74) is only applicable to the cases when the diameter is constant for all the particles. I suggest the mean particle diameter for d_{p} if a distribution of particles diameter is applied in the simulation. The n_{p} represents the number of particles that entered into the furnace through the jet within a characteristic time (ζ_{p}). The characteristic time explains the required time for one particle to completely enter into the furnace and is given by

$$\zeta_{\text{p}} = {}^{d_{\text{p}}}/_{u_{\text{p}}}, \tag{2.75}$$

where u_{p} is the particle velocity.

2.3.2 Momentum Exchange Terms

The momentum exchange terms, which appear in the gas and particle momentum balances, are

$$S_{\text{p}v} = -\frac{m_{\text{p}} f_{\text{d}}}{\tau_{\text{p}} \text{V}_{\text{cell}}} (v - v_{\text{p}}), \tag{2.76}$$

$$S_{\text{p}u} = -\frac{m_{\text{p}} f_{\text{d}}}{\tau_{\text{p}} \text{V}_{\text{cell}}} (u - u_{\text{p}}), \tag{2.77}$$

where $\tau_{\text{p}} = \frac{d_{\text{p}}^2}{18\nu_{\text{g}}}$ is the particle relaxation time [13] and f_{d} is the drag force coefficient. The model employed for f_{d} is

$$f_{\text{d}} = \begin{cases} 1 & Re_{\text{p}} < 1 \\ 1 + 0.15 Re_{\text{p}}^{0.687} & 1 < Re_{\text{p}} < 1000 \\ 0.0183 Re_{\text{p}} & Re_{\text{p}} > 1000 \end{cases},$$

where

$$Re_{\text{p}} = \frac{\text{d}_{\text{p}} |u_{\text{p}} - u_{\text{g}}|}{\nu_{\text{g}}} \tag{2.78}$$

is the particle Reynolds number and ν_{g} is the gas kinematic viscosity. Subscripts p and g indicate particle and gas phase properties, respectively.

2.3.3 Mass exchange terms

Most of the particle mass (except ash) is released to the gas phase during the combustion process. Furthermore, char oxidation and gasification require additional species from the gas phase such as oxygen and carbon monoxide. The mass source term for single particles for species i can be written as

$$S_{\mathrm{p}Y_i} = \left(\frac{\mathrm{d}m_i}{\mathrm{d}t}\right)^{\mathrm{Evap}} + \left(\frac{\mathrm{d}v_i}{\mathrm{d}t}\right)^{\mathrm{Dev}} + \left(\frac{\mathrm{d}m_i}{\mathrm{d}t}\right)^{\mathrm{Oxid}} + \left(\frac{\mathrm{d}m_i}{\mathrm{d}t}\right)^{\mathrm{Gasif}}. \tag{2.79}$$

Models for evaporation, devolatilization, and char oxidation/gasification in (2.79) are discussed in §2.2.

During the combustion almost all of particle mass except the ash part will be released to gas phase. Also, char oxidation and gasification reactions need certain species from gas phase such as O_2 and CO_2 that get consumed by them. The species source terms are mentioned in Table 2.4.

2.3.4 Energy exchange terms

The energy source term for the gas phase energy conservation equation, (2.4), is given as

$$\begin{aligned} S_{\mathrm{pe}_0} &= \alpha\left(S_{\mathrm{p,CO}}\Delta H_{\mathrm{CO}} + S_{\mathrm{p,CO_2}}\Delta H_{\mathrm{CO_2}}\right)^{\mathrm{Oxid}} \\ &+ \alpha\left(\frac{\mathrm{d}m_{\mathrm{c}}}{\mathrm{d}t}\right)_{\mathrm{H_2O}} \Delta H^{\mathrm{Gasif}}_{\mathrm{H_2O}} \\ &+ \alpha\left(\frac{\mathrm{d}m}{\mathrm{d}t}\right)_{\mathrm{CO_2}} \Delta H^{\mathrm{Gasif}}_{\mathrm{CO_2}}, \end{aligned} \tag{2.80}$$

where α is the fraction of heat released to the gas and $1-\alpha$ is the fraction of heat absorbed by the particle. In this study, $\alpha = 0.3$ was used. For all of the conditions explored in this work, the value of α has negligible impact on the predicted ignition delay since the devolatilization (not char oxidation) rate is the dominant factor determining the ignition delay. However, in situations where char oxidation becomes dominant, the value of α will play an important role. The source term in (2.80) includes the heat of char oxidation (exothermic) CO_2 and H_2O gasification (endothermic).

Finally, the source term appearing in the particle energy balance, (2.17), is written as

$$
\begin{aligned}
S_r &= \frac{1-\alpha}{m_{\mathrm{p}} C_{\mathrm{p}}} \left(S_{\mathrm{p,CO}} \Delta H_{\mathrm{CO}} + S_{\mathrm{p,CO_2}} \Delta H_{\mathrm{CO_2}}\right)^{\mathrm{Oxid}} \\
&+ \frac{1-\alpha}{m_{\mathrm{p}} C_{\mathrm{p}}} \left(\frac{\mathrm{d}m_{\mathrm{c}}}{\mathrm{d}t}\right)^{\mathrm{Gasif}}_{\mathrm{H_2O}} \Delta H^{\mathrm{Gasif}}_{\mathrm{H_2O}} \\
&+ \frac{1-\alpha}{m_{\mathrm{p}} C_{\mathrm{p}}} \left(\frac{\mathrm{d}m_{\mathrm{c}}}{\mathrm{d}t}\right)^{\mathrm{Gasif}}_{\mathrm{CO_2}} \Delta H^{\mathrm{Gasif}}_{\mathrm{CO_2}} \\
&+ \frac{1}{m_{\mathrm{p}} C_{\mathrm{p}}} \left(S_{\mathrm{p,H_2O}}\right)^{\mathrm{Evap}} \lambda_{\mathrm{Evap}}, \qquad (2.81)
\end{aligned}
$$

where ΔH is the enthalpy of heterogeneous reaction reported in Table. 2.5, λ_{Evap} is water's latent heat of vaporization and $\left(S_{\mathrm{p,H_2O}}\right)^{\mathrm{Evap}}$ is defined in (2.19).

2.3.4.1 α value

Heterogeneous reactions at the particle surface, such as char oxidation and gasification, release significant amounts of heat. The produced heat is partially absorbed by the particle and the rest releases to the carrier (gas) phase. The α value represents the fraction of heat released to the gas, whereas $1-\alpha$ is the fraction of heat absorbed by the particle. In this work, the gradients of energy and mass inside the particle are not considered, meaning particles have the same temperature and composition at the surface and the core.

In this dissertation, a certain value (0.3) is used for α, and the author suggests a method to determine a dynamic value for α during the simulation. The heat of homogenous reactions release to the gas phase by convective heat transfer and also absorb into the particle by conducive heat transfer. The α value can be represented by following equation:

$$
\alpha = \frac{h_c D}{h_c D + k} = \frac{h_c D/k}{(h_c D + k)/k} = \frac{Bi}{Bi + 1} \qquad (2.82)
$$

where h_c and k are the convective and conductive heat transfer coefficient, respectively. The Biot number (Bi) represents the ratio of convection to conductive heat transfer. For Biot numbers smaller than 0.1, it can be assumed that the inside of the particle has an uniform temperature.

For simulations performed in Chapter 3, the value of α has negligible impact on the ignition delay time since the mode of ignition is homogenous for all the performed simulations. In Figure 2.6 the particle and gas phase (at the particle position) temperatures are illustrated for $\alpha = 0$ and $\alpha = 1$. Figure 2.6 shows that the predicted particle and gas phase temperature do not notably change before the characterized ignition time by varying α from 0 to 1.

However, the impact of α on the physics of combustion is significant when the char oxidation process becomes active. The α value not only changes the fate of coal particles

but also has notable influence on the gas phase. Figure 2.7a shows the normalized mass of volatile and char for α value of 0 and 1 at given time. The activation of char oxidation after 12 seconds highlights the impact of α value on the behavior of the coal particle. In this work, $\alpha = 1$ means all the heat produced by char oxidation are absorbed by the particle, therefore using $\alpha = 1$ increases the particle temperature notably compared to $\alpha = 0$. In Figure 2.7.b temperature of particle and gas phase (of the case $A.1$ shown in Figure 2.6) are illustrated for $\alpha = 0$ and $\alpha = 1$ in a wider time window. The char oxidation accelerates by increase in particle temperature, which implies more heat production by this process. The heat produced by char oxidation increases the gas phase temperature by convection heat transfer. Furthermore, higher particle temperature implies higher devolatilization rate, hence more homogenous reactions are expected. However, at time = 18 sec, the particle temperature profile using $\alpha = 1$ becomes smooth and crosses the particle temperature using $\alpha = 0$. The smoothness of particle temperature using $\alpha = 1$ can be explained by lack of oxygen around the particle. As explained, value of α implies different physics to the system and changes the fate of particle and gas phase significantly.

2.4 Turbulence Model

In ODT, turbulent mixing is modeled through a series of stochastic eddy events, or simply, "eddies" [41, 93]. By construction, eddies conserve momentum, energy and mass over the interval on which they act. Their size(ℓ_e), lifetime (τ_e) and location are influenced by the local energetics of the flow field [41, 93]. This allows the ODT model to naturally capture key turbulence properties such as the $-5/3$ energy cascade in isotropic turbulence [41]. The frequency at which eddies occur is dictated by eddy rate distribution:

$$\lambda = \frac{C}{\ell_e^2 \tau_e}, \tag{2.83}$$

which is directly influenced by the "eddy rate constant" (C). The impact of the value chosen for C on the model's ability to capture statistics in turbulent jets was studied by [74].

The particle-eddy interaction is considered in this work using a continuos formulation of Type-C interaction proposed by Schmidt [79]. Further details of the model are described by [74].

2.5 Conclusions

The intention of this chapter is to provide a reference for those interested in coal combustion/gasification modeling. The chemistry models determining homogenous reactions in the

gas phase are also described. A new formulation for infinity-fast chemistry is proposed in this chapter. A summary of ODT framework (an Eulerian formulation) is briefly discussed, more details can be found in [74].

The coal submodels description are not limited to ODT framework and can be applied to other platforms. The source terms that couple the gas and coal particle phase are reported here. A formulation is proposed to exchange source between gas and particle phases where the variables are intensive and extensive, respectively. This formulation follows the principals and basic ideas applied to develop ODT.

The impact of α value on the single coal particle combustion is studied. α represents the fraction of heat absorbed by the particle during heterogeneous reactions (char oxidation/gasification). It was shown that the value α can significantly alter the simulation prediction when the char oxidation becomes active. However, for the cases studied in Chapter 3, it does not have any notable impact since the focus of the study is on the devolatilziation process and homogenous reactions.

Furthermore, the expression graph of the coal submodels provides information on the expression dependencies and tag name. The expression graphs included in this chapter can be helpful for those interested in the further development of the code, and also eases the code learning. In addition, it reflects the applied method and complexity of models.

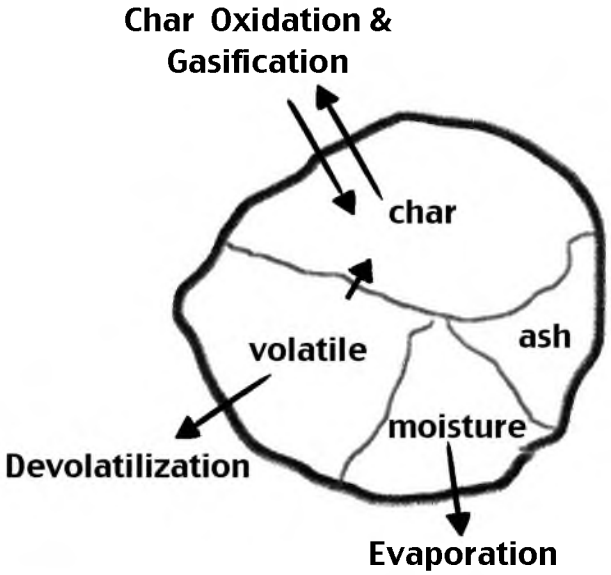

Figure 2.1: Coal constituents.

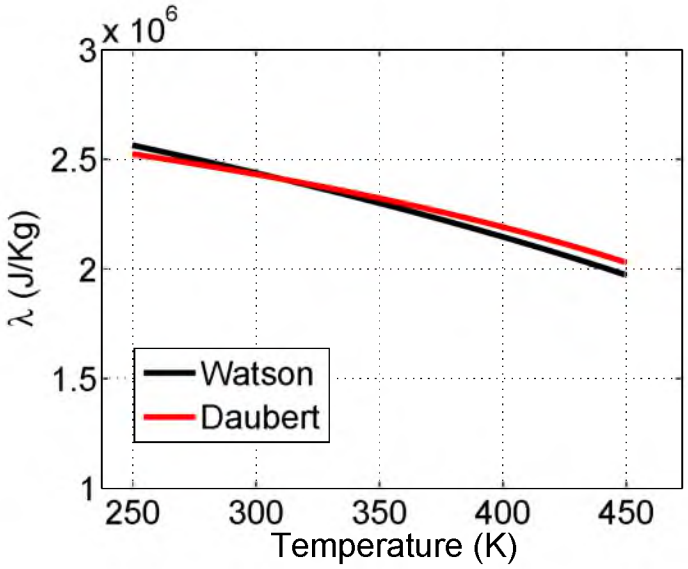

Figure 2.2: Latent heat of vaporization (λ) predicted by Watson model (black line) and Daubert model (red line).

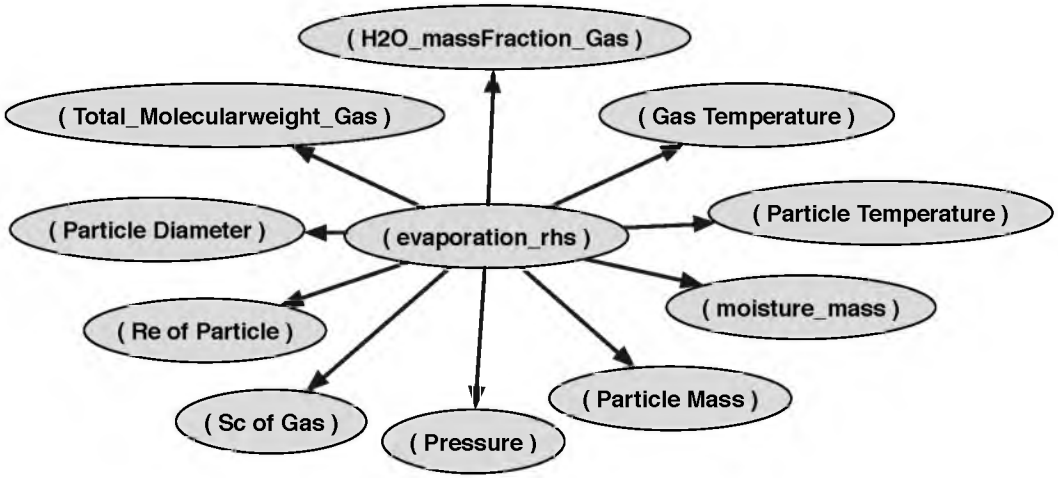

Figure 2.3: Expression graph of evaporation model.

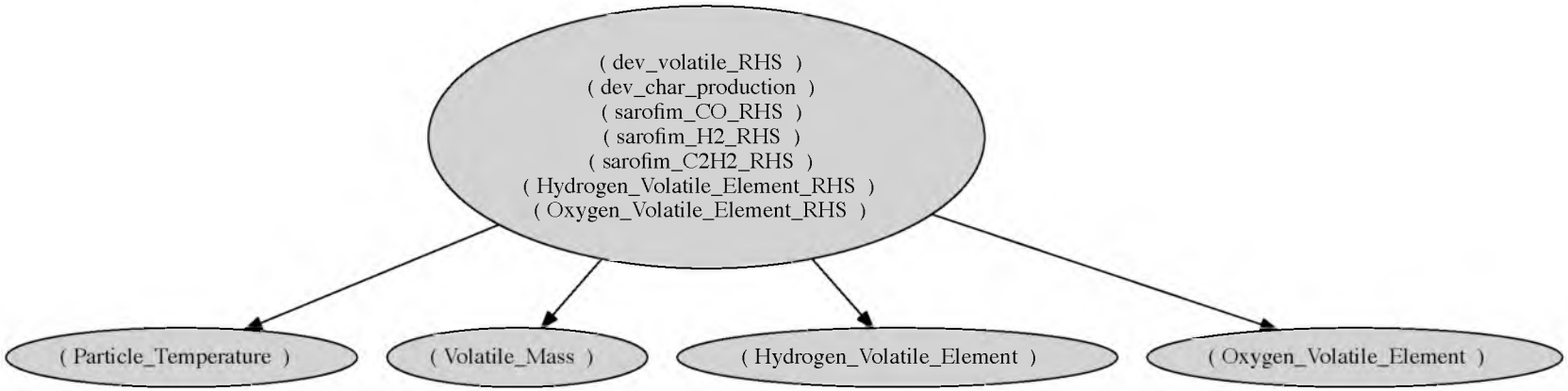

Figure 2.4: Expression graph of Kobayashi-Sarofim devolatilization model.

Table 2.1: CPD composition[37]

Specie	bond	primary functional group source	$A(s^{-1})$	E/R(K)
CO_2	extra loose	carboxyl	0.56×10^{15}	30,000 ± 1500
	loose	carboxyl	0.65×10^{17}	33,850 ± 1500
	tight	carboxyl	0.11×10^{16}	38,315 ± 2000
H_2O	loose	hydroxyl	0.22×10^{19}	32,700 ± 1500
	tight	hydroxyl	0.17×10^{14}	32,700 ± 1500
CO	ether loose	ether O	0.14×10^{19}	40,000 ± 6000
	ether tight	ether O	0.15×10^{16}	40,500 ± 1500
	extra tight	ether O	0.20×10^{14}	45,400 ± 1500
HCN	loose		0.17×10^{14}	30,000 ± 1500
	tight		0.69×10^{13}	42,500 ± 4750
NH_3			0.12×10^{13}	27,300 ± 3000
C_2H_2		H(al^2)	0.84×10^{15}	30,000 ± 1500
CH_4	extra loose	methoxy	0.84×10^{15}	30,000 ± 1500
	loose	methyl	0.75×10^{14}	30,000 ± 2000
	tight	methyl	0.34×10^{12}	30,000 ± 2000
H		H(ar^3)	0.10×10^{15}	40,500 ± 6000

Table 2.2: Arrhenius parameters for equation (2.56)

	A (mol/sm^{2}atm^n)	E (kJ/mol)
k_1	93.0	0.1
k_2	26.2	109.9
n	0.3	

Table 2.3: Arrhenius parameters for the gasification reactions used in (2.64) by [38, 102].

	CO_2		H_2O	
	$T < 1473$	$T \geq 1473$	$T < 1533$	$T \geq 1533$
E (J/kmol)	2.71×10^8	1.63×10^8	2.52×10^8	1.40×10^8
A $\left(\text{kg.s}^{-1}.\text{pa}^{-n_g}\right)$	3.34×10^8	6.78×10^4	2.89×10^8	8.55×10^8
n_g	0.54	0.73	0.64	0.84

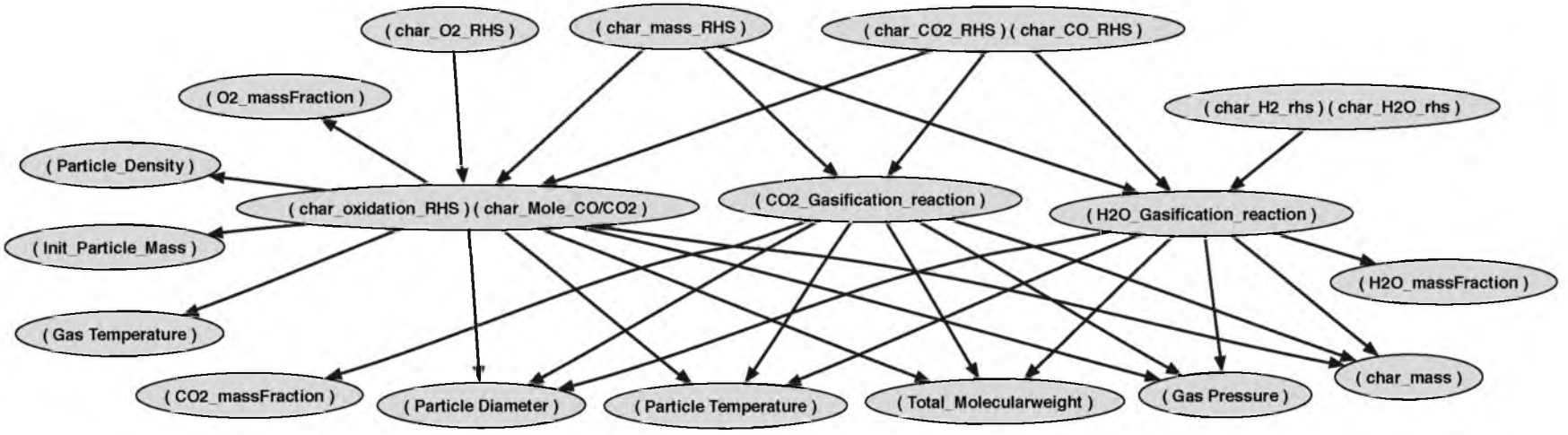

Figure 2.5: Expression graph of char oxidation and gasification model.

Table 2.4: Species source terms.

Specie $S_{p,i}$	Vaporization	Devolatilization			Char	
		Single Rate	Kobayashi-Sarofim	CPD	Oxidation	Gasification
CO_2				$(S_{p,CO_2})^{CPD}$	$(S_{p,CO_2})^{Oxid}$	$(S_{p,CO_2})^{Gasif}$
CO		$(S_{p,CO})^{SR}$	$(S_{p,CO})^{Kob}$	$(S_{p,CO})^{CPD}$	$(S_{p,CO})^{Oxid}$	$(S_{p,CO})^{Gasif}$
O_2					$(S_{p,O_2})^{Oxid}$	
H_2O	$(S_{p,H_2O})^{Evap}$			$(S_{p,H_2O})^{CPD}$		$(S_{p,H_2O})^{Gasif}$
H_2		$(S_{p,H_2})^{SR}$	$(S_{p,H_2})^{Kob}$			$(S_{p,H_2})^{Gasif}$
HCN				$(S_{p,HCN})^{CPD}$		
CH_4				$(S_{p,CH_4})^{CPD}$		
C_2H_2				$(S_{p,C_2H_2})^{CPD}$		
NH_3				$(S_{p,NH_3})^{CPD}$		
H				$(S_{p,H})^{CPD}$		

Table 2.5: Reaction enthalpy of heterogeneous reactions.

	Oxidation		Gasification	
	CO_2	CO	H_2O (eq. 2.62)	CO (eq. 2.61)
ΔH(kJ/kg)	33075.72	9629.64	10.94×10^3	14.37×10^3

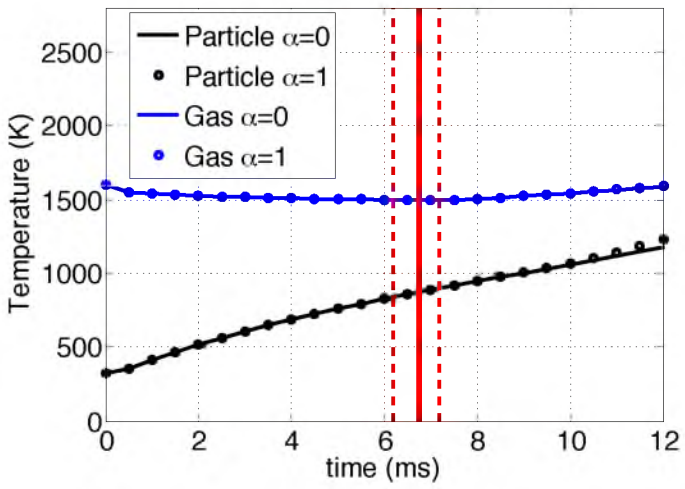

Figure 2.6: Temperatures of particle and gas phase at the particle position. The red lines represent characterized ignition delay, dash lines show the associated sensitivity bars.

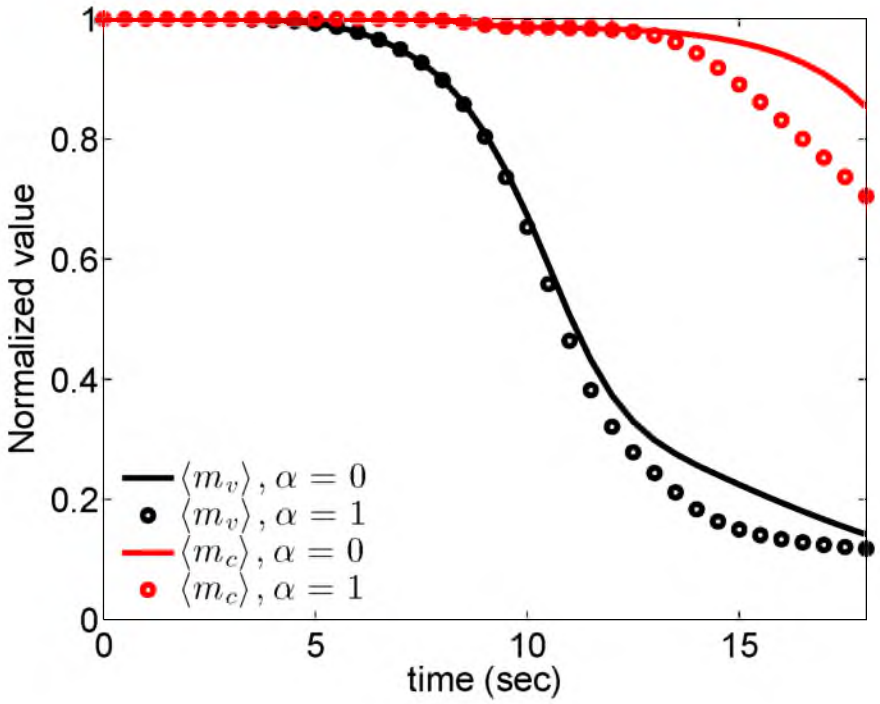

(a) Normalized volatile and char mass.

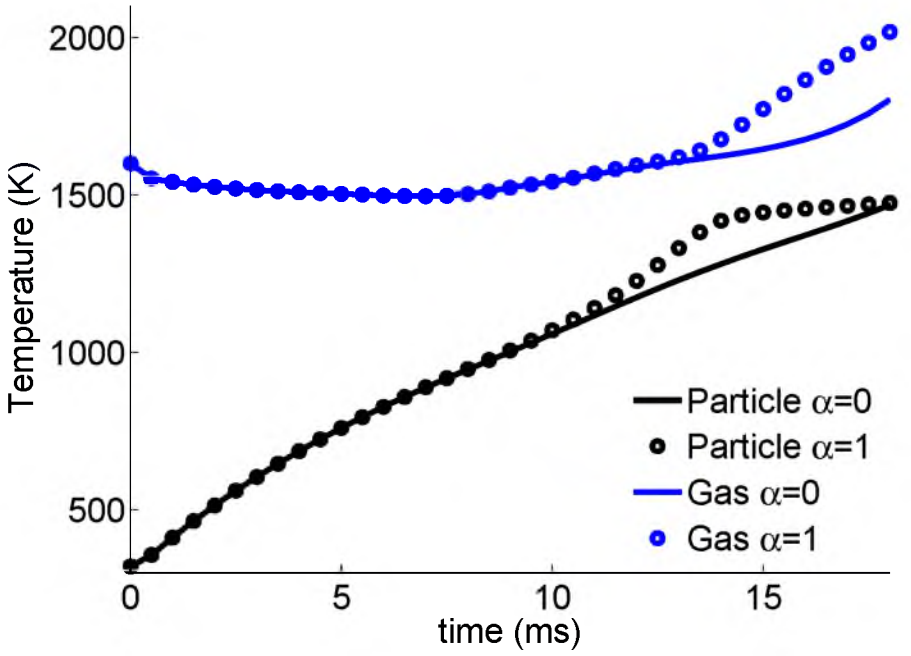

(b) Particle and gas (at particle position) temperature.

Figure 2.7: Impact of α on particle and gas phase.

CHAPTER 3

SINGLE COAL PARTICLE COMBUSTION

"*In the existing sciences whenever a phenomenon is encountered that seems complex it is taken almost for granted that the phenomenon must be the result of some underlying mechanism that is itself complex. Buy my discovery that simple programs can produce great complexity make it clear that this not in fact correct.*"

-Stephen Wolfram, A New Kind of Science

The objective of this chapter is to evaluate the efficacy of devolatilization and gas-phase chemistry models for coal combustion/gasification. To avoid complexity of the large/pilot scale combustor where the turbulence has a considerable impact on the combustion behavior, an experiment conduced in laminar flow is selected.

To this end, we compared experimental observations of coal particle ignition delay to two devolatilization models paired with two gas-phase kinetics models.

3.1 Introduction

Coal combustion/gasification is a complex process with many coupled subprocesses occurring simultaneously [89]. Furthermore, most practical coal combustion systems are turbulent, further complicating the modeling challenge because of the nonlinear coupling occurring across a multitude of length and time scales. Even with modern day computers, resolving the entire physics of the problem remains prohibitively expensive. Coal combustion/gasification models must address particle dynamics in turbulent flow, gas-phase thermochemistry, heterogeneous reactions between the coal and gas, devolatilization/pyrolysis, vaporization, radiative heat transfer, *etc.*

The modeling challenge for coal combustion is further complicated by the varying properties and chemical structure of different coal types [17], and by the fact that the coal properties change significantly throughout a coal particle's lifetime in a combustor

[57, 101, 84]. The coal particle thermochemistry in this work is divided into three processes: vaporization, devolatilization and char oxidation/gasification.

Models for devolatilization vary widely in complexity, with the most sophisticated models accounting for the chemical structure of the coal and its effect on the devolatilization process [89]. In 1971, a constant value was proposed for the combustion rate of each coal type [5]. Arrhenius-form models such as the single-rate [4] and Kobayashi [45] models describe devolatilization with a kinetic rate. In 1976, the Distributed Activation Energy (DAE) model [3] proposed using a gaussian distribution for the activation energy. Determining the parameters for the gaussian distribution were the challenges of this model [70]. Representing coal as a collection of functional group including aromatic rings, aliphatic chains and bridges and oxygen-carrying groups was a significant step in devolatilization modeling [21, 91]. The Chemical Percolation Devolatilization (CPD) model accounts for the thermal decomposition of the macromolecular network and accounts for structural variation among various coal types [25, 6, 89]. It can accurately describe light-gas evolution from coal devolatilization [37]. In this work, the Kobayashi and CPD devolatilization models (representing a relatively simple and fairly sophisticated model, respectively) are utilized; their ability to predict ignition delay are examined.

Char oxidation and gasification are heterogenous reactions, and are significantly slower than the vaporization and devolatilization processes [89, 88]. There are many factors that influence char oxidation, such as coal structure, coal type, the gas-phase environment (*e.g.*, oxygen partial pressure) and temperature [61, 52]. The products of char oxidation are mainly carbon dioxide and monoxide [56, 95]. A common assumption in coal combustion modeling is that char oxidation occurs after the coal particle is fully devolatilized [98, 97]. The present study and formulation allow for simultaneous vaporization, devolatilization and char oxidation and do not impose any temporal ordering/sequencing of these processes.

The influence of system parameters such as oxidizer composition and coal rank on ignition delay and flame stability have been explored experimentally by several researchers [48, 54, 51, 36, 43, 44, 72]. A review on experiments measuring the coal particle ignition delay is reported in [11]. In [51], the influence of gas phase temperature and particle size on the single particle ignition delay are also considered as parameters. In this work, the ignition delay is employed as a metric to evaluate simulation results where the effect of gas phase temperature, coal rank and particle size on ignition delay are studied and compared to the experiments conducted by [51].

Although numerous simulations of coal combustion have beed performed, most use

relatively simple models for the devolatilization and gas-phase combustion process [99, 31, 107, 47, 100]. The flamelet and flame-sheet models are used in simulation of single coal particle combustion by different groups [33, 47, 99]. Attempts to address limitations of these models have used two- and four-step global mechanisms [36]. [30, 27, 28] performed one-dimensional simulations on char oxidation of single coal particles with detailed kinetics to determine the temperature and species radial profiles for char oxidation, but used boundary-layer assumptions to treat diffusion.

3.2 Computational Configuration

This section briefly summarizes the computational parameters, models and configurations used for each simulation performed in this chapter. The computational configuration mirrors the experimental setup described in [51]. A schematic of the facility reported by the experiment [61] is given in Figure 3.1. It is an atmospheric furnace located at Sandia's optical entrained flow reactor facility. The detailed description of the flow reactor illustrated in Figure 3.1 is provided in [58].

Figure 3.2 shows the photographs taken in the experiment where Black Thunder coal with sizes cut of 75-105 μm is combusted in 12 vol.% O2 and a gas temperature of 1230 K. In this figure, the impact of coal feed rate was the subject of study where the coal feed is increased from left (a) to right (i).

The governing equations and models outlined in Chapter 2 are solved using a fully coupled, compressible algorithm with an explicit time integration scheme and a second-order finite volume spatial discretization. Characteristic boundary conditions are applied on the domain boundaries [92]. For the simulations reported herein, the computational domain is 1.4 cm with a grid spacing of 140 μm and time step of 2×10^{-8} s. The results presented herein are grid-converged; simulations performed on finer grids yield the same result for predicted ignition delay.

A schematic of the simulated system is illustrated in Figure 3.3 where the one-dimensional domain oriented in the y-direction moves in the x-direction via a space-time mapping using the mean system velocity [93].

In this chapter, two US coals are used: Pittsburgh high-volatile bituminous coal and Black Thunder subbituminous coal from the Powder River basin, with proximate and ultimate analysis reported by [51]. The coal particles are assumed to be spherical, with initial density of 1200 kg/m^3 and initial temperature of 298 K for all simulations.

The initial gas composition and temperature are uniform and constant over the computational domain, consistent with the experimental configuration described in [51]. Table

3.1 summarizes the key parameters varied as part of this work. The initial gas phase composition includes O_2, N_2, CO_2 and H_2O. The effect of O_2 composition is considered while maintaining the initial CO_2 and H_2O mole fractions constant at 0.3 and 0.116, respectively. Likewise, the initial streamwise velocity ($v = 2.5\,\mathrm{m/s}$) is uniform and constant over the domain, but evolves in time according to (2.3), with dilatational effects due to chemical reaction as well as particle vaporization, devolatilization and char oxidation accounted for. Cases $A.1$-$A.8$ each consider the effect of the initial gas phase temperature on the ignition delay, resulting in a number of distinct simulations being performed for each of these cases. Similarly, each case, $B.1$-$B.4$, includes several simulations of particle sizes varying from 45-125 μm.

3.3 Results Analysis

The experiments were conducted to observe the physics associated with combustion of single particle which implies the interaction of subsequent particles is negligible. To examine the validity of this assumption a scaling analysis is made here.

The distance between subsequent particles can be obtained by (3.1)

$$\Delta z_{\mathrm{p}} = \Delta t \times u \tag{3.1}$$

where Δz_{p} and Δt are the distance and elapsed time between the subsequent particles. The Δt can be calculated by :

$$\Delta t = \frac{m_{\mathrm{p}}}{\dot{m}_{\mathrm{p}}} \tag{3.2}$$

where $\dot{m}_{\mathrm{p}}$ is the mass flow rate of particles and m_{p} is the particle mass. The characteristic length represents the length required between subsequent particles to avoid any interaction, given by:

$$z_c = \sqrt{D \times \Delta t} \tag{3.3}$$

where D is the mass diffusion coefficient and z_c is the characteristic length. Figure 3.4 shows the comparison between the z_c and z_{p}, that the distance between subsequent particles is longer than the characteristic length at all simulated coal feed rates. This ensures that the subsequent particles do not affect each others behavior and the observed physics are associated to a single coal particle.

Simulations were performed to investigate the effect of furnace temperature, particle size and coal type on ignition delay of coal particles. Furthermore, for particle and gas phase calculation, two methods with different levels of complexity and computation cost

are utilized. To validate the simulation predictions, ignition delay as a metric is identified to compare the simulation results with experimental data.

Figure 3.5 shows the normalized volatile and char content of the coal particle for case $B.1$, and also indicates the location of ignition[1]. This figure suggests that the ignition is characterized almost entirely by homogeneous reactions rather than heterogeneous char reactions.

Figure 3.6 illustrates the spatio-temporal evolution of several fields for case $B.1$ (in Table 3.1) with a particle size of 92.4 μm. To show more detail on species evolution, the profiles of OH, CO and CH_4 at 30, 40 and 45 ms are illustrated in Figure 3.7.

During the first 25 ms, the gas phase temperature (Figure 3.6a) decreases due to the cooler particle absorbing heat prior to the onset of ignition near 25 ms. The mass fraction of carbon monoxide (Y_{CO}) is illustrated in Figure 3.6b. Devolatilization produces CO as the particle heats up during $t = [0, 25]$ ms, with a spike in CO production around 25-30 ms as homogenous ignition occurs in the gas phase. After homogenous ignition, when the temperature of the particle and gas phase is high, char oxidation dominates CO production. Figure 3.6c shows the O_2 space-time evolution, which is consistent with the interpretation discussed in connection with the CO evolution. Gas phase (homogenous) reaction and char oxidation (heterogeneous) both contribute to the O_2 consumption, with homogenous reactions dominating initially and heterogeneous reactions dominating after homogeneous ignition. The evolution of OH, shown in Figure 3.6d, supports the observation that homogeneous ignition first occurs away from the particle surface, followed by heterogeneous char oxidation.

In Figure 3.7 at time 30 ms OH has two local maxima (indicated by black arrows) and CH_4 has two corresponding maxima where homogenous reaction of volatiles begins. These maxima correspond to the two branches in Figure 3.6d during $t \approx [27, 35]$ ms. By 40 ms, the released volatiles are consumed, as shown by Figure 3.7c (here, CH_4 is chosen to represent the volatiles produced by the CPD model). The two local minima at 45 ms in the OH profile in Figure 3.7a (see the blue arrows) correspond to the homogenous reactions with the byproducts (primarily CO) of char oxidation.

3.4 Ignition Delay Definition

In experiments, the most widely used methods to identify ignition delay are based on measurements of the intensity of visible light emission [34, 51]. In the experimental

[1]Section 3.4 discusses the characterization of ignition in detail.

results used in this work, CH^* emission is considered as an indicator of ignition, with the ignition point defined as half of the CH^* maximum signal [51]. However, this signal was contaminated by $CO_2{}^*$ and thermal radiation from hot soot and the coal/char particle [51].

Computationally, it is not obvious how to determine the ignition point, for example, threshold values of temperature or species mass fractions, or the inflection point in the particle temperature-time history (as suggested by [34]). Physically, the inflection point in the particle temperature history represents the location where the asymptotic heating of the particle by its surroundings is overtaken by the heat transfer due to chemical reaction nearby the particle.

Figure 3.8a shows the simulation prediction for ignition delay based on several plausible criteria. These results are for the same conditions as described in connection with Figure 3.6, but with the inlet gas temperature varying. For the species criteria, ignition is defined as the time at which the species mass fraction is 50% of its maximum value. CO is chosen to be representative of the products of devolatilization and char oxidation and CH is chosen as a surrogate representation of CH^*, which is the reported basis of the experimental measurements of ignition delay.

The bars in Figure 3.8a represent 25% and 75% of the maximum mass fraction in the profiles of species, consistent with the approach taken in [51]. These "uncertainties" or sensitivities are not obtained through rigorous uncertainty or sensitivity analysis, as that is beyond the scope of this work. Rather, they are provided to give an indication of the sensitivity of the reported ignition delay to the chosen definition.

The time-evolution of these species and the particle temperature at the particle position are shown in Figure 3.8b. Since the ignition delay criteria based on CH provides the best agreement between the simulation and experimental data, it is used to identify the ignition delay throughout the chapter where detailed kinetics are utilized in the gas phase, unless specifically stated otherwise.

The CH criteria is unavailable in flame-sheet method (discussed in §2.1.2) because intermediate species are not available. Therefore, CO and the particle temperature history inflection point as measures of ignition delay were used. As shown in Figure 3.8, these are not expected to be highly accurate indicators of ignition delay, but provide a reasonable approximation. By assuming that the true ignition delay prediction for the flame-sheet method lays between the CO and particle inflection point, a comparison between detailed kinetics and flame-sheet can be made.

3.5 Effect of Furnace Temperature

Using the ignition delay criteria established in §3.4, the effect of furnace temperature on ignition delay for Pittsburgh and Black Thunder coals[2] is investigated. The simulation parameters and applied models for this study are give in Table 3.1, which includes cases $A.1$ to $A.8$.

The experiments considered a particle size cut of 75-105 μm, whereas the simulation adopts particles at the mass mean size of the size cut (92.4 μm). The model prediction of ignition delay as a function of particle size is considered in §3.6.

3.5.1 Detailed Chemistry

Figure 3.9a shows the ignition delay as a function of furnace temperature for Pittsburgh (Figure 3.9a) and Black Thunder (Figure 3.9b) coals, respectively. Results for the CPD and the Kobayashi models, both with detailed chemistry in the gas-phase, are compared with experimental data. Figure 3.9 indicates that the CDP model is more successful than the Kobayashi model in predicting the ignition delay over the range of furnace temperatures and the two coal types, with larger discrepancies at higher furnace temperatures.

Figure 3.10 shows the particle temperature at ignition using the inflection point and CH_x criteria (see §3.4) with the CPD model and detailed chemistry in the gas phase, and indicates that ignition occurs at lower particle temperatures as the furnace temperature increases. Figure 3.10 also shows the results using the particle temperature inflection point criteria as an ignition definition, and demonstrates that the inflection point criterion results in significantly different particle temperatures at ignition. Furthermore, the sensitivity in particle temperature at ignition point is quite high at low furnace temperatures. All of this highlights the importance of carefully characterizing ignition, and also the potential difficulty of comparing computational and experimental data if simulations do not predict the same quantity being observed by the experiment.

The volatile consumption fractions at the ignition point for both devolatilization models are reported in Figure 3.11. The CPD model shows a much more pronounced effect of the furnace temperature on the volatile consumption fraction at ignition. As a consequence of producing highly reactive species such as H, the consumption fraction of CPD model at high temperature is lower than the Kobayashi model. The particle temperature at ignition point decreases as initial furnace temperature increases in Figure 3.10, which can be explained by the fact that less volatile is required for ignition as furnace temperature increases.

---

[2]The proximate and ultimate analysis for these coals was taken from [51].

3.5.2 Flame-Sheet Model

We now consider the flame-sheet model for the gas-phase chemistry treatment. As a very inexpensive model, this is attractive for use in large-scale simulations, provided that it is sufficiently accurate. As discussed in §3.4, the CO profile at particle position and inflection point in particle temperature history are used to identify the ignition point since the flame-sheet model does not provide CH_x radical species for comparison with the experimental measurements.

Figure 3.12 shows the ignition delay as a function of furnace temperature, analogous to the results shown in Figure 3.9 for detailed gas-phase chemistry. The difference between the CPD and Kobayashi models is not as pronounced when flame-sheet chemistry is used in the gas phase as when detailed kinetics are used (see Figure 3.8a). Overall, the flame-sheet model paired with either devolatilization model does not perform as well as the detailed chemistry treatment paired with the CPD model, and fails to capture the nonlinear trend of ignition delay as a function of furnace temperature that the data show. Some of this discrepancy can be attributed to the lack of a suitable metric for ignition delay with the flame-sheet model, as discussed in §3.4.

3.6 Particle Size Effects

The experimental data were obtained on particle sizes in different ranges [51], giving some uncertainty as to the effect of particle size variation within the cut on the resulting ignition delay. The effect of particle size on ignition delay for an initial furnace temperature of 1320 K is illustrated in Figure 3.13. The triangles connected by dash-dot lines indicate experimentally measured ignition delay for the three different particle size cuts used in the experiments [51]. Also shown are the computational results for particles of different sizes.

Figure 3.13a compares experimental data to results for the CPD and Kobayashi models with detailed gas-phase chemistry (cases $B.1$ and $B.2$ in Table 3.1). The models show a larger effect of particle size on ignition delay than is observed experimentally. Nevertheless, the CPD model with detailed gas-phase chemistry does compare more favorably with the experimental data than the Kobayashi model. For comparison, the ignition delay trends using the flame-sheet model (cases $B.3$ and $B.4$ in Table 3.1) are shown in Figure 3.13b. Consistent with results discussed in §2.1.2, the flame-sheet model paired with either of the devolatilization models is not as accurate as the detailed kinetic model paired with CPD.

3.7 Conclusions

This chapter considered several models for single coal particle ignition and compared these to experimental measurements available in the literature for two coal types at various furnace temperatures and for several particle sizes. Two models for devolatilization (CPD and the Kobayashi-Sarofim model) and two for the gas phase chemistry treatment (detailed kinetics and a flame-sheet model) were applied. These models essentially trade complexity for cost.

To the author's knowledge, this is the first simulation performed using detailed kinetics in the gas phase fully coupled to a high-fidelity model (CPD) for devolatilization of coal particles. The CPD model attempts to predict the light-gas evolution for the coal particles.

The results indicate that simpler Kobayashi-Sarofim and flame-sheet models roughly capture general trends present in the experimental data, but fail to provide quantitative agreement. On the other hand, the CPD model paired with detailed gas-phase chemistry provides reasonable agreement with the experimental observations over all reported conditions. This suggests that detailed devolatilization and gas-phase chemistry modeling are important to provide accurate characterization of ignition delay. This conclusion also applies when considering the ability of the models to capture trends when varying furnace temperature and particle size.

The amount of volatile produced by each devolatilization model at ignition is compared, and varies significantly between the CPD and Kobayashi-Sarofim models, with the CPD model showing much more sensitivity to the gas phase temperature in predicting the volatile yield at the point of ignition.

One significant challenge in comparing to experimental data is determining how to define ignition in the simulation. This is particularly challenging for the flame-sheet model where intermediate species are unavailable for comparison against the emission measurements of CH^* in the experiment. A rough indication of the sensitivity of the model predictions to the definition of the ignition delay are also presented.

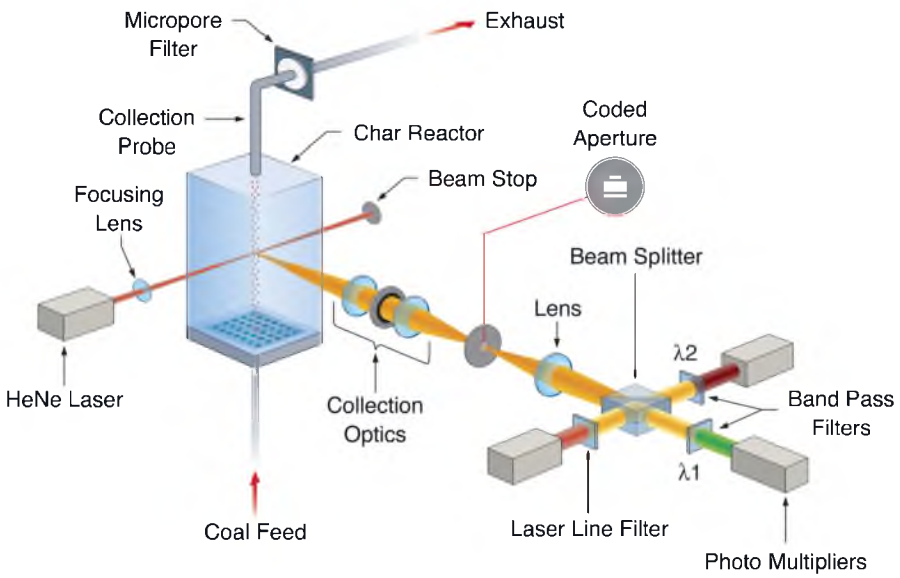

Figure 3.1: Schematic diagram of Sandia's char kinetic entrained flow reactor. Adapted from [61].

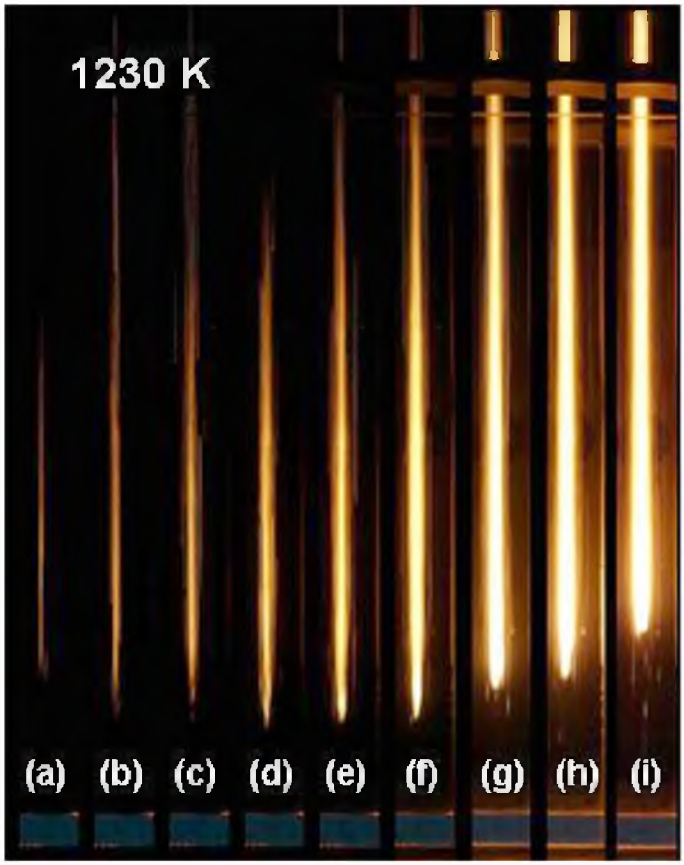

Figure 3.2: Experiment photograph of 75-105 μm Black Thunder coal in 12 vol.% O2 and gas temperature of 1230 K [51].

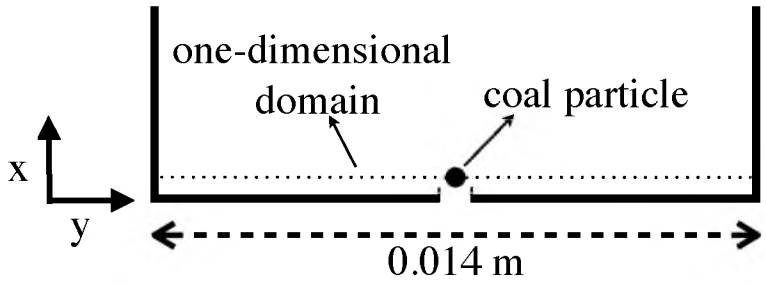

Figure 3.3: A schematic of the simulated system.

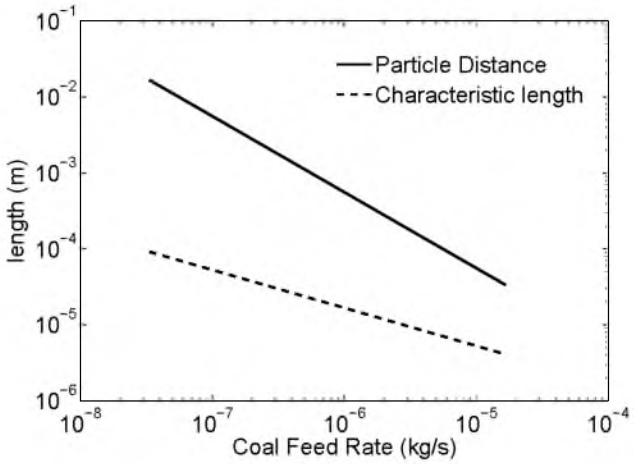

Figure 3.4: Characteristic length and distance between subsequent particles versus flow rate

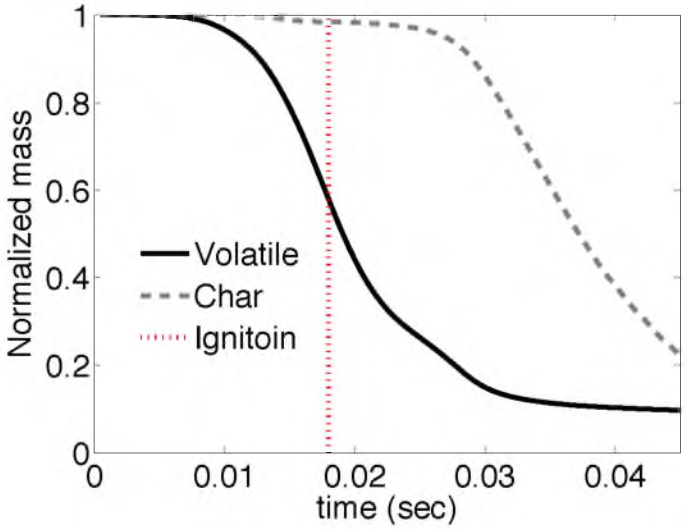

Figure 3.5: Normalized volatile and char content in the coal particle as a function of time for case $B.1$.

Table 3.1: Parameters for simulations considered herein.

Case	Coal type	Devolatilization model	Gas chemistry model	T_{gas} (K)	Particle size (μm)	O_2 (mole frac)	N_2
$A.1$	Pittsburgh	CPD	detailed kinetics	1200-1750	92.4	0.2	0.384
$A.2$	Pittsburgh	Kobayashi-Sarofim	detailed kinetics	1200-1750	92.4	0.2	0.384
$A.3$	Pittsburgh	CPD	flame-sheet	1200-1750	92.4	0.2	0.384
$A.4$	Pittsburgh	Kobayashi-Sarofim	flame-sheet	1200-1750	92.4	0.2	0.384
$A.5$	Black Thunder	CPD	detailed kinetics	1200-1750	92.4	0.2	0.384
$A.6$	Black Thunder	Kobayashi-Sarofim	detailed kinetics	1200-1750	92.4	0.2	0.384
$A.7$	Black Thunder	CPD	flame-sheet	1200-1750	92.4	0.2	0.384
$A.8$	Black Thunder	Kobayashi-Sarofim	flame-sheet	1200-1750	92.4	0.2	0.384
$B.1$	Pittsburgh	CPD	detailed kinetics	1320	45-125	0.12	0.464
$B.2$	Pittsburgh	Kobayashi-Sarofim	detailed kinetics	1320	45-125	0.12	0.464
$B.3$	Pittsburgh	CPD	flame-sheet	1320	45-125	0.12	0.464
$B.4$	Pittsburgh	Kobayashi-Sarofim	flame-sheet	1320	45-125	0.12	0.464

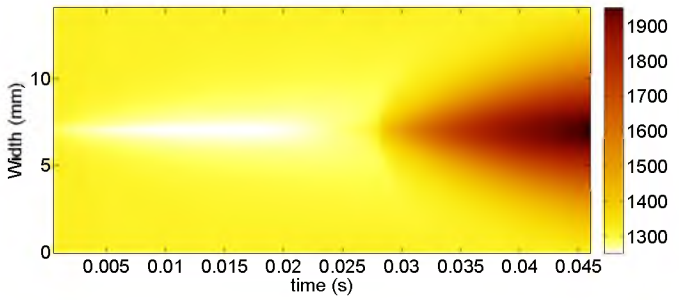

(a) Temperature (K).

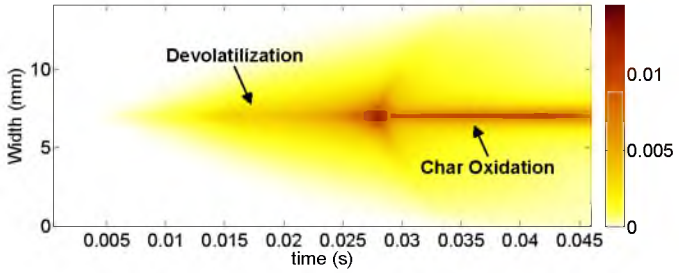

(b) CO mass fraction.

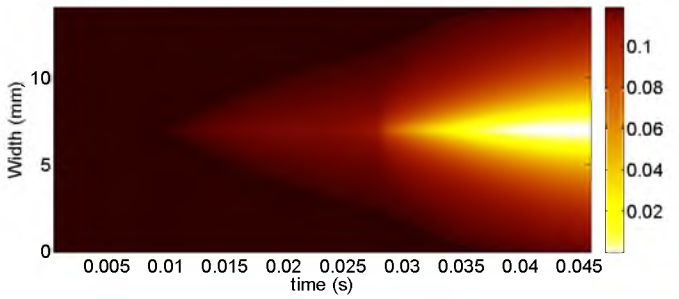

(c) O_2 mass fraction.

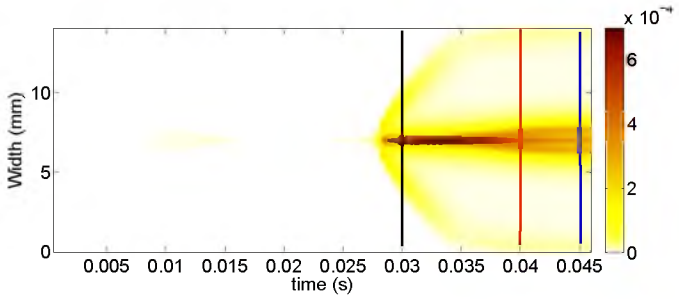

(d) OH mass fraction.

Figure 3.6: Space-time evolution of several quantities associated with case $B.1$ (Table 3.1) with a 92.4-μm particle.

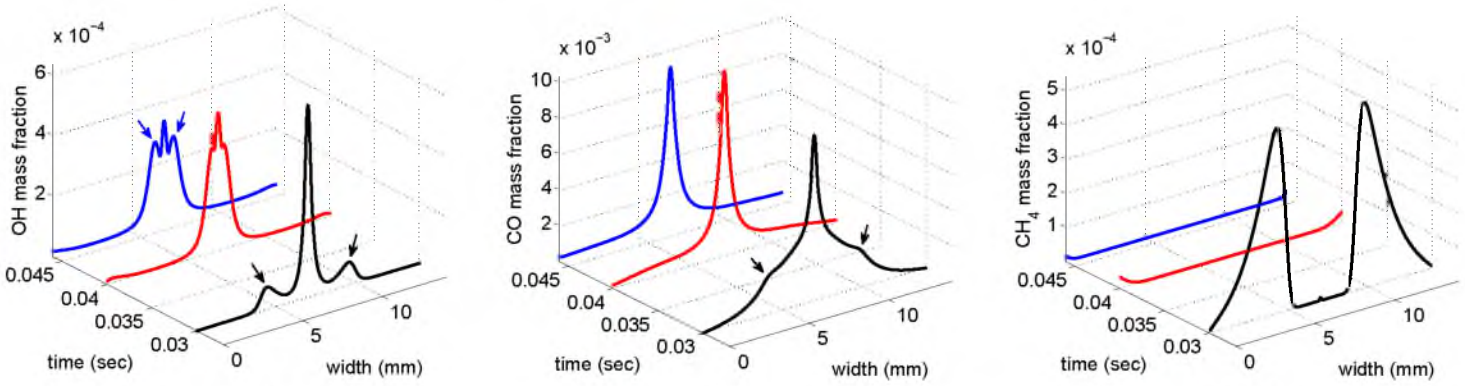

(a) OH (b) CO (c) CH_4

Figure 3.7: Profiles of OH, CO and CH_4 at different times (30, 40 and 45 ms) for case $B.1$ (Table 3.1) with a 92.4-μm particle. Time slices correspond to the vertical lines shown in Figure 3.6d.

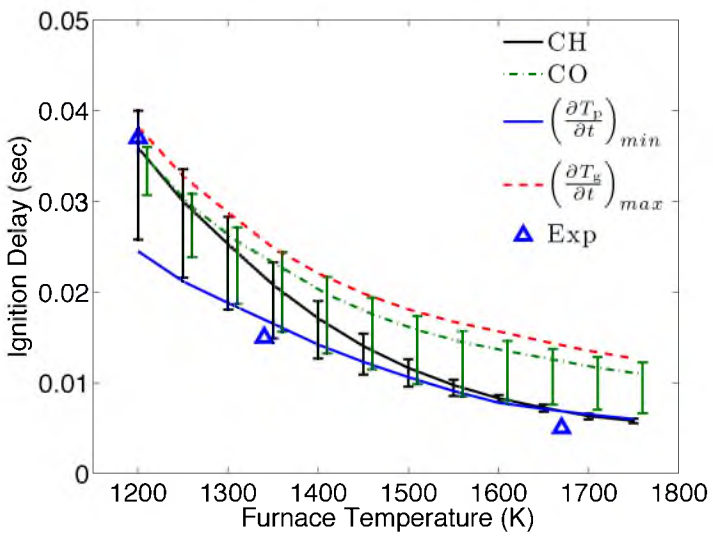

(a) Ignition delay for various criteria. Species criteria are based on the time at which the species mass fraction reaches half of its maximum. Experimental data are extracted from [51] .

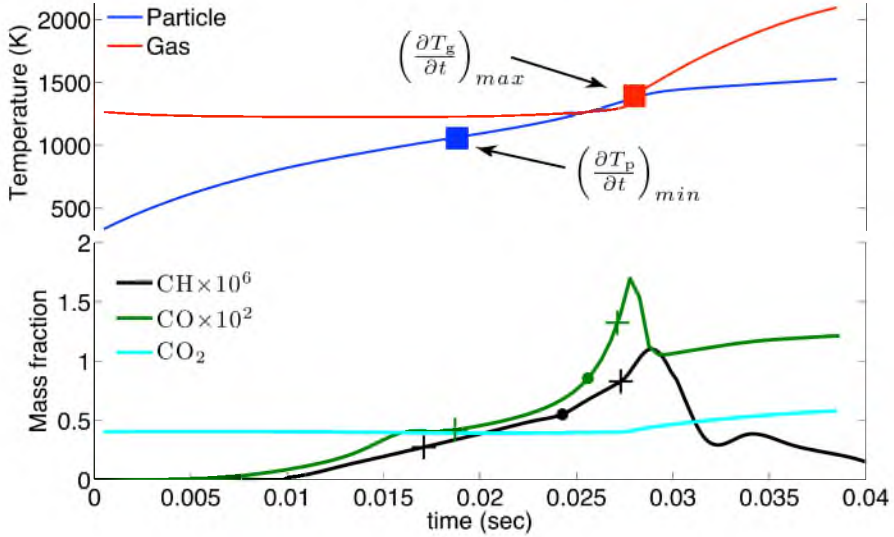

(b) Species (bottom) and particle temperature (top) histories. Crosses indicate 25% and 75% of the maximum species mass fraction and squares show the particle temperature inflection point $\left(\partial T_p/\partial t|_{\min}\right)$ and the maximum gas-phase temperature increase rate $\left(\partial T_g/\partial t|_{\max}\right)$.

Figure 3.8: Ignition delay identified with half of the maximum in species mass fraction profiles. Pittsburgh coal particle with size of 92.4 μm injected into 20 vol% O_2 with N_2 diluent (case *A*.1).

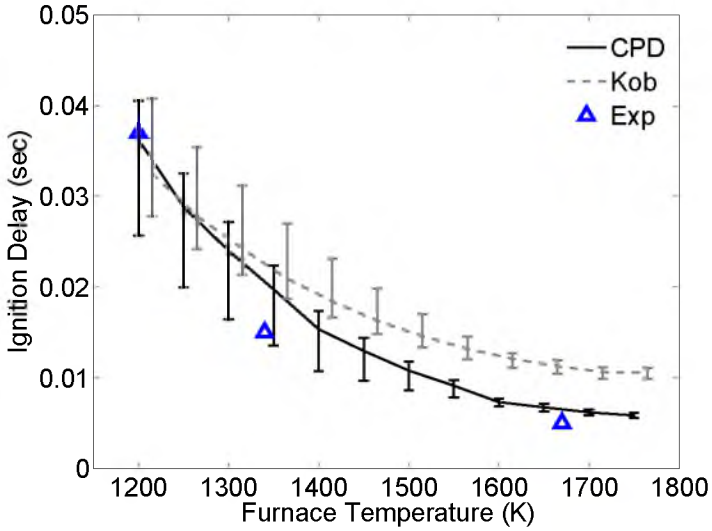

(a) Pittsburgh, cases $A.1$ & $A.2$

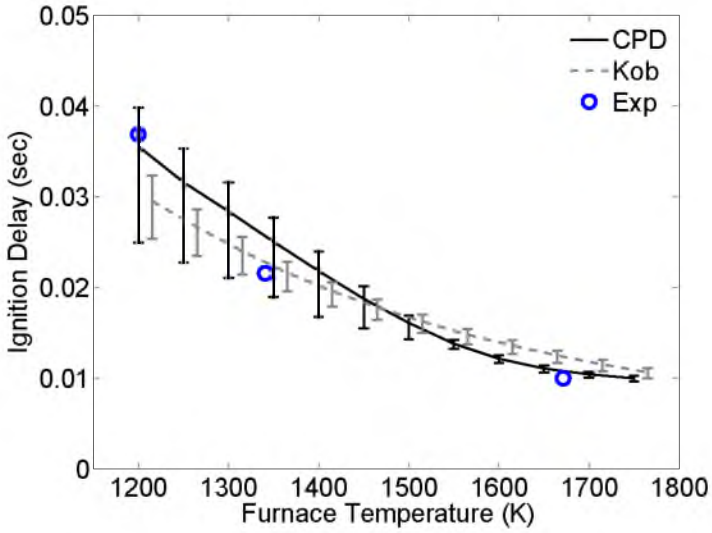

(b) BlackThunder, cases $A.5$ & $A.6$

Figure 3.9: Ignition delay vs initial furnace temperature. CPD, Kob and Exp represent the CPD model, Kobayashi model and experimental data [51], respectively. Detailed kinetics in the gas phase was used where (a) Pittsburgh and (b) BLack Thunder coal types are applied.

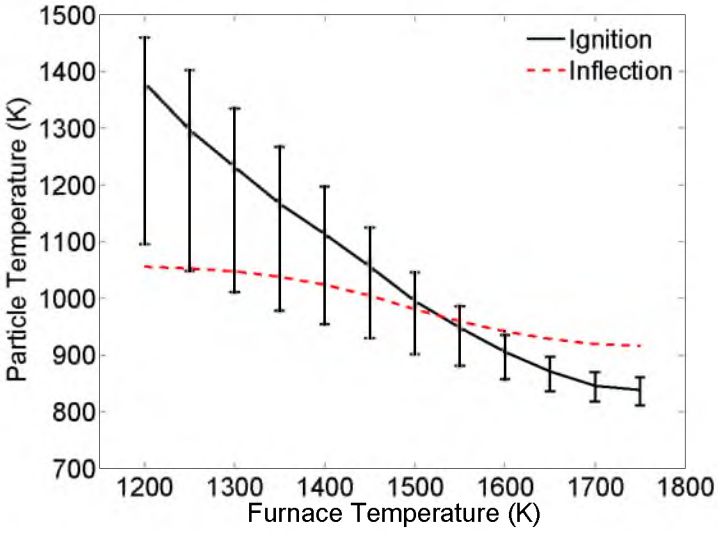

Figure 3.10: Pittsburgh coal particle temperature at ignition and inflection point by utilizing CPD model (case $A.1$). Ignition is characterized by half of CH_x maximum. Vertical bars show 25% and 75% of maximum.

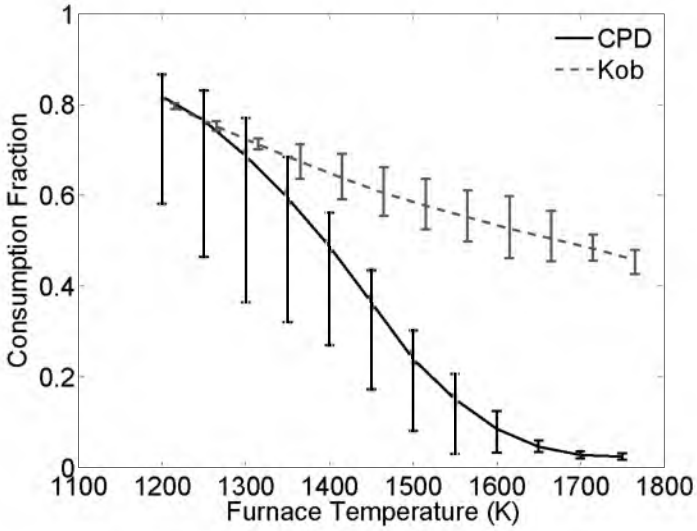

(a) Pittsburgh, cases $A.1$ & $A.2$

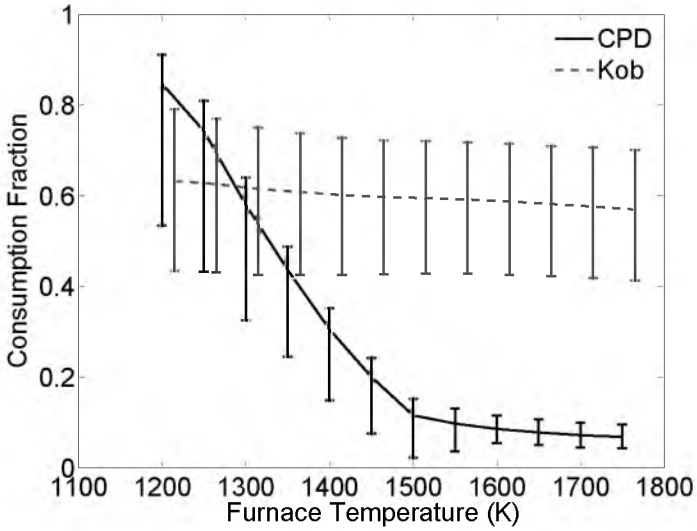

(b) Black Thunder, cases $A.5$ & $A.6$

Figure 3.11: Volatile consumption fraction vs initial furnace temperature. CPD and Kob represent the CPD and Kobayashi-Sarofim models, respectively. Coal types of (a) Pittsburgh and (b) Black Thunder are applied.

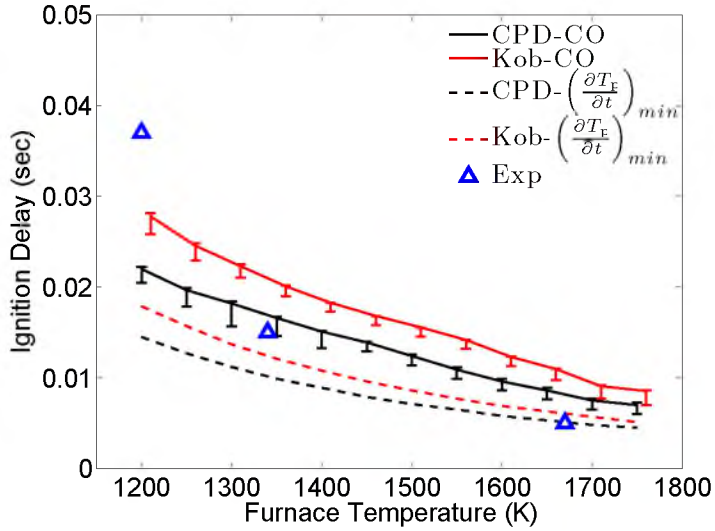

(a) Pittsburgh, cases $A.3$ & $A.4$

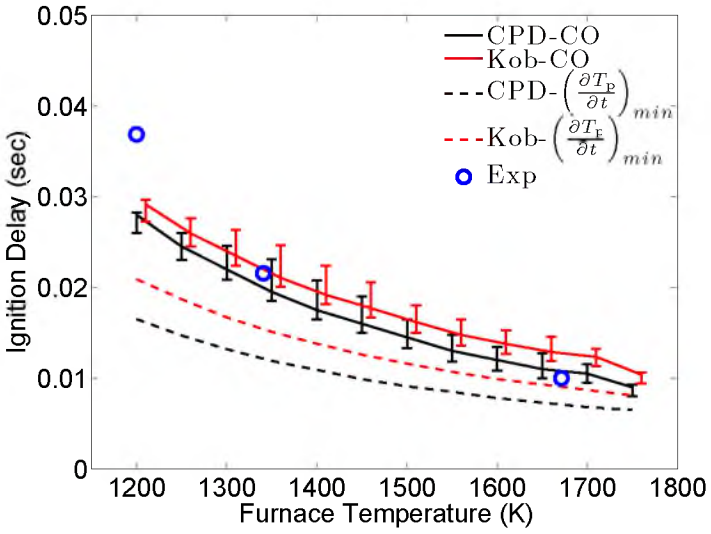

(b) Black Thunder, cases $A.7$ & $A.8$

Figure 3.12: Ignition delay vs initial furnace temperature. CPD, Kob and Exp refer to the CPD model, the Kobayashi-Sarofim model and experimental data [51], respectively. These results employ the flame-sheet calculation in the gas phase where (a) Pittsburgh and (b) Black Thunder coal types are applied.

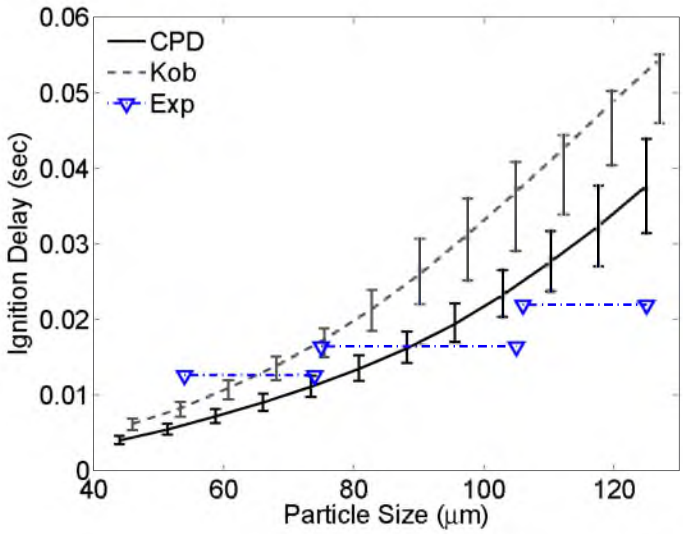

(a) Detailed kinetics, cases $B.1$ & $B.2$

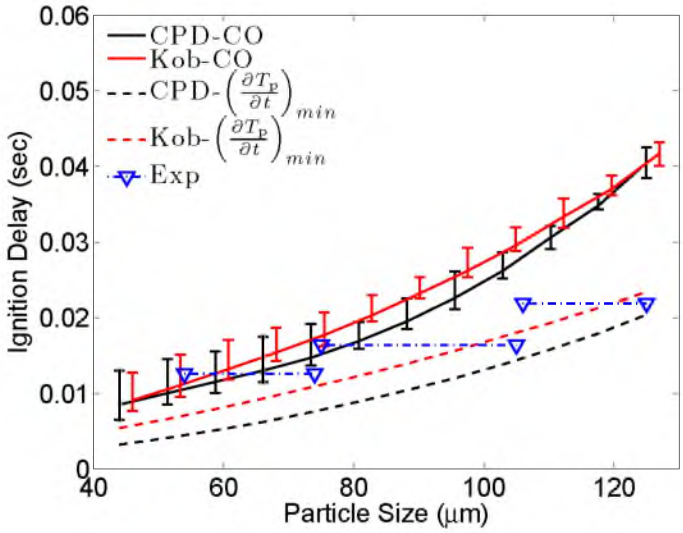

(b) Flame-sheet chemistry, cases $B.3$ & $B.4$

Figure 3.13: Ignition delay vs particle size for a Pittsburgh coal particle injected into 12% vol O_2 in N_2 at 1320 K. The experimental data are shown for the three particle size cuts used experimentally. Gas phase chemistries for (a) and (b) are detailed kinetics and flame-sheet, respectively.

CHAPTER 4

TURBULENT OXY-COAL COMBUSTION

"*The only way to rectify our reasonings is to make them as tangible as those of the Mathematicians, so that we can find our error at a glance, and when there are disputes among persons, we can simply say: Let us calculate [calculemus], without further ado, to see who is right.*"

-Gottfried Wilhelm Leibniz

4.1 Introduction

Among the promising technologies to capture CO_2 for subsequent sequestration in new and existing coal-fired power plants is oxy-coal combustion. In the process of oxy-coal combustion, the oxygen is mixed with recycled flue gas rather than air. Notable difference observed in flame pattern and shape between air-fired and oxy-fuel combustors [42]. There are three main differences between air-fired and oxy-fuel combustion:

1. The oxygen diluent in air-fired is nitrogen (O_2/N_2) but in oxy-coal it is CO_2 (O_2/CO_2)
2. Heat flux (radiative and convective)
3. Combustion product composition and thermal properties

The key aspects in the design of oxy-coal systems are [78]:

- To provide sufficient oxygen into the pulverized coal flow to ensure the complete ignition and stabilization of the flame
- To assure the ratio of recycled flue gas is optimum for radiative and convective heat transfer.

The flue gas recycling ratio has a notable impact on radiant and convective heat transfer. Increasing the recycling ratio will increase the convective heat transfer and also move the peak of radiative heat flux downstream [87].

An important benefit of using oxy-coal technology is the reduction of air pollutants. Oxy-coal combustion can reduce the NO_x emission without decreasing the fuel burnout efficiency [94, 2]. The amount of NO_x formation under different oxygen concatenation is studied by [82]. In oxy-fuel combustion processes, different techniques such as reburning, staging and low-NO_x burning are suggested to control the NO_x emission; the biggest disadvantage of such techniques is reduction in combustion efficiency [65].

Numerous studies on oxy-coal combustion and gasification physics, in particular the ignition delay, flame stability and temperature, flame shape, impacts of oxygen and diluent have been undertaken (see, *e.g.*, [68, 29, 51, 14, 34, 62, 36]). Increasing oxygen concentration accelerates particle ignition regardless of combustion medium [81]. Various experiments have measured the impact of coal type and operating conditions such as composition of coal transport medium on flame stand-off and stability [105, 76].

Models to predict the physics of such a system must address the nonlinearly coupled processes of particle dynamics, gas-phase thermochemistry, heterogeneous reactions between the coal and gas, devolatilization/pyrolysis, vaporization, radiative heat transfer, *etc.* This multiscale (in both space and time) problem poses a significant modeling challenge.

Applying Direct Numerical Simulation (DNS) with detailed gas phase kinetics and coal devolatilization models can help improve understanding of ignition and can provide a basis for evaluating simpler models. However, it remains prohibitively expensive to perform DNS in regimes relevant to practical coal combustion. Reynolds–Averaged Navier–Stokes (RANS) equations are a common solution to reduce the computational cost in most engineering practices. RANS is a turbulence model that solves a time-averaged governing equation. This model has been applied by numerous researchers to simulate the oxy-coal combustion process [46, 8, 106, 10]. In addition, the RANS method is used when radiative heat transfer in oxy-coal combustion is the subject of study [104, 39].

A middle ground between DNS and RANS is the Large Eddy Simulation (LES) model that resolves only large scales and uses submodels to address the small scales. The application of the LES model in oxy-coal combustion simulation is growing due to its reasonable computational cost and has been employed by different researchers [16, 24, 68]. [24] compared the performance of LES and RANS models in air-fires and oxy-fired combustion. They reported that RANS modeling predicts reasonable results for air-fired combustion, however, for the oxy-fired combustion its prediction deviated significantly from the experimental data. In contrast, LES models showed more accurate prediction than RANS, wich can be attributed to turbulent representation in this LES model [24]. Using LES

framework, the direct quadrature method of moments was utilized to address the coal combustion/gasification [67, 75]. Furthermore, the oxy-coal combustor studied in this chapter is simulated by Pedel [67] using the LES model. Regimes of combustion during flame ignition were captured using the LES model. The model also showed the sensitivity of the flame stand-off to the stoichiometric ratio [67]. The results reported by [67] showed that LES model coupled with the direct quadrature method of moments can predict the flame ignition mechanism accurately.

In this work, an Eulerian formulation of the one-dimensional turbulence (ODT) model is used. ODT resolves the full range of length and time scales of the continuum (as in DNS) but in a single spatial dimension, thereby significantly decreasing the computational cost relative to DNS. First proposed by [41], ODT has been successfully applied to a variety of turbulent flows, including particle-laden flows [80] and turbulence-chemistry interaction including extinction and reignition [73, 49]. Most notable among the assumptions in ODT is that the flow field is statistically one-dimensional (implications of this assumption are discussed in [74, 93]). In this work, ODT is used to simulate oxy-coal flames and is evaluated against experimental data [105, 77].

The aim of this chapter is to assess the effects of system parameters as well as model parameters on the prediction of flame stand-off distance in a 40 kW coal combustor [76, 77], and to demonstrate the efficacy of the ODT model in modeling turbulent coal combustion. The impact of the "eddy rate constant" (which affects the mixing rate in ODT), radiative temperature, and primary O_2 concentration on the flame stand-off is explored. Furthermore, the impact of modeling level in particle and gas phases is studied. Two different models for both devolatilization and gas phase chemistry are used. This is the first work of its kind that determines flame stand-off distance using detailed kinetic calculation of the gas phase fully coupled to a high-fidelity model (CPD) for devolatilization of coal particles.

4.2 System Description

The Oxy-Fuel Combsutor (OFC) modeled in this chapter is located at the University of Utah. The OFC is a nominally 100 kW combustor equipped with a recycle system to provide conditions similar to an industrial oxy-coal combustor. As shown in Figure 4.1, OFC consists of three main zone:

1. Burner zone: This zone includes four windows located in its quadrants that provide optical access to the combustion chamber.

2. Radiant zone: This section is made of ceramic plates that keep the "radiative temperature" uniform and at the desired temperature.

3. Convective zone: This zone is located horizontally in the bottom of the furnace.

A schematic of the coaxial burner is illustrated in Figure 4.2. A picture of the OFC is shown in Figure 4.3. Details of the furnace and burner considered here are reported in [77]. The downward-fired burner consists of a primary stream with 15.8 mm ID and 21.3 mm OD and a secondary stream with 35.05 mm ID.

The velocities of the primary and secondary streams are 6.3 and 14.9 m/s, respectively. The composition and temperature of the inlet streams and co-flow are reported in Table 4.1. In this work, the composition of effluent gas is applied for co-flow[1]. Illinois #6 coal particles of size 68.5 μm and density 1450 $^{kg}/_{m^3}$ are fed at a rate of 5.26 $^{kg}/_{hr}$. The coal particles are assumed to have the same temperature and velocity as carrier gas (primary stream). The ultimate and proximate analysis of Illinois #6 coal are reported in [76].

To study the effect of the radiative temperature and mixing rate on the flame stand-off distance, a parametric study was undertaken, as summarized in Table 4.2. For each configuration, approximately 300 realizations are performed to obtain reasonable statistics. Temporal and spatial resolutions are 200 ns and 200 μm, respectively, which yield grid-converged statistics for the flame stand-off distance.

The governing equations and models outlined previously are solved using a fully coupled, compressible algorithm with an explicit time integration scheme and a second-order finite volume spatial discretization. Characteristic boundary conditions [92] are applied on the domain boundaries.

4.3 Computational Resources

Simulations are performed using Center for High Performance Computing (CHPC) resources specified to CRSim group[2]. The computational load was handled by two of the CHPC machines listed below:

- Ember (Linux version 2.6.32-358.18.1.el6.x86_64 - gcc version 4.4.7 20120313)
- Updraft (Linux version 2.6.18-238.el5 - gcc version 4.1.2 20080704)

[1]This assumption is motivated by the recirculation of products upstream to the inlet. Although not ideal, in the absence of experimental measurement of the near-burner entrained gases this was reasonable.

[2]Visit https://software.crsim.utah.edu/trac

4.4 Results and Discussions

The simulation predictions are compared to experimental data where flame stand-off distance is used as a metric.

4.4.1 Flame Stand-off Distance Characterization

Characterizing the ignition point and flame stand-off is a challenge in both experiment and simulation. Pictures of flames were taken in the experiment to characterize the flame stand-off using image processing techniques. A sample picture is given in Figure 4.4.

To find the flame stand-off distance, the first step is to characterize the flame boundaries. Figure 4.5 shows the experimental methodology used to identify the flame boundaries (discussed in [105]) which can be summarized as:

1. sequence of images taken by a CMOS camera were collected (∼6000)
2. pictures are converted to gray scale which makes the pictures an n×m matrix
3. flame edges were defined to be where the intensity gradient is at the maximum. Sobel operator is applied to accomplish this task.
4. The average intensity value at the detected edges was used to define a threshold value. The threshold value is different in every image.
5. The calculated threshold value was applied to the gray scale image to obtain the flame stand-off distance.

These steps were applied to the sequence of approximately 6000 images to obtain a Probability Density Function (PDF) for the flame stand-off distance [77].

The simulations do not allow for a direct comparison with experimental data since a reliable model for light emission in the spectra captured by the CMOS camera would be a significant undertaking. In this work, a simple model based on the local mole fraction of acetylene (C_2H_2) and the gas temperature is used:

$$I_{C_2H_2} = x_{C_2H_2} \times T_g^4. \tag{4.1}$$

Acetylene was chosen since it is a soot precursor [20]. With (4.1) as an approximation for the light emission intensity, a procedure analogous to the experimental one outlined here is used to define the flame stand-off:

- $I_{C_2H_2}$ is determined via (4.1), and the flame edges are defined where the gradient is at the maximum.

- The average $I_{C_2H_2}$ is used to define a threshold value.
- The flame stand-off distance is identified where $I_{C_2H_2}$ first crosses the threshold.

For each simulation listed in Table 4.2, the above procedure is applied to obtain a PDF of the flame stand-off distance for comparison with the experimental data.

Figure 4.6 shows the average of normalized volatile ($\langle m_v \rangle$) and char mass ($\langle m_c \rangle$) of coal particles for case A.3, as well as the relative contribution of char oxidation to the overall char consumption rate (the balance being char gasification)[3]. Figure 4.6 indicates that the onset of devolatilization occurs around $\ell \approx 0.2$ m and that char consumption, dominated by gasification reactions, is active beginning at $\ell \approx 0.3$ m. The vertical bars indicate the maximum and minimum values observed among the coal particles at a given location (across all ODT realizations), and are due to particle dispersion, which subjects the particles to different gas environments.

The ensemble-averaged spatial profiles for a few gas-phase properties for case A.3 are shown in Figure 4.7. The gas phase temperature (Figure 4.7a) at the centerline resists heating due to the thermal inertia of the coal particles. A volatile cloud starts to form at the centerline at $\ell \approx 0.25$ m, displacing and consuming O_2 as the coal temperature increases and devolatilization nears completion around $\ell \approx 0.45$ m. The homogenous oxidation of the volatiles at $\ell \approx 0.25 - 0.35$ m produces OH as an intermediate species as shown in Figure 4.7d. The notable production of OH after $\ell \approx 0.5$ m indicates the homogenous reaction (oxidation) of the accumulated fuel at the center of the furnace.

By $\ell \approx 0.4$ m, homogenous reactions have consumed most of the oxygen in the devolatilization region (as evidenced by Figure 4.7b) and the temperatures of the gas and particles are high enough that the char reactions become important. Figure 4.6 shows the fraction of the char consumption that is due to char oxidation (with the balance due to gasification), and indicates that gasification reactions (reaction of char with H_2O and CO) play a very substantial role in the char consumption. Indeed, Figures. 4.7c and 4.7e indicate that the CO_2 is largely consumed by char oxidation, being replaced with a substantial amount of CO. At $\ell \approx 0.45 - 0.6$ m the gasification reactions are accountable for 60-80% of char consumption. In addition, due to the lack of oxygen around the coal particles after $\ell \approx 0.45$ m the the char oxidation reaction favors CO (rather than CO_2) production.

A final observation on Figure 4.6 is that the overlap of char oxidation/gasification with devolatilization suggests that these processes should be allowed to occur concurrently

[3]Space-time mapping was applied using the mean axial velocity (which evolves in time) to determine an approximate downstream distance for the ODT line. See [93] for details.

rather than assumed to occur sequentially, as has been assumed in some proposed modeling approaches [97, 34, 36].

Since this work is focused on characterizing flame stand-off distance, the simulation predictions at the longer distances, where subsequent mix-out of the rich zone and burnout occur, are not discussed herein.

The trajectories of coal particles are predicted using equations (2.14) and (2.15). In Figure 4.8 an ensemble average over particle number density for case A.3 is illustrated. Considerable homogenous/heterogeneous oxidations at $\ell \approx 0.35$ m increases the spanwise gas phase velocity (v). Therefore, the spanwise particle velocity increases (see (2.15)) and disperses the coal particles. In Figure 4.8, particle numbers density after $\ell \approx 0.35$ m is decreased at the center of jet where the coal particles starts to disperse in spanwise (y) direction.

4.4.2 Impact of Mixing

As discussed in §2.4, the impact of C as an ODT model parameter is to directly influence the eddy frequency (turbulence intensity). This section explores the effect of this parameter on the predicted flame stand-off[4]. Figure 4.9 shows the ensemble averaged streamwise (axial) velocity profiles, $\langle u \rangle$, for different C values at two downstream locations, and provides an indication of the effect of C on entrainment.

The coal particle temperature, averaged across all particles and all ODT realization at a given downstream length, is illustrated in Figure 4.10 for three values of C. The vertical bars indicate the minimum and maximum observed particle temperatures for all ODT realizations. An increase in C leads to greater particle dispersion which, for $\ell < 0.35$, tends to move some particles into hotter regions (see Figure 4.7). This, in turn, leads to earlier ignition and shorter flame standoff distance, as can also be inferred from Figure 4.10.

Figure 4.11 shows the the experimentally observed flame stand-off as well as the results for different eddy rate constants (C). The minimum characterized flame stand-off distance (*i.e.*, the position of the left-most tail of the PDF) is relatively insensitive to the mixing rate, suggesting that the lower-limit for the flame standoff is kinetically controlled. The width of PDFs in Figure. 4.11 shrinks as C value increases, consistent with the suggestion of a kinetically-limited lower limit for flame standoff around $\ell = 0.22$. Physically, larger mixing rates result in higher particle dispersion as well as introduction of hot product gases

[4]The effect of this parameter on turbulent reacting jets was studied by [74], where $C = 10$ was suggested as a reasonable value.

into the devolatilization region. As discussed previously (see Figure 4.10), this increases the mean particle temperature resulting in higher devolatilization rates and resulting in a narrowing of the flame stand-off PDF.

To further establish the relative importance of mixing vs reaction on the flame stand-off prediction, the oxygen mole fraction of the jet primary stream was increased from 0 (case A.3) to 0.101 (case C.1) while the overall oxygen flow in the jet (primary and secondary streams) is kept constant. Other properties such as streams velocity and temperature are preserved (see Table 4.1 for details). Figure 4.12 illustrates the effect of the primary stream composition on flame stand-off, where the experiment data (dashed line) are for $x^p_{O_2} = 0$. The minimum distance of flame stand-off PDF that represents the kinetic limited ignition is not affected by a change in oxygen concentration in the primary stream; further suggesting that the minimum flame stand-off is kinetically limited. There is a slight effect of partial premixing ($x^p_{O_2}$=0.101) on the larger flame stand-off distance, indicating that the effects of mixing (for $x^p_{O_2}$=0) become more important in determining flame standoff.

4.4.3 Influence of Radiative Temperature

In the particle energy equation, (2.4), an effective radiative temperature is considered as the radiation source. To characterize the impact of this effective radiative temperature on flame stand-off distance, a range of effective radiative temperatures from 1280 K to 1800 K was considered. Figure 4.13 shows the influence of radiative temperature on flame stand-off distance. As expected, higher effective radiative temperatures result in a smaller stand-off distance. The significant influence of radiative temperature on flame stand-off distance was also reported by [68], in which LES of the oxy-coal combustor was performed.

As explained perviously, the shorter distances of PDFs are the flames identified in kinetic limited regimes. In Figure 4.13, the shortest distances of PDFs are moving notably with changes in radiative temperature that emphasize the dominancy of kinetic limited regimes in these distances, whereas mixing rate did not have considerable influence on them. Additionally, the PDF width decreases with increasing radiative temperature; this can be explained by the rate of volatile release.

Figure 4.14 illustrates the averages of normalized volatile mass in the coal particles at the downstream distance where ignition occurs ($\langle m_v | \text{Flame} \rangle$). The vertical bars indicate the range of normalized volatile mass observed at the corresponding flame stand-off distance. Of particular significance, Figure 4.14 suggests that there is a minimum devolatilization required to achieve ignition and that this amount is nearly constant over a range of radiative temperatures, despite the large difference in devolatilization rates at the various radiative

temperatures. The larger devolatilization rates at higher wall temperatures simply narrow the flame stand-off PDF, providing a more uniform ignition.

4.4.4 Models Impact

The level of modeling in gas and coal phase significantly impacts the prediction of oxy-coal combustion physics. In Figure 4.15, flame stand-off predictions for the CPD model, Kobayashi-Sarofim model (Kob) utilizing detail kinetic (DK) and flame-sheet (FS) calculation are illustrated.

As Figure 4.15 presents, utilizing detailed kinetic calculation in the gas phase and CPD model in the particle phase provides a satisfactory prediction of flame stand-off distance where it almost agrees with experimental data. The Kobayashi-Sarofim model predicts longer flame stand-off distance than the CPD model, which can be attributed to the yield and composition of volatile produced by the Kobayashi-Sarofim model.

The dotted lines in Figure 4.15 represent the flame stand-off distances predicted by using the flame-sheet model calculation for CPD and Kobayashi-Sarofim model. In the flame-sheet calculation (discussed in 2.1.2), the homogenous reactions of fuel and oxidizer are assumed to be infinitely fast, therefore, the mean value of flame stand-off distance is decreased notably compared to detail kinetic calculation. Furthermore, the shape of the flame stand-off PDF in the flame-sheet calculation is narrower than in the detailed kinetic model. This is also consistent with the "mixed-is-burnt" assumption of this model. This phenomena is expected to be observed more substantially where the process is reaction limited rather than diffusion-mixing limited.

As explained before, there is a minimum of volatile yield required to onset the ignition. Hence, it is expected that the minimum flame stand-off distance for the given devolatilization model be constant using detail kinetic or flame-sheet calculation, as illustrated in Figure 4.15. Furthermore, the discrepancy in prediction of flame stand-off distance decreases when employing flame-sheet rather than detail kinetic calculation where the reactivity of species in the flame-sheet calculation is not accounted and assumed to be equal.

Figure 4.16 shows the contour plots of gas temperature and some species mass fraction in the gas phase using flame-sheet calculation. The gas phase temperature rapidly increases at $\ell \approx 0.27$ m as shown in Figure 4.16.a due to homogenous reaction of the volatiles. C_2H_2 can be an appropriate representative of volatile in the gas phase (Figure 4.16.b). In addition, CO at early stages, before activation of the char oxidation/gasification process can represent the released volatile. At $\ell \approx 0.27$ m there is a considerable release of volatile into the gas as shown by C_2H_2 and CO in Figure 4.16.b and Figure 4.16.c, respectively. The rapid decrease

in oxygen mass fraction also evidences the onset of homogenous reaction at $\ell \approx 0.27$ m. There is a significant increase in CO mass fraction at $\ell \approx 0.35$ m, mostly produced by char oxidation. The char oxidation process fiercely consumes all the accessible oxygen at the edge of the flame and releases considerable heat as shown in Figure 4.16.a. Due to lack of oxygen at the center of the flame, the char oxidation process is in favor of CO production.

In the flame-sheet calculation, fuel burns as soon as it is mixed with the oxidizer. Therefore, there are two main flame limitations:

1. Diffusion/mixing limit: The flame-sheet model uses the "burnt as mixed" idea. Mixing will provide fuel with oxidizer for homogenous reactions.

2. Fuel limit: The homogeneous oxidation requires fuel in the gas phase. This fuel can be provided by devolatilization and char oxidation (*e.g.*, CO).

The minimum flame stand-off distance represents the fuel limitation in the flame-sheet model enforced by the devolatilization model. In other words, a minimum of fuel is required in the gas phase to form a flame. The fuel limit is controlled by coal particle submodels as well as particle heating rate. The impact of gas chemistry models on the minimum flame stand-off distance is negligible. However, parameters affecting particle behavior such as radiative-temperature and the devolatilization model can move the minimum flame stand-off distance. Radiation heat transfer dominated by the refractory wall is one of the main factors influencing the particle heating rate that can change the flame stand-off distance as illustrated in Figure 4.17.

In oder to show the insensitivity of the minimum flame stand-off distance to the gas chemistry model, flame stand-off distance using detailed kinetic and flame-sheet model is predicted at different radiative temperatures. Figure 4.17 shows the flame stand-off predicted using Detailed Kinetic (DK) and Flame-Sheet (FS) calculation in the gas phase for a radiative temperature of 1280 (4.17.a) and 1800 K (4.17.b). A change in radiative temperature influences the particle temperature directly thereby affecting the volatile release. The flame stand-off PDF predicted by the flame-sheet model becomes narrower as the radiative temperature increases. As explained before (4.14), at higher radiative temperature, a higher rate of volatile release is expected.

The infinity-fast chemistry calculation in the gas phase not only affects the gas phase but also has a significant impact on particle behavior. Figure 4.18 shows the normalized volatile and char mass as the particle evolves through the furnace. The solid and dotted lines represent utilization of Detailed Kinetic (DK) and Flame-Sheet (FS) calculation in the

gas phase, respectively. In the flame-sheet model, the homogenous oxidation of volatile is infinitely-fast, however, in the detail kinetic model, the oxidation rate depends on the species reactivity at given gas temperature. After $\ell \approx 0.2$ m, particles gain enough temperature to release volatile, which is marked as the minimum flame stand-off distance for both gas chemistry models in Figure 4.15. Due to faster homogenous oxidation of volatile in the flame-sheet, the released energy (of oxidation) increases the particles faster than in detail kinetic calculation, thereby, accelerating the devolatilization process and volatile release. The char oxidation process is activated at $\ell \approx 0.35$ m and $\ell \approx 0.37$ m using flame-sheet and detailed kinetic calculation, respectively. However, at $\ell \approx 0.5$ m the amount of oxidized char using detail kinetic exceeds the flame-sheet model, which can be attributed to the lack of oxidizer (oxygen) at particle position. In the flame-sheet calculation, homogenous oxidation of volatile (and also CO produced by char oxidation) is infinity-fast so that the char oxidation process cannot be provided with the same amount of oxygen as in detail kinetic calculation. According to what has been explained, using the flame-sheet (infinity-fast) model in the gas phase calculation has significant impact on both homogenous and heterogenous reactions and changes the fate of coal particle in the combustion/gasification process.

The devolatilization model has a notable impact on the flame stand-off shape and minimum as illustrated in Figure 4.15. This can be explained by the discrepancy in the devolatilization rate and the released species in each model. The impact of species reactivity discrepancy is damped in the flame-sheet model, as in this model the reactivity of species is assumed to be equal. Figure 4.19a shows the normalized volatile mass using the Kobayashi-Sarofim and CPD model. An implication of (2.49) is that the activation energies used in the CPD model are initially low and then increase with the releases of volatile. However, in the Kobayashi-Sarofim model the activation energy is assumed to be constant. Therefore, it can be expected that initial volatile yield of the CPD model will be higher than that of the Kobayashi-Sarofim model. Due to this fact, the flame stand-off distance predicted by the CPD model is shorter than that of the Kobayashi-Sarofim model.

Figure 4.19b shows the average particles temperature at given furnace lengths. As explained before, the initial yield of the CPD model is more than that of the Kobayashi-Sarofim model; therefore, a higher energy release due to volatile reaction is expected. Hence, the average particle temperature in the CPD model is higher than in the Kobayashi-Sarofim model at $\ell \lessapprox 0.35$ m. However, after $\ell \approx 0.35$ m, the volatile yield of the Kobayashi-Sarofim model exceeds that of the CPD model as shown in Figure 4.19a. The homogenous reaction

of the released volatile heats up the particles rapidly where at $\ell \approx 0.40$ m the average particle temperature in the Kobayashi-Sarofim model surpasses that in the CPD model.

To further elaborate on the impact of the devolatilization model, the contour plots of gas properties using the Kobayashi-Sarofim model (case E.1) are illustrated in Figure 4.20. In Figure 4.20a there is a rapid increase in gas temperature at $\ell \approx 0.38$ m that is almost matched with the mode of flame stand-off distance PDF, as illustrated in Figure 4.15. At this length there is also notable production of CO as shown in Figure 4.20b. The oxygen consumed considerably at the center of the furnace after $\ell \approx 0.42$ m can be evidence of the char oxidation process. OH as an intermediate species in homogenous oxidation is illustrated in Figure 4.15d. The notable formation of OH after $\ell \approx 0.4$ m also shows the considerable homogenous oxidation and indicates the fuel lean limit of the flame. After $\ell \approx 0.45$, due to lack of oxygen at the center of furnace, the OH has almost vanished. However, oxygen diffuses into the center of the furnace where it mixes with hot gas and the OH being produced during the homogenous oxidation.

4.5 Conclusions

Simulations of oxy-coal flames have been performed using the ODT model. Because the ODT model must only resolve the physics in one spatial dimension, it allows incorporation of detailed thermochemistry models that would be unaffordable in DNS. The fully coupled governing equations in the particle and gas phases including mass, momentum and energy are solved with detailed gas-phase kinetics and a high-fidelity devolatilization model (CPD). Comparison to experimental data indicate that the model captures the flame standoff distance, a key marker of ignition, quite well. Results indicate that char gasification plays an important role during the later phases of the devolatilization process after homogeneous ignition occurs.

The impact of mixing rate on the flame stand-off prediction and physics of the system was also considered. For the cases studied in this chapter, an increase in mixing rate decreases the likelihood of ignition at longer distances; however, it does not affect short distances, suggesting a kinetically limited lower bound to flame standoff. A study on the impact of radiative temperature on simulation prediction is performed. Results show that radiative temperature significantly influences flame stand-off distance, modifying both mean and PDF shape of flame stand-off. In addition, the simulations performed here consider a uniform particle size, and these conclusions must bear that in mind.

The level of modeling in gas and particle phases has significant effect on the fate of both phases. In the gas phase the prediction of detailed kinetic and flame-sheet models are

compared. The flame stand-off PDF predicted by the flame-sheet model is narrower than that in the detailed kinetic, however they share the same minimum flame stand-off distance. As explained in the "radiative-temperature" (§4.4.3) study, the minimum flame stand-off represents the minimum of volatile required to onset the flame through homogenous reaction.

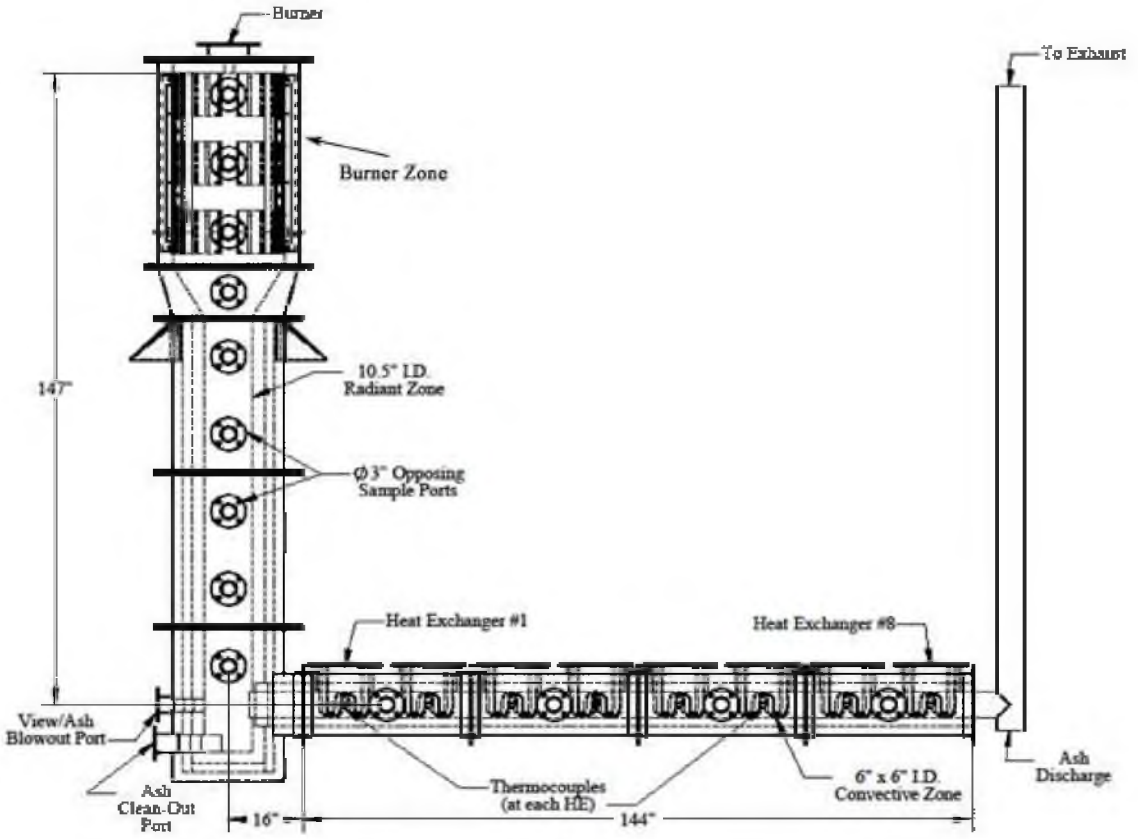

Figure 4.1: Schematic of OFC. Reproduced with permission from [77].

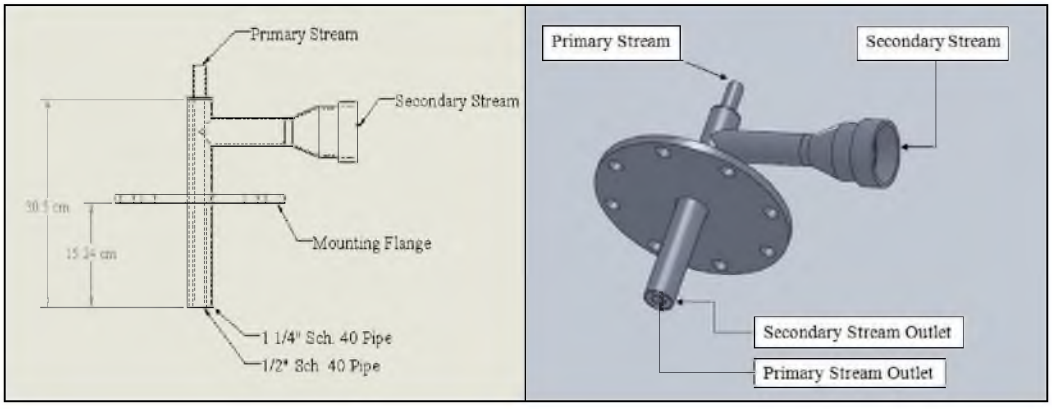

Figure 4.2: Burner schematic. Adapted from [77].

Figure 4.3: Picture of the OFC. Reproduced with permission from [76].

Table 4.1: Composition and temperature of burner streams and co-flow gas.

	T	O_2	CO_2	H_2O
	(K)	volume fraction		
Primary	305	0.0-0.101	1.0-0.899	0.0
Secondary	489	0.488-0.467	0.512-0.533	0.0
Co-flow	1283	0.048	0.815	0.137

Table 4.2: Parameters for simulations considered herein.

Case no	$x^{\mathrm{P}}_{\mathrm{O}_2}$	$x^{\mathrm{S}}_{\mathrm{O}_2}$	C	T_{wall} (K)	Gas Chemistry Model	Devolatilization Model
A.1	0.0	0.488	10	1280	Detailed Kinetic	CPD
A.2	0.0	0.488	10	1450	Detailed Kinetic	CPD
A.3	0.0	0.488	10	1600	Detailed Kinetic	CPD
A.4	0.0	0.488	10	1800	Detailed Kinetic	CPD
B.1	0.0	0.488	2	1600	Detailed Kinetic	CPD
B.2	0.0	0.488	20	1600	Detailed Kinetic	CPD
C.1	0.101	0.467	10	1600	Detailed Kinetic	CPD
E.1	0.0	0.488	10	1600	Detailed Kinetic	Kobayashi-Sarofim
E.2	0.0	0.488	10	1600	Flame-Sheet	CPD
E.3	0.0	0.488	10	1600	Flame-Sheet	Kobayashi-Sarofim
E.4	0.0	0.488	10	1280	Flame-Sheet	CPD
E.5	0.0	0.488	10	1800	Flame-Sheet	CPD

Figure 4.4: A sample picture taken during the experiment. Reproduced with permission of [76].

Figure 4.5: Flame characterization methodology used in the experiment. Reproduced with permission of [76].

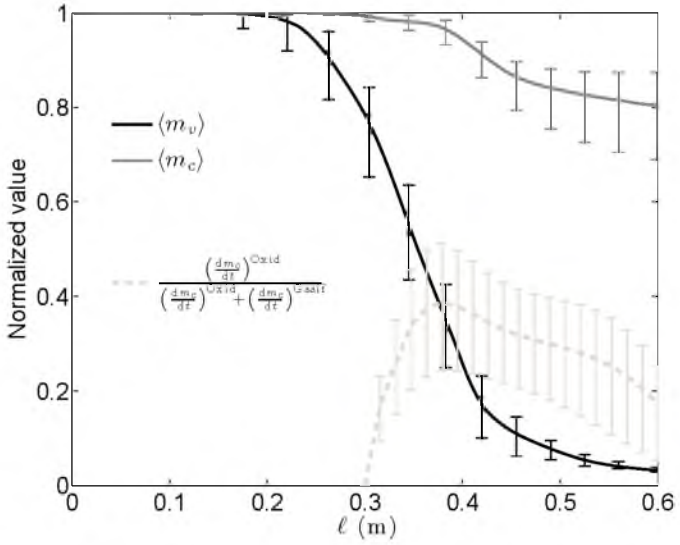

Figure 4.6: Average of normalized volatile and char mass for case A.3. .

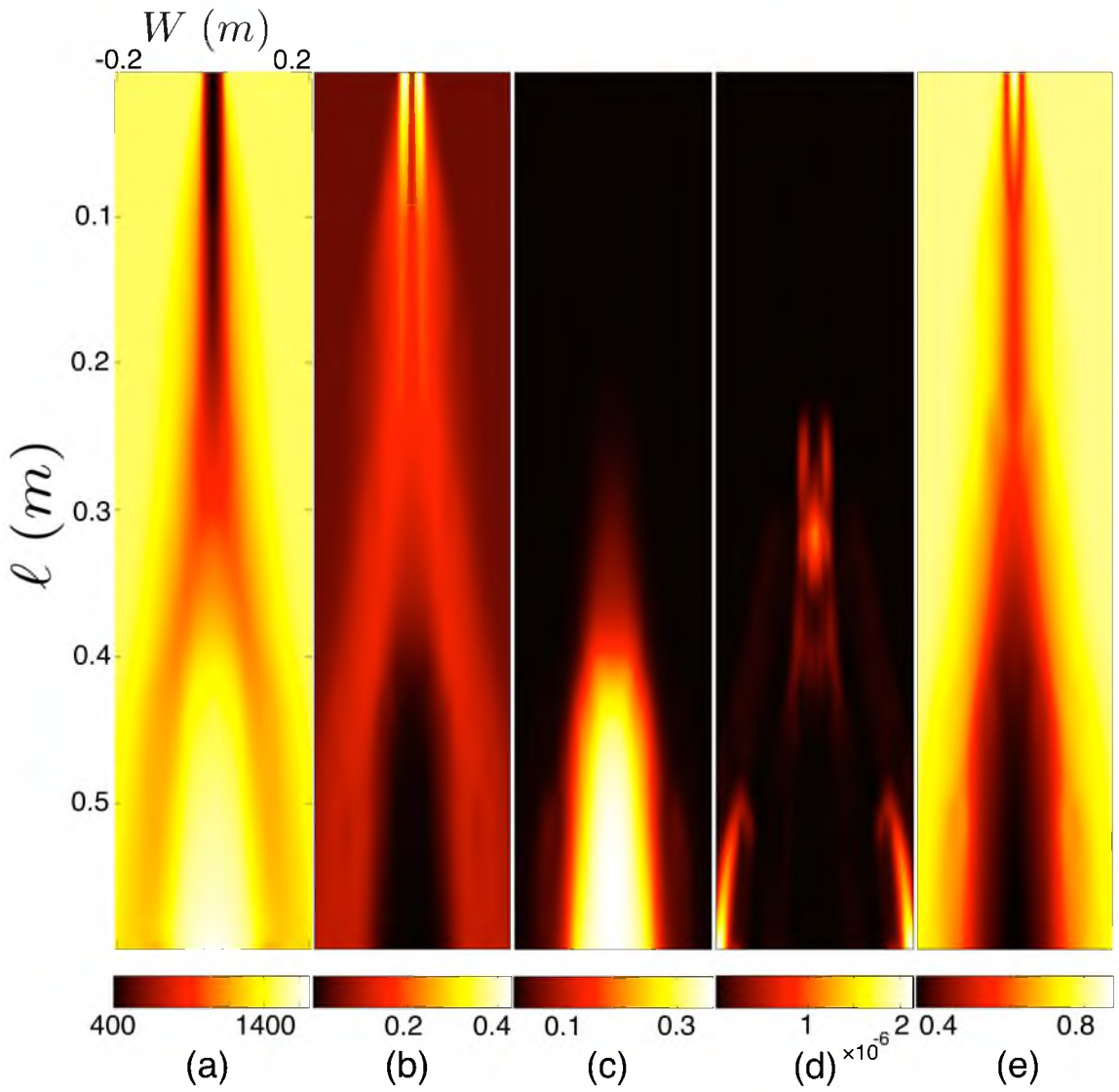

Figure 4.7: Species mole fraction and gas temperature contours for case A.3. a) Gas temperature (K). b) O_2, c) CO, d) OH, e) CO_2 mole fraction.

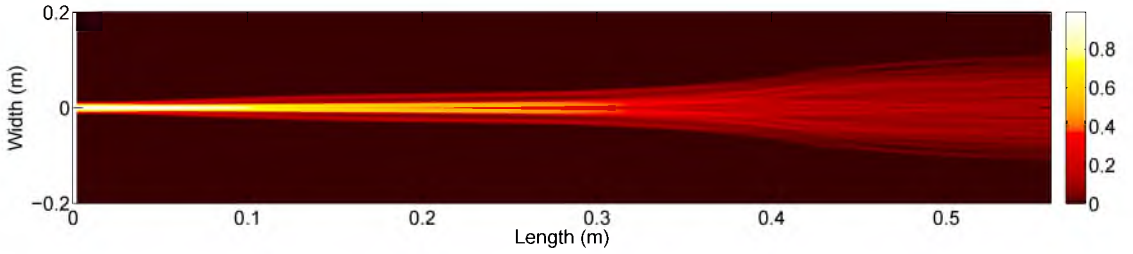

Figure 4.8: Particle number density for case A.3

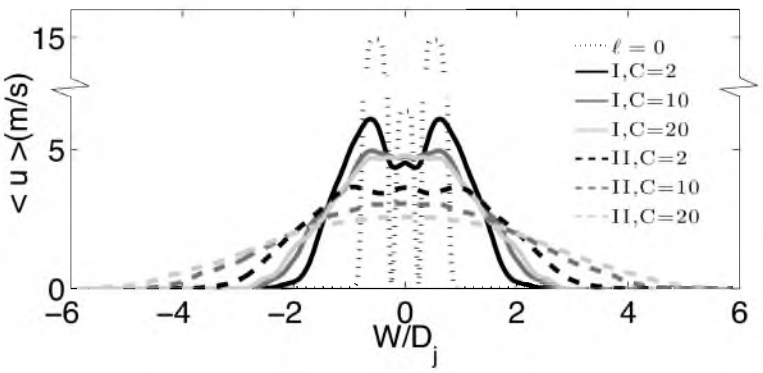

Figure 4.9: Velocity profiles for case B.1 (C=2), A.3 (C=10) and B.2 (C=20) (see Table 4.2). I and II represent $\ell/\mathrm{D_j} = 2.5$ and $\ell/\mathrm{D_j} = 8.5$, respectively, where $\mathrm{D_j}$ is the primary jet inner-diameter. The initial velocity profile is also shown for reference.

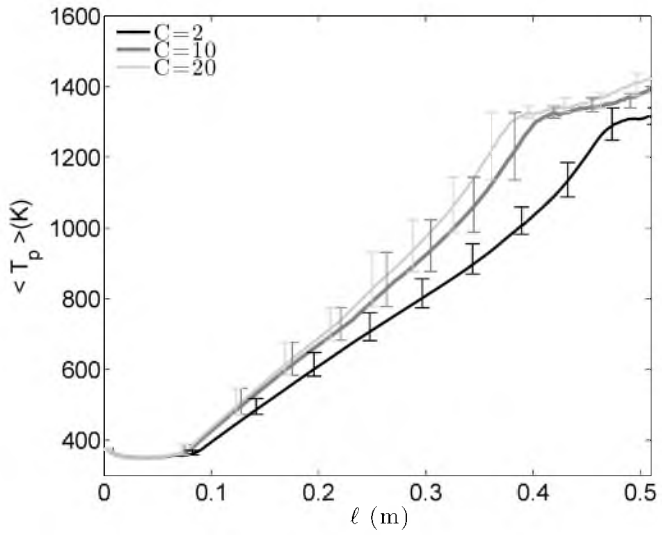

Figure 4.10: Averaged particles temperature for cases B.1 (C=2), A.3 (C=10) and B.2 (C=20) (see Table 4.2).

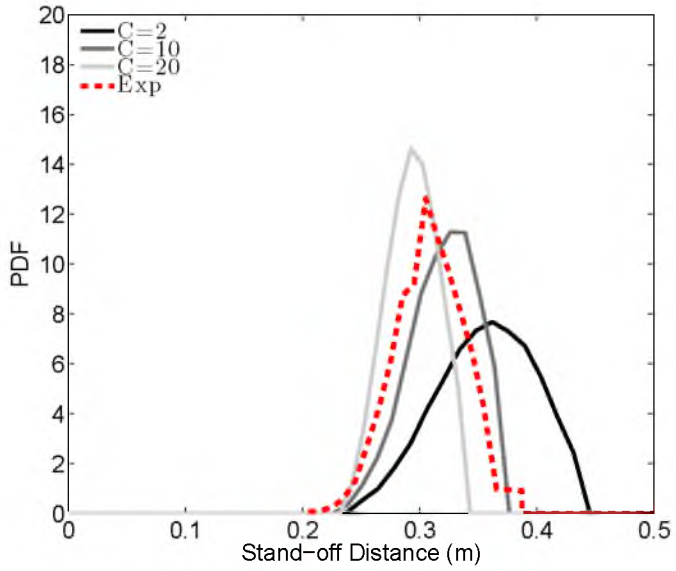

Figure 4.11: Mixing effect on flame stand-off (cases B.1, A.3 and B.2).

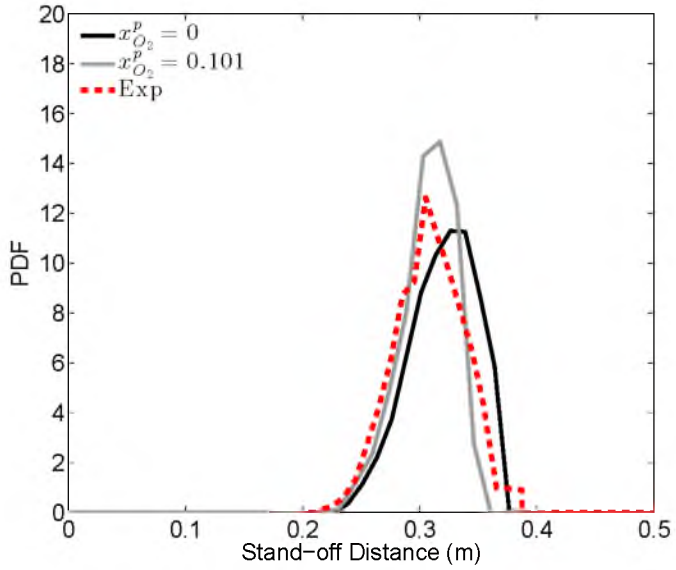

Figure 4.12: Effect of primary oxygen concentration on flame stand-off distance (cases A.3 and C.1) .

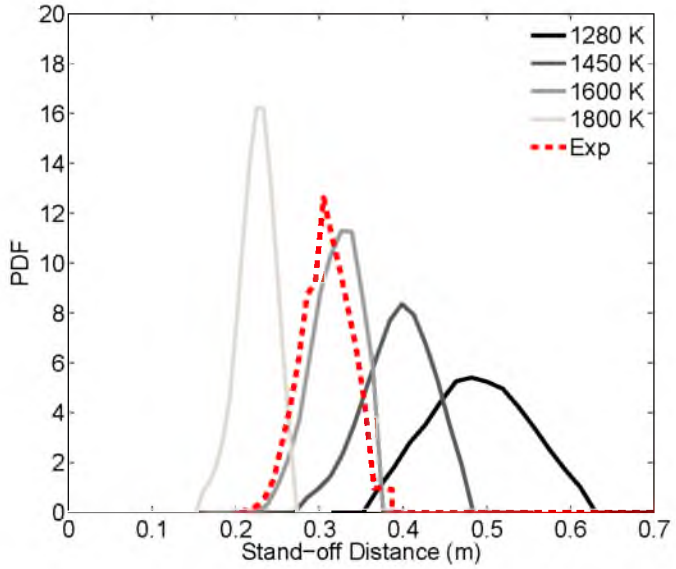

Figure 4.13: Effect of radiative temperature on flame stand-off (cases A.2, A.2, A.3 and A.4).

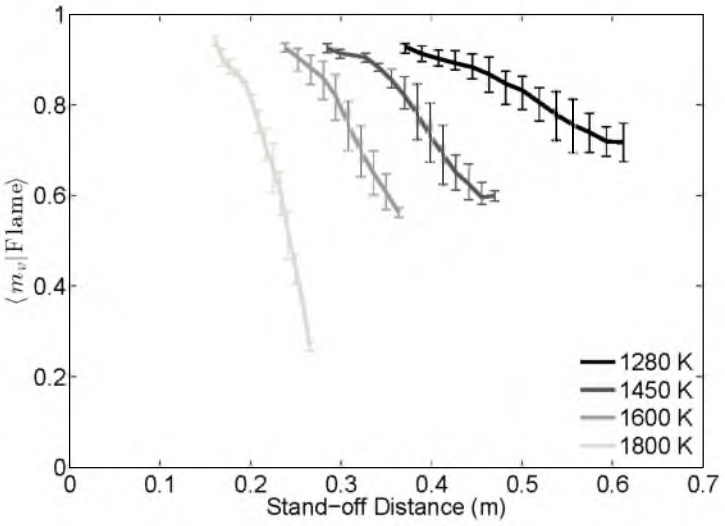

Figure 4.14: Residual volatile fractions in coal particles at the identified flame stand-off distance.

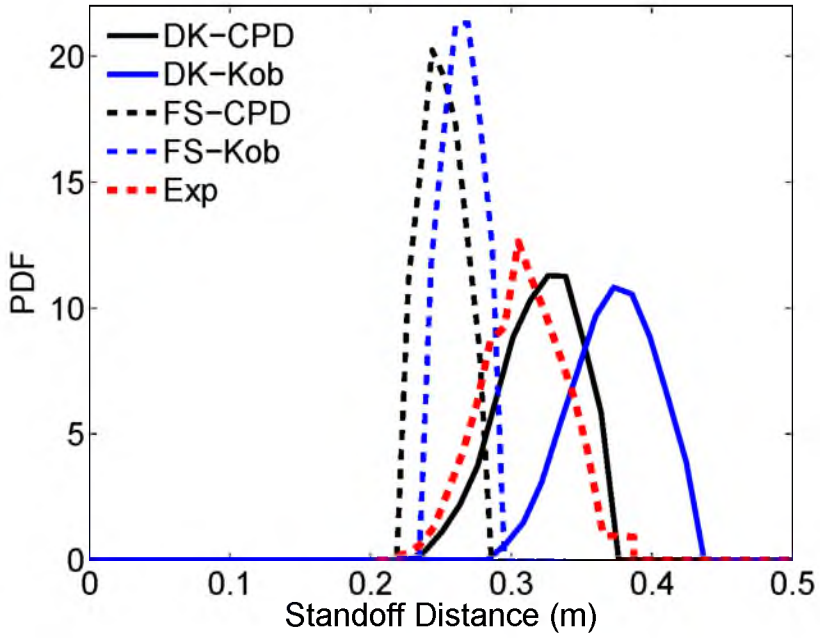

Figure 4.15: Flame stand-off PDFs obtained with both gas phase combustion models and both devolatilization models (cases A.3, E.1, E.2 and E.3).

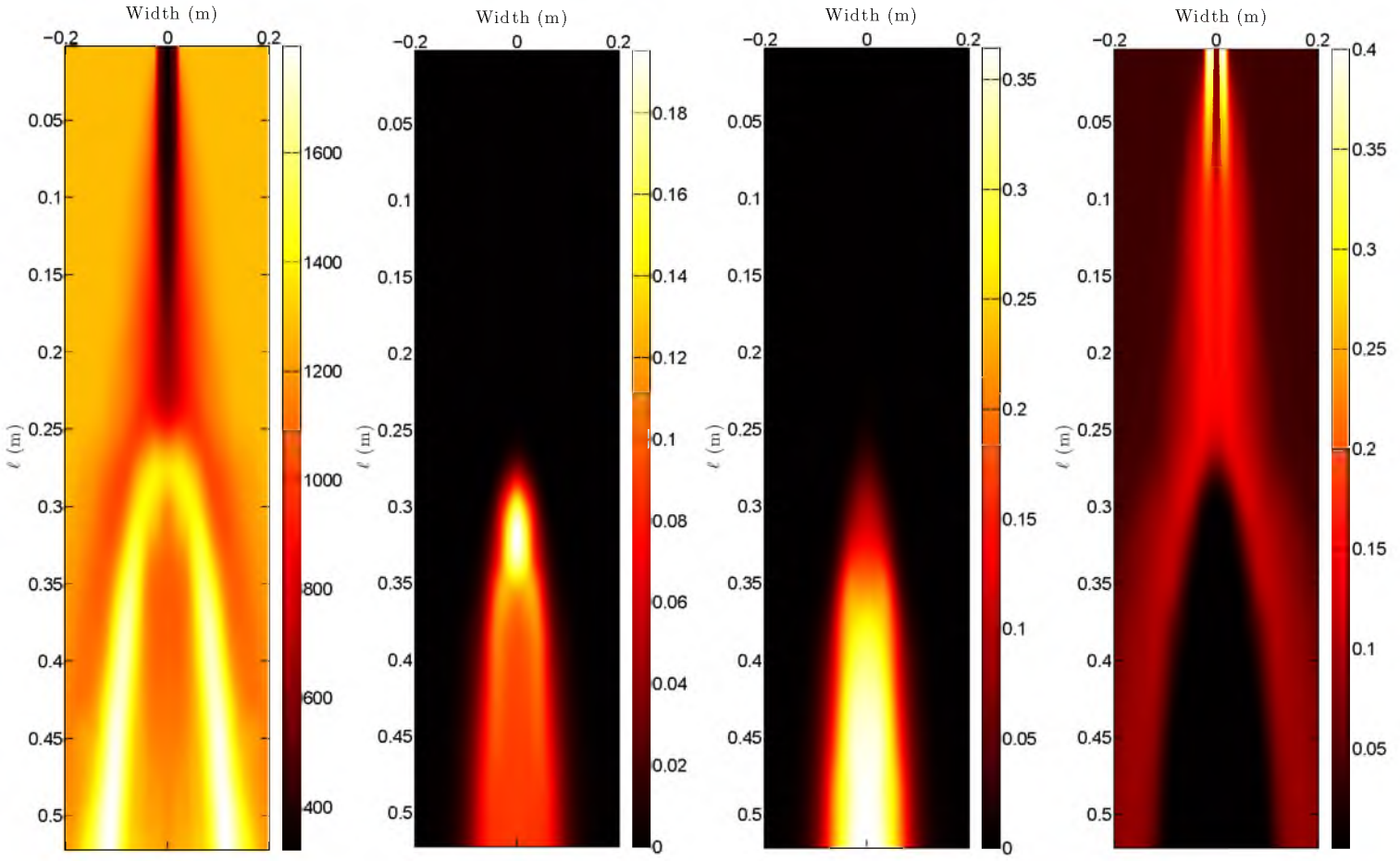

(a) Gas Temperature (K) (b) C_2H_2 mass fraction (c) CO mass fraction (d) O_2 mass fraction (in flame-sheet products)

Figure 4.16: Gas properties predicted using flame-sheet calculation (case E.2). Ensembeled gas phase properties, a) Gas temperature (K), b) C_2H_2 mass fraction, c) CO mass fraction, d) O_2 mass fraction.

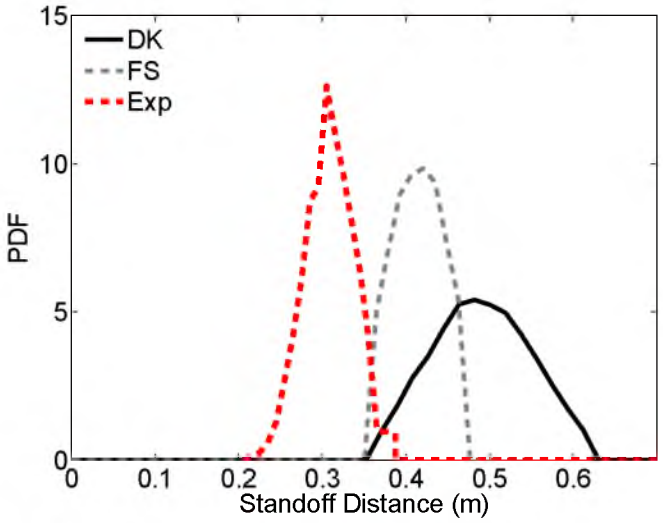

(a) T_w=1280 K

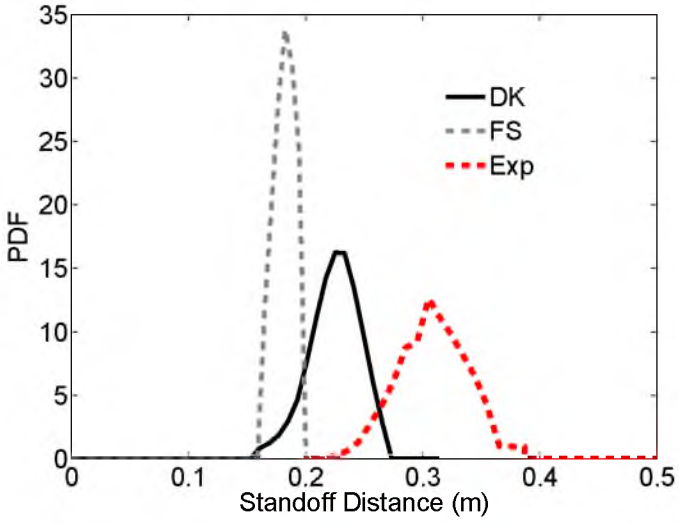

(b) T_w=1800 K

Figure 4.17: Flame stand-off PDFs obtained with detailed kinetic and flame-sheet model using radiative temperature 1280 and 1800 (cases E.4 and E.5).

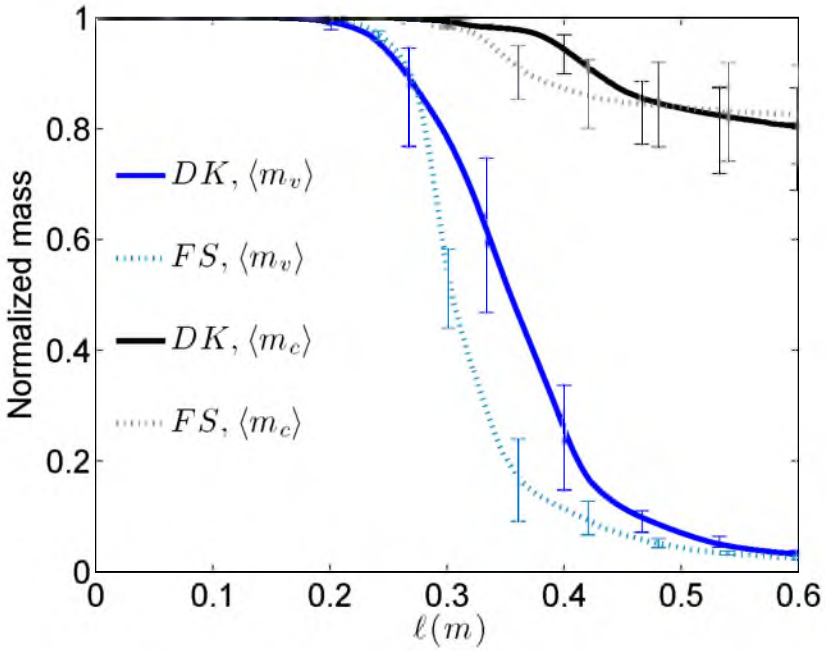

Figure 4.18: Normalized volatile and char mass (Cases A.3 & E.2).

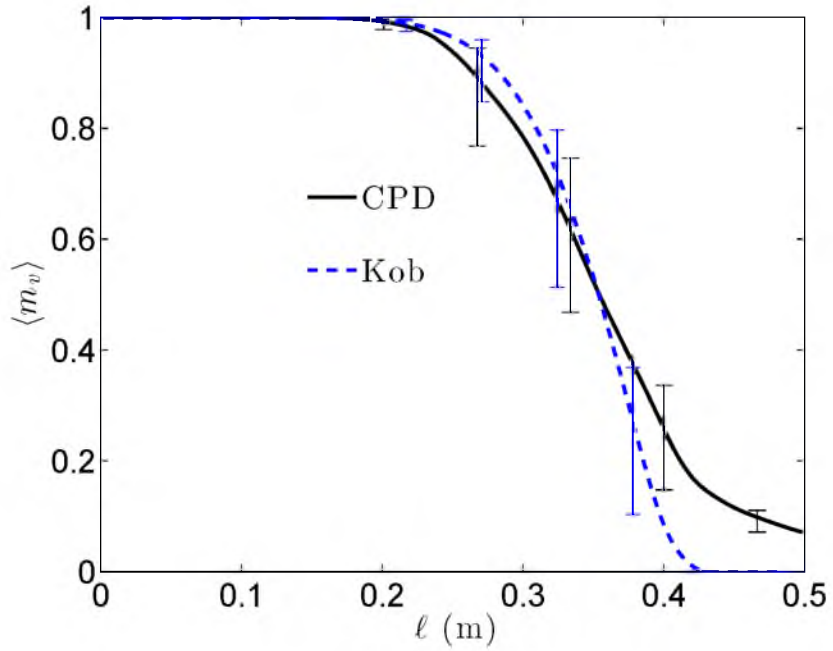

(a) normalized volatile mass

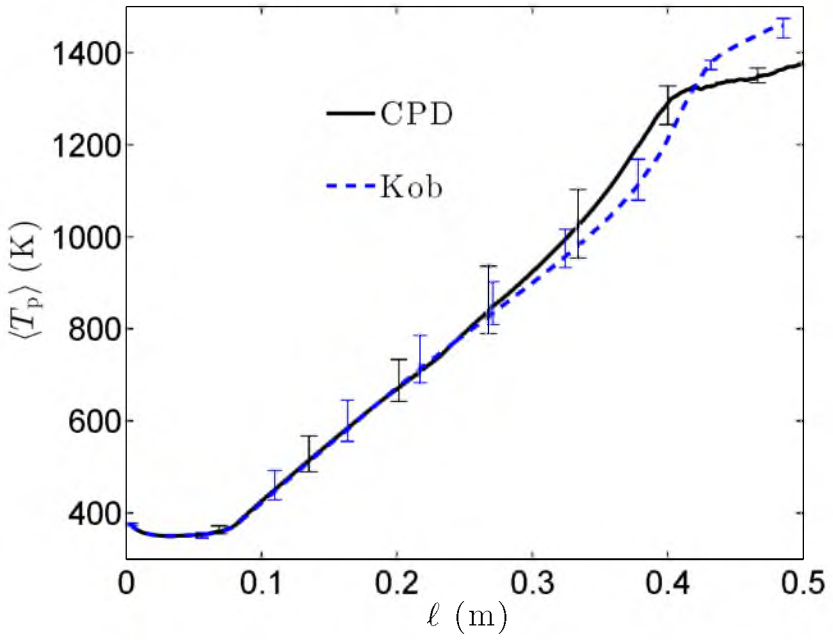

(b) average particles temperature

Figure 4.19: Devolatilization model impact on the coal particles behavior cases (A.3 and E.1). Averaged particle properties a) normalized mass, b) particles temperature (K).

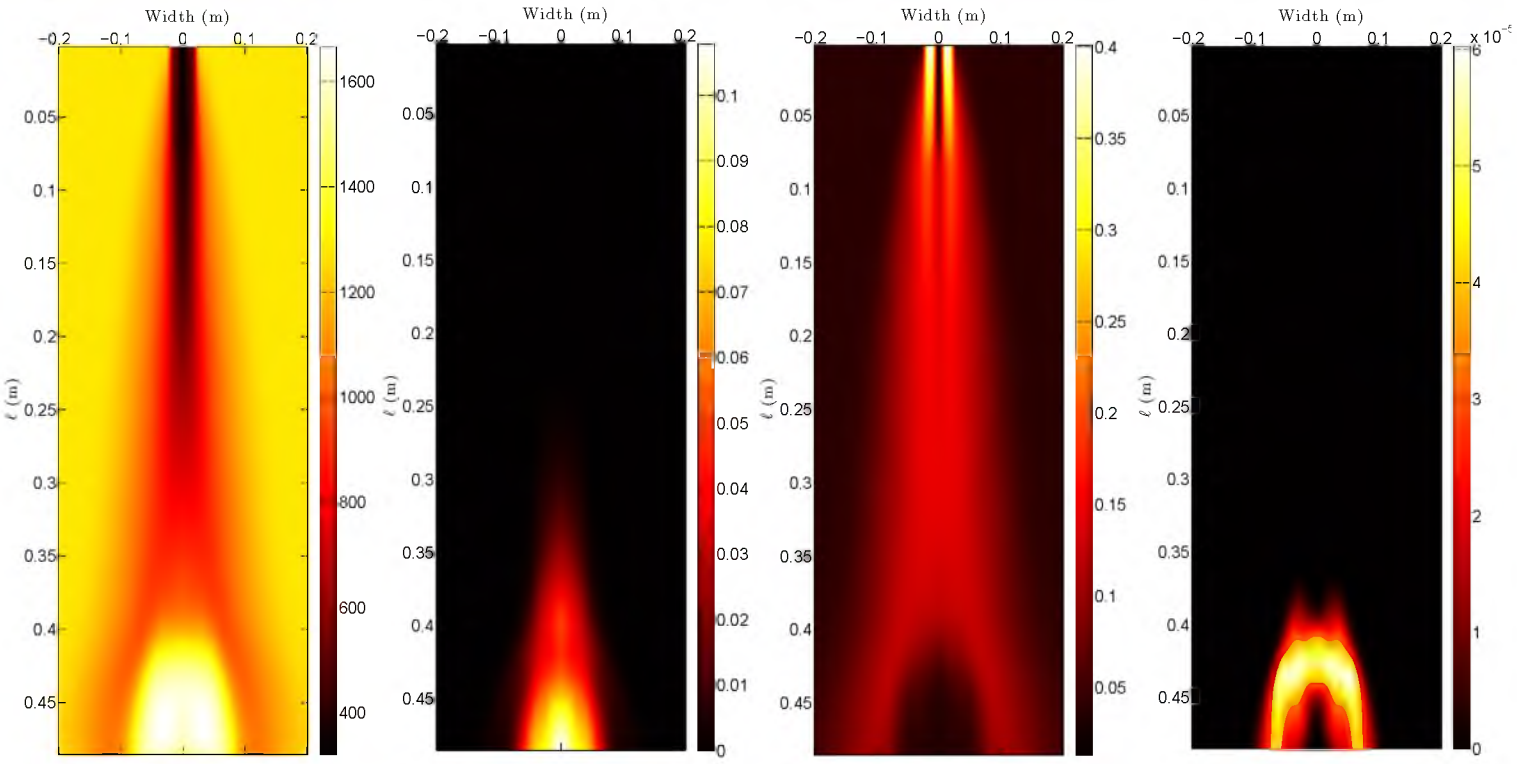

(a) Temperature (K) (b) CO mass fraction (c) O_2 mass fraction (d) OH mass fraction

Figure 4.20: Gas properties predicted using Kobayashi-Sarofim model and detailed kinetic calculation (case E.1). Ensembeled gas phase properties, a) Gas phase temperature (K), b) CO mass fraction, c)O_2 mass fraction, d)OH mass fraction.

CHAPTER 5

CONCLUSION

The coal combustion process is numerically simulated using One-Dimensional Turbulence (ODT) model. Impacts of system and model parameters as well as models complexity are studied and the simulation prediction are compared with experimental results. The purpose of this work was to simulate the coal combustion in a pilot/large scale combustor. To achieve this, different models were implemented through the ODT framework.

In the single particle simulation (Chapter 3), several models for coal particle ignition were considered where the simulation predictions are compared to experimental measurements available in the literature for two coal types at various furnace temperatures and for several particle sizes. Two models for devolatilization (CPD and the Kobayashi-Sarofim model) and two for the gas phase chemistry treatment (detailed kinetics and a flame-sheet model) were applied. These models essentially trade complexity for cost.

To the author's knowledge, this is the first simulation performed using detailed kinetics in the gas phase fully coupled to a high-fidelity model (CPD) for devolatilization of coal particles. The CPD model attempts to predict the light-gas evolution for the coal particles.

The results indicate that simpler Kobayashi-Sarofim and flame-sheet models roughly capture general trends present in the experimental data, but fail to provide quantitative agreement. On the other hand, the CPD model paired with detailed gas-phase chemistry provides reasonable agreement with the experimental observations over all reported conditions. This suggests that detailed devolatilization and gas-phase chemistry modeling are important to provide accurate characterization of ignition delay. This conclusion also applies when considering the ability of the models to capture trends when varying furnace temperature and particle size.

The amount of volatile produced by each devolatilization model at ignition is compared, and varies significantly between the CPD and Kobayashi-Sarofim models, with the CPD model showing much more sensitivity to the gas phase temperature in predicting the volatile yield at the point of ignition.

One significant challenge in comparing to experimental data is determining how to define ignition in the simulation. This is particularly challenging for the flame-sheet model where intermediate species are unavailable for comparison against the emission measurements of CH^* in the experiment. A rough indication of the sensitivity of the model predictions to the definition of the ignition delay are also presented.

In Chapter 4, simulations of oxy-coal flames have been performed using the ODT model. Because the ODT model must only resolve the physics in one spatial dimension, it allows incorporation of detailed thermochemistry models that would be unaffordable in DNS. Comparison to experimental data indicate that the model captures the flame standoff distance, a key marker of ignition, quite well. Results indicate that char gasification plays an important role during the later phases of the devolatilization process after homogeneous ignition occurs.

The impact of mixing rate on the flame stand-off prediction and physics of the system were also considered. For the cases studied in this dissertation, an increase in mixing rate decreases the likelihood of ignition at longer distances, however, its impact on short distances is not considerable, suggesting a kinetically limited lower bound to flame standoff. A study on impact of radiative temperature on simulation prediction is performed. Results show that radiative temperature significantly influences flame stand-off distance, modifying both mean and PDF of flame stand-off shape.

Additionally, the influence of model complexity on flame stand-off prediction was studied. The infinity-fast chemistry model and detailed kinetic calculation are employed in the gas phase and their predictions are compared. In the coal particle phase, CPD and Kobayashi-Sarofim models are utilized for devolatilization. The flame-sheet model predicts a narrower flame stand-off PDF than the detailed kinetic model. However, it has the same minimum distance as the detailed kinetic, confirming the minimum required fuel in the gas phase. For the cases explored in this dissertation, the Kobayashi-Sarofim model predicts longer flame stand-off than the CPD model, however, the results may vary by changing the coal type, particle heating rate, *etc.* Interestingly, the flame stand-off predictions of these devolatilization models become closer using the flame-sheet model in gas phase. Finally, the simulations performed in Chapter 4 consider a uniform particle size, and these conclusions must bear that in mind.

5.1 Recommendations for Future Work

This work is directed toward development of a prediction tool that simulates a large scale coal combustor/gasifier. In this dissertation some parts of this goal were achieved

by simulating a pilot scale oxy-coal combustor. However, there are many aspect of this predicting tool that require further development and investigation. A list of key items that require further work are:

- In this work, a reduced mechanism is utilized to address the gas phase chemistry. The reduced mechanism enforced some restriction on the simulation prediction such as soot production. However, it helped to reduce the computation cost considerably. Soot plays an important role in the combustion process and should be considered.

- The main focuse of this work was on the ignition process and regime, however, flame behavior after ignition and flame formation is not fully covered. This work, provided a reliable infrastructure for further investigation on flame stability, regime, extinction/reigntion and *etc.*

- It is necessary to validate the char oxidation model for further investigation on flame physics. In this work, modeling of the devolatilization process is studied in detail and the predictions are compared with experimental data. Char oxidation process also requires careful study since it governs a major part of particle life time in the combustion process.

- The study performed in Chapter 4 showed that the radiation term has a significant impact on the simulation prediction. Hence, it suggests a more sophisticated model to determine the radiation source terms for the particle. Additionally, considerable concentration of CO_2 and H_2O in the combustion environment affect the radiation. Considering radiation source term in the gas phase energy conservation equation (2.4) may also alter the simulation prediction notably.

REFERENCES

[1] U.S. Energy Information Administration. Annual energy outlook 2012 with projections to 2035. Technical report, U.S. Department of Energy, 2012.

[2] Klas Andersson, Fredrik Normann, Filip Johnsson, and Bo Leckner. No emission during oxy-fuel combustion of lignite. *Industrial & Engineering Chemistry Research*, 47(6):1835–1845, 2008.

[3] Donald B. Anthony and Jack B. Howard. Coal devolatilization and hydrogastification. *AICHE Journal*, 22(4):625–656, July 1976.

[4] Stanley Badzioch and Peter G. W. Hawksley. Kinetics of thermal decomposition of pulverized coal particles. *Industrial & Engineering Chemistry Process Design and Development*, 9(4):521–530, 1970.

[5] M. M. Baum and P. J. Street. Predicting the combustion behavior of coal particles. *Combustion Science and Technology*, 3:231–243, 1971.

[6] B. Scott Brewster, Larry L. Baxter, and L. Douglas Smoot. Teatment of coal devolatilization in comprehensive combustion modeling. *Energy & Fuels*, 2:362–370, 1988.

[7] Arden L. Buck. New equations for computing vapor pressure and enhancement factor. *J. Appl. Meteor*, 20:1527–1532, 1981.

[8] Hauli Cao, Shaozeng Sun, Yinghui Liu, and Terry F Wall. Computational fluid dynamics modeling of nox reduction mechanism in oxy-fuel combustion. *Energy & Fuels*, 24:131–135, 2010.

[9] Farid Chejne and Carlos A. Londoño Eliana Lopera. Modelling and simulation of a coal gasification process in pressurized fluidized bed. *Fuel*, 90(1):399–411, 2011.

[10] Lei Chen and Ahmed F. Ghoniem. Simulation of oxy-coal combustion in a 100 kWth test facility using RANS and LES: A validation study. *Energy & Fuels*, 26:4783–4798, 2012.

[11] Lei Chen, Sze Zheng Yong, and Ahmed F. Ghoniem. Oxy-fuel combustion of pulverized coal: Characterization, fundamentals, stabilization and CFD modeling. *Progress in Energy and Combustion Science*, 38:156–214, 2012.

[12] Caixia Chena, Masayuki Horioa, and Toshinori Kojimab. Use of numerical modeling in the design and scale-up of entrained flow coal gasifiers. *Fuel*, 80:1513–1523, 2001.

[13] Clayton T. Crowe, John D Schwarzkodf, Martin Sommerfeld, and Yutaka Tsuji. *Multiphase Flows with Droplets and Particles*. CRC Press, second edition, 2012.

[14] Rodrigo Corrêa da Silva, Tanin Kangwanpongpan, and Hans Joachim Krautz. Flame pattern, temperatures and stability limits of pulverized oxy-coal. *Fuel*, 115:507–520, 2014.

[15] E. G. Eddings, A. Molina, D. W. Pershing, A. F. Sarofim, T. H. Fletcher, H. Zhang, K. A. Davis, M. Denison, and H. Shim. Minimization of no emissions from multi-burner coal-fired boilers. Technical Report Final Report, U.S. Dept. of Energy, 2002.

[16] P. Edge, S. R. Gubba, L. Ma, R. Porter, M. Pourkashanian, and A. Williams. Les modelling of air and oxy-fuel pulverised coal combustion—impact on flame properties. *Proceedings of the Combustion Institute*, 33(2):2709–2716, 2011.

[17] W. Eisermann, P. Johnson, and W.L. Conger. Estimating thermodynamic properties of coal, char, tar and ash. *Fuel Processing Technology*, 3:39–53, 1980.

[18] Bo Feng and Suresh K. Bhatia. Variation of the pore structure of coal chars during gasification. *Carbon*, 41(507-523), 2003.

[19] J. Fermoso, B. Arias, M.V. Gil, M.G. Plaza, C. Pevida, J.J. Pis, and F. Rubiera. Co-gasification of different rank coals with biomass and petroleum coke in a high-pressure reactor for h2-rich gas production. *Bioresource Technology*, 101(9):3230–3235, 2010.

[20] Thomas H. Fletcher, Jinliang Ma, James R. Rigby, Alexander L. Brown, and Brent W. Webb. Soot in coal combustion systems. *Progress in Energy and Combustion Science*, 23(3):283–301, 1997.

[21] George R. Gavalas, Paul How-Kei Cheong, and Ravi Jain. Model of coal pyrolysis. 1. Qualitative development. *Industrial & Engineering Chemistry Fundamentals*, 20(2):113–122, 1981.

[22] M. Geier, C.R. Shaddix, and F. Holzleithner. A mechanistic char oxidation model consistent with observed CO2/CO production ratios. *Proceedings of the Combustion Institute*, 34:2411–2418, 2013.

[23] Curtis F. Gerald and Patrick O. Wheatley. *Applied Numerical Analysis*. Addison - Wesley, sixth edition, 1999.

[24] M. Gharebaghi, R.M.A. Irons, L. Ma, M. Pourkashanian, and A. Pranzitelli. Large eddy simulation of oxy-coal combustion in an industrial combustion test facility. *International Journal of Greenhouse Gas Control*, 5(1):S100–S110, 2011.

[25] David M Grant, Ronald J Pugmire, Thomas H Fletcher, and Alan R Kerstein. Chemical model of coal devolatilization using percolation lattice statistics. *Energy & Fuels*, 3:175–186, 1989.

[26] Nozomu Hashimoto, Ryoichi Kurose, Seung-Min Hwang, Hirofumi Tsuji, and Hiromi Shirai. A numerical simulation of pulverized coal combustion employing a tabulated-devolatilization-process model (TDP model). *Combustion and Flame*, 159:353–366, 2012.

[27] Ethan S. Hecht, Christopher R. Shaddix, Manfred Geier, Alejandro Molina, and Brian S. Haynes. Effect of CO2 and steam gasification reactions on the oxy-combustion of pulverized coal char. *Combustion and Flame*, 159:3437–3447, 2012.

[28] Ethan S. Hecht, Christopher R. Shaddix, and JoAnn S. Lighty. Analysis of the errors associated with typical pulverized coal char combustion modeling assumptions for oxy-fuel combustion. *Combustion and Flame*, 160:1499–1509, 2013.

[29] Ethan S. Hecht, Christopher R. Shaddix, Alejandro Molina, and Brian S. Haynes. Effect of CO2 gasification reaction on oxy-combustion of pulverized coal char. *Proceedings of the Combustion Institute*, 33:1699–1706, 2011.

[30] Ethan S. Hecht, Christopher R. Shaddix, Alejandro Molina, and Brian S. Haynes. Effect of CO2 gasification reaction on oxy-combustion of pulverized coal char. *Proc. Combust. Inst.*, 33:1699–1706, 2011.

[31] F.J. Higuera. Numerical simulation of the devolatilization of a moving coal particle. *Combustion and Flame*, 156:1023–1034, 2009.

[32] Frank P. Incropera and David P. DeWitt. *Introduction to Heat Transfer*. John Wiley & Sons, fourth edition, 2002.

[33] Mark Jost, Ian Leslie, and Charles Kruger. Flow-tube reactor studies of devolatilization of pulverized coal in an oxidizing environment. *Proc. Combust. Inst.*, 20(1):1531–1537, 1985.

[34] Rastko Jovanovic, Aleksandra Milewska, Bartosz Swiatkowski, Adrian Goanta, and Hartmut Spliethoff. Numerical investigation of influence of homogeneous/heterogeneous ignition/combustion mechanisms on ignition point position during pulverized coal combustion in oxygen enriched and recycled flue gases atmosphere. *International Journal of Heat and Mass Transfer*, 54(4):921–931, 2011.

[35] Rastko Jovanovic, Aleksandra Milewska, Bartosz Swiatkowski, Adrian Goanta, and Hartmut Spliethoff. Sensitivity analysis of different devolatilisation models on predicting ignition point position during pulverized coal combustion in o2/n2 and o2/co2 atmospheres. *Fuel*, 101:23–37, 2012.

[36] Rastko Jovanovic, Boško Rašuo, Predrag Stefanovic, Dejan Cvetinovic, and Bartosz Swiatkowski. Numerical investigation of pulverized coal jet flame characteristics under different oxy-fuel conditions. *International Journal of Heat and Mass Transfer*, 58:654–663, 2013.

[37] Ravichandra S Jupudi, Vladimir Zamansky, and Thomas H. Fletcher. Prediction of light gas composition in coal devolatilization. *Energy & Fuels*, 23:3063–3067, 2009.

[38] S. Kajitani, S. Hara, and H. Matsuda. Gasification rate analysis of coal char with a pressurized drop tube furnace. *Fuel*, 81(5):539–546, 2002.

[39] Tanin Kangwanpongpan, Rodrigo Corrêa da Silva, and Hans Joachim Krautz. Prediction of oxy-coal combustion through an optimized weighted sum of gray gases model. *Energy*, 41:244–251, 2012.

[40] Mohammad Kariznovi, Hossein Nourozieh, Jalal Abedi, and Zhangxin Chen. Simulation study and kinetic parameter estimation of underground coal gasification in alberta reservoirs. *Chemical Engineering Research and Design*, 91(3):464–476, 2013.

[41] A R Kerstein. One-dimensional turbulence: Model formulation and application to homogeneous turbulence, shear flows, and buoyant stratified flows. *J. Fluid Mech.*, 392:277–334, 1999.

[42] S.P. Khare, T.F. Wall, A.Z. Farida, Y. Liu, B. Moghtaderi, and R.P. Gupta. Factors influencing the ignition of flames from air-fired swirl pf burners retrofitted to oxy-fuel. *Fuel*, 87(7):1042–1049, 2008.

[43] Reza Khatami, Chris Stivers, Kulbhushan Joshi, Yiannis A. Levendis, and Adel F. Sarofim. Combustion behavior of single particles from three different coal ranks and from sugar cane bagasse in O2/N2 and O2/CO2 atmospheres. *Combustion and Flame*, 159(1253-1271), 2012.

[44] Reza Khatami, Chris Stivers, and Yiannis A. Levendis. Ignition characteristics of single coal particles from three different ranks in O2/N2 and O2/CO2 atmospheres. *Combustion and Flame*, 159:3554–3568, 2012.

[45] H. Kobayashi, J. B. Howard, and A. F. Sarofim. Coal devolatilization at high temperatures. *Symposium (International) on Combustion*, 16:411–425, 1977.

[46] M. Gharebaghi L. Álvarez a, M. Pourkashanian, A. Williams, J. Riaza, C. Pevida, J.J. Pis, and F. Rubiera. CFD modelling of oxy-coal combustion in an entrained flow reactor. *Fuel Processing Technology*, 92(1489-1497), 2011.

[47] Chun Wai Lau and Stephen Niksa. The combustion of individual particles of various coal types. *Combustion and Flame*, 90(1):45–70, 1992.

[48] Yiannis A. Levendis, Kulbhushan Joshi, Reza Khatami, and Adel F. Sarofim. Combustion behavior in air of single particles from three different coal ranks and from sugarcane bagasse. *Combustion and Flame*, 158:452–465, 2011.

[49] David O. Lignell and Devin S. Rappleye. One-dimensional-turbulence simulation of flame extinction and reignition in planar ethylene jet flames. *Combustion and Flame*, 159:2930–2943, 2012.

[50] Hao Liu, Chunhua Luo, Masahiro Kaneko, Shigeru Kato, and Toshinori Kojima. Unification of gasification kinetics of char in CO2 at elevated temperatures with a modified random pore model. *Energy & Fuels*, 17:961–970, 2003.

[51] Yinhe Liu, Manfred Geier, Alejandro Molina, and Christopher R. Shaddix. Pulverized coal stream ignition delay under conventional and oxy-fuel combustion conditions. *International Journal of Greenhouse Gas Control*, 5:S36–S46, 2011.

[52] Liqiang Ma and Reginald Mitchell. Modeling char oxidation behaviour under zone ii burning condition at elevated preesure. *Combustion and Flame*, 156(1):37–50, 2009.

[53] Rosemary A. MacDonald, Jane E. Callanan, and Kathleen M. McDermott. Heat capacity of a medium-volatile bituminous premium coal from 300 to 520 k. comparison with a high-volatile bituminous nonpremium coal. *Energy & Fuels*, 1(6):535–540, 1987.

[54] Tiziano Maffei, Reza Khatami, Sauro Pierucci, Tiziano Faravelli, Eliseo Ranzi, and Yiannis A. Levendis. Experimental and modeling study of single coal particle combustion in O2/N2 and oxy-fuel (O2/CO2) atmospheres. *Combustion and Flame*, 160:2559–2572, 2013.

[55] Daniel J. Maloney, Ramanathan Sampath, and John W. Zondlo. Heat capacity and thermal conductivity considerations for coal particles during the early stages of rapid heating. *Combustion and Flame*, 116(1-2):94–104, January 1999.

[56] Reginal E. Mitchell. On the products of the hetrogeneous oxidation reaction at the surfaces of burning coal char particles. *Symposium (International) on Combustion*, 22(1):69–78, 1988.

[57] Reginald E. Mitchell, Liqiang Ma, and BumJick Kim. On the burning behavior of pulverized coal chars. *Combustion and Flame*, 151:426–436, 2007.

[58] Alejandro Molina and Christopher R. Shaddix. Ignition and devolatilization of pulverized bituminous coal particles during oxygen/carbon dioxide coal combustion. *Proceedings of the Combustion Institute*, 31:1905–1912, 2007.

[59] Charles R. Monson, Geoffrey J. Germane, Angus U. Blackdam, and L. Douglas Smoot. Char oxidation at elevated pressures. *Combustion and Flame*, 23:1207–1213, 1990.

[60] Tatsuya Morimoto, Tetsuya Ochiai, Sadao Wasaka, and Hirokazu Oda. Modeling on pore variation of coal chars during CO2 gasification associated with their submicropores and closed pores. *Energy & Fuels*, 20(353-358), 2006.

[61] Jeffrey J. Murphy and Christopher R. Shaddix. Combustion kinetics of coal chars in oxygen-enriched environments. *Combustion and Flame*, 144(4):710–729, 2006.

[62] Prabhat Naredi and Sarma Pisupati. Effect of co2 during coal pyrolysis and char burnout in oxy-coal combustion. *Energy & Fuels*, 25:2452–2459, 2011.

[63] Gregory Nellis and Sanford Klein. *Heat Transfer*. Cambridge, 2008.

[64] Stephen Niksa, Gui su Liua, and Robert H. Hurt. Coal conversion submodels for design applications at elevated pressures. Part I. Devolatilization and char oxidation. *Progress in Energy and Combustion Science*, 29(5):425–477, 2003.

[65] Fredrik Normann, Klas Andersson, Bo Leckner, and Filip Johnsson. Emission control of nitrogen oxides in the oxy-fuel process. *Progress in Energy and Combustion Science*, 35(5):385–397, 2009.

[66] PATRICK K. NOTZ, ROGER P. PAWLOWSKI, and James C. Sutherland. Graph-based software design for managing complexity and enabling concurrency in multiphysics pde software. *ACM Transactions on Mathematical Software*, 39(1), 2012.

[67] Julien Pedel. *LARGE EDDY SIMULATIONS OF COAL JET FLAME IGNITION USING THE DIRECT QUADRATURE METHOD OF MOMENTS*. PhD thesis, The University of Utah, 2012.

[68] Julien Pedel, Jeremy N. Thornock, and Philip J. Smith. Ignition of co-axial turbulent diffusion oxy-coal jet flames: Experiments and simulations collaboration. *Combustion and Flame*, 160:1112–1128, 2013.

[69] R. H. Perry, D. W. Green, and J. O. Maloney. *Perry's Handbook of Chemical Engineering*. McGraw-Hill, New York, 6 edition, 1984.

[70] C. P. Please, M. J. McGuinness, and D. L. S. McElwain. Approximation to the distributed activation energy model for the pyrolysis of coal. *Combustion and Flame*, 133:107–117, 2003.

[71] Bruce E. Poling, John M. Prausnitz, and John P. O'Connell. *The Properties of Gases and Liquids*. McGraw-Hill, fifth edition, 2004.

[72] Anna Ponzio, Sivalingam Senthoorselvan, Weihong Yang, Wlodzmierz Blasiak, and Ola Eriksson. Ignition of single coal particles in high-temperature oxidizers with various oxygen concentrations. *Fuel*, 87:974–987, 2008.

[73] N. Punati, J. C. Sutherland, A. R. Kerstein, E. R. Hawkes, and J. H. Chen. An evaluation of the one-dimensional turbulence model: Comparison with direct numerical simulations of co/h2 jets with extinction and reignition. *Proc. Combust. Inst.*, 33(1):1515–1522, 2011.

[74] Naveen Punati. *An Eulerian One-Dimensional Turbulence Model: Application to Turbulent and Multiphase Reacting Flows.* PhD thesis, Department of Chemical Engineering, The University of Utah, January 2012.

[75] Charles Martin Reid. *AN INSTRUMENTALIST APPROACH TO VALIDATION: A QUANTITATIVE ASSESSMENT OF A NOVEL COAL GASIFICATION MODEL.* PhD thesis, The University of Utah, 2012.

[76] Dadmehr Rezaei. *Co-Axial Turblent Diffusion Flames with Directed Oxygen Injection.* PhD thesis, The University of Utah, May 2013.

[77] Dadmehr Rezaei, Yuegui Zhou, Jingwei Zhang, Kerry E. Kelly, Eric G. Eddings, Ronald J. Pugmire, Mark S. Solum, and Jost O. L. Wendt. The effect of coal composition on ignition and flame stability in coaxial oxy-fuel turbulent diffusion flames. *Energy & Fuels*, 27:4935–4945, 2013.

[78] Günter Scheffknecht, Leema Al-Makhadmeh, Uwe Schnell, and Jörg Maier. Oxy-fuel coal combustion: A review of the current state-of-the-art. *International Journal of Greenhouse Gas Control*, 5S(S16-S35), 2011.

[79] J. R. Schmidt. *Stochastic Models for the Prediction of Individual Particle Trajectories in One-Dimensional Turbulence Flows.* PhD thesis, The University of Arizona, 2004.

[80] John R. Schmidt, Jost O. L. Wendt, and Alan R. Kerstein. Non-equilibrium wall deposition of inertial particles in turbulent flow. *Journal of Statistical Physics*, 137(2):233–257, 2009.

[81] Christopher R. Shaddix and Alejandro Molina. Particle imaging of ignition and devolatilization of pulverized coal during oxy-fuel combustion. *Proceedings of the Combustion Institute*, 32(2091-2098), 2009.

[82] Christopher R. Shaddix and Alejandro Molina. Fundamental investigation of nox formation during oxy-fuel combustion of pulverized coal. *Proceedings of the Combustion Institute*, 33(2):1723–1730, 2011.

[83] Y. S. Shen, B. Y. Guo, A. B. Yu, and P. Zulli. A three-dimensional numerical study of the combustion of coal blends in blast furnace. *Fuel*, 88:255–263, 2009.

[84] Randy C. Shurtz, Kolbein K. Kolste, and Thomas H. Fletcher. Coal swelling model for high heating rate pyrolysis aplication. *Energy & Fuels*, 25:2163–2173, 2011.

[85] Armin Silaen and Ting Wang. Effect of turbulence and devolatilization models on coal gasification simulation in an entrained-flow gasifier. *International Journal of Heat and Mass Transfer*, 53:2074–2091, 2010.

[86] N. Slavinskaya, M. Braun-Unkhoff, and P. Frank. Reduced reaction mechanisms for methane and syngas combustion in gas turbines. *Institute of Combustion Technology*, 130:38–40, MARCH 2008.

[87] J. P. Smart, P. O'Nions, and G.S. Riley. Radiation and convective heat transfer, and burnout in oxy-coal combustion. *Fuel*, 89(9):2468–2476, 2010.

[88] I. W. Smith. The combustion rates of coal chars: A review. *Symposium (International) on Combustion*, 19:1045–1065, 1982.

[89] K. Lee Smith, L. Douglas Smoot, Thomas H. Fletcher, and Ronald J. Pugmire. *The Structure and Reaction Process of Coal.* Plenum Press, New York, 1994.

[90] L. Douglas Smoot and Philip J. Smith. *Coal Combustion and Gasification.* Plenum Press, 1985.

[91] P. R Solomon, D. G. Hamblen, R. M. Carangelo, M. A. Serio, and G. V. Deshpande. General model of coal devolatilization. *Energy & Fuels*, 2:405–422, 1988.

[92] J. C. Sutherland and C. A. Kennedy. Improved boundary conditions for viscous, reacting, compressible flows. *J. Comp. Phys.*, 191(2):502–524, 2003.

[93] James C. Sutherland, Naveen Punati, and Alan R. Kerstein. *A Unified Approach to the Various Formulations of the One-Dimensional-Turbulence Model.* Institute for Clean and Secure Energy, 2010.

[94] Yewen Tan, Eric Croiset, Mark A. Douglas, and Kelly V. Thambimuthu. Combustion characteristics of coal in a mixture of oxygen and recycled flue gas. *Fuel*, 85(4):507–512, 2006.

[95] L. Tognotti, J. P. Longwell, and A. F. Sarofim. The products of the high temperature oxidation of a single char particle in an electrodynamic balance. *Symposium (International) on Combustion*, 23(1):1207–1213, 1991.

[96] Shivadev K. Ubhayakar, David B. Stickler, Charles W. Von Rosenberg Jr., and Richard E. Gannon. Rapid devolatilization of pulverized coal in hot combustion gases. *Symposium (International) on Combustion*, 16(1):427–436, 1977.

[97] M. Vascellari, R. Arora, M. Pollack, and C. Hasse. Simulation of entrained flow gasification with advanced coal conversion submodels. Part 1: Pyrolysis. *Fuel*, 113(654-669), 2013.

[98] M. Vascellari and G. Cau. Influence of turbulence-chemical interaction on CFD pulverized coal MILD combustion modeling. *Fuel*, 101:90–101, 2012.

[99] M. Vascellari and C. Hasse H. Xu. Flamelet modeling of coal particle ignition. *Proc. Combust. Inst.*, 34:2445–2452, 2013.

[100] C.S. Wang, G.F. Berry, K.C. Chang, and A.M. Wolsky. Combustion of pulverized coal using waste carbon dioxide and oxygen. *Combustion and Flame*, 72(3):301–310, 1988.

[101] Fu Yang Wang and Suresh K. Bhatia. A generalised dynamic model for char particle gasification with structure evolution and peripheral fragmentation. *Chemical Engineering Science*, 56:3683–3697, 2001.

[102] H. Watanabe and M. Otaka. Numerical simulation of coal gasification in entrained flow coal gasifier. *Fuel*, 85:1935–1943, 2006.

[103] K. M. Watson. Thermodynamics of the liquid state. *Ind. Eng. Chem.*, 35(4):398–406, 1943.

[104] Chungen Yin, Lasse A. Rosendahl, and Søren K. Kær. Chemistry and radiation in oxy-fuel combustion: A computational fluid dynamics modeling study. *Fuel*, 90:2519–2529, 2011.

[105] Jingwei Zhang, Kerry E. Kelly, Eric G. Eddings, and Jost O.L. Wendt. CO2 effects on near field aerodynamic phenomena in 40 kw, co-axial, oxy-coal, turbulent diffusion flames. *International Journal of Greenhouse Gas Control*, 55:547–557, 2011.

[106] Wu Zhou, Changsui Zhao, Lunbo Duan, Daoyin Liu, and Xiaoping Chen. CFD modeling of oxy-coal combustion in circulating fluidized bed. *International Journal of Greenhouse Gas Control*, 5:1489–1497, 2011.

[107] Mingming Zhu, Hai Zhang, Zhezi Zhang, and Dongke Zhang. A numerical modeling study of ignition of single coal particles under microgravity conditions. *Combustion Science and Technology*, 183(11):1221–1235, 2011.